REPORT DOCUMENTATION PAGE		Form Approved OMB No. 0704-018H

The public reporting burden for this collection of information is estimated to average 1 hour per response, including the time for reviewing instructions, searching existing data sources, gathering and maintaining the data needed, and completing and reviewing the collection of information. Send comments regarding this burden estimate or any other aspect of this collection of information, including suggestions for reducing the burden, to Department of Defense, Washington Headquarters Services, Directorate for Information Operations and Reports (0704-0188), 1215 Jefferson Davis Highway, Suite 1204, Arlington, VA 22202-4302. Respondents should be aware that notwithstanding any other provision of law, no person shall be subject to any penalty for failing to comply with a collection of information if it does not display a currently valid OMB control number.
PLEASE DO NOT RETURN YOUR FORM TO THE ABOVE ADDRESS.

1. REPORT DATE (DD-MM-YYYY)	2. REPORT TYPE		3. DATES COVERED (From - To)
21-08-2006	FINAL		JUNE 2003 - AUG. 2006

4. TITLE AND SUBTITLE	5a. CONTRACT NUMBER
STRUCTURALLY EFFICIENT ANISOTROPIC ORGANIZED RETICULATED STRUCTURES FOR COOLING OF ELECTRONICS AND SENSORS	F49620-03-1-342 03-1-0342
	5b. GRANT NUMBER
	5c. PROGRAM ELEMENT NUMBER

6. AUTHOR(S)	5d. PROJECT NUMBER
RICHARD A. WIRTZ YANYAO JIANG	
	5e. TASK NUMBER
	5f. WORK UNIT NUMBER

7. PERFORMING ORGANIZATION NAME(S) AND ADDRESS(ES)	8. PERFORMING ORGANIZATION REPORT NUMBER
University of Nevada, Reno 1664 N. Virginia St. Sponsored Projects / Mail Stop 325 Reno, NV 89557-0240	1320-117-30DA

9. SPONSORING/MONITORING AGENCY NAME(S) AND ADDRESS(ES)	10. SPONSOR/MONITOR'S ACRONYM(S)
Lt. Col Rhett Jefferies AFOSR/NA 875 North Randolph Street Suite 325, Room 3112 Arlington, VA 22203-1768	
	11. SPONSOR/MONITOR'S REPORT NUMBER(S)

12. DISTRIBUTION/AVAILABILITY STATEMENT
Approved for public release, distribution unlimited   AFRL-SR-AR-TR-08-0146

13. SUPPLEMENTARY NOTES

14. ABSTRACT

Anisotropic organized reticulated structures, consisting of group-interconnected and purposely oriented thermally conductive filaments, can be configured to have wide ranging porosity, a large specific surface area, and superior strength characteristics. When deployed as heat exchanger matrices, these structures produce high ntu-values because of the large specific surface area inherent to the media. Analytical and numerical tools are developed to evaluate the geometric, thermal and structural attributes of box lattice structures (an example of such media). Models of porosity, specific surface area and effective thermal conductivity are developed. Numerical CFD simulations investigate flow and transport characteristics. Flow boiling experiments assess the performance of porous extended surface matrices.

15. SUBJECT TERMS

reticulated-filament-media, heat transfer, convection, boiling, extended-surfaces, strength, stiffness,

16. SECURITY CLASSIFICATION OF:			17. LIMITATION OF ABSTRACT	18. NUMBER OF PAGES	19a. NAME OF RESPONSIBLE PERSON
a. REPORT	b. ABSTRACT	c. THIS PAGE			R.A. Wirtz
UU	UU	UU	UU	100	19b. TELEPHONE NUMBER (include area code) 775-784-6714

Reset   Standard Form 298 (Rev. 8-98)
Prescribed by ANSI Std. Z39.18

Structurally Efficient Anisotropic Organized Reticulated Structures
For Cooling Of Electronics And Sensors

F49620-03-1-342

Richard A. Wirtz and Yanyao Jiang

Mechanical Engineering Department
University of Nevada, Reno
Reno, NV 89557

(775) 784-6714

August 31, 2006

Table of Contents

Summary

Anisotropic _Organized_ _Reticulated-Filament_ _Structures_ (AORS), consisting of group-interconnected and _purposely oriented_ thermally conductive filaments, can be configured to have wide ranging porosity and a large specific surface area. When deployed as heat exchanger matrices, these structures produce high _ntu_-values (number of transfer units) because of the large specific surface area inherent to the media. Examples of structures with the above described characteristics are: laminations of orthogonal-weave fine-wire screen, three-filament stacked weaves and box lattice structures. Box lattice structures offer increased design flexibility relative to woven structures since filament cross section shape (in addition to filament orientation) can be tailored to a specific application. Relative to a box lattice with circular cross section filaments, ellipticity adds surface area to the structure, as well as the possibility to streamline flow through the array. Furthermore, box lattices have superior strength characteristics.

Research focuses on characterizing the geometric, thermal and structural attributes of box lattice structures. Geometric models of porosity and specific surface area are developed along with a thermal model of the effective of the effective thermal conductivity. They show that metal fraction can range as: 0% - 0.94%; dimensionless specific surface area can range as: 0.93- 3.14 and dimensionless effective thermal conductivity can range as: $0 - 0.78$.

Numerical simulations evaluate laminar and turbulent flow and single phase convection in circular cross section filament box lattice structures. CFD simulations of the flow in a unit cell show that laminar flow persists to a mesh Reynolds number of 150, and unsteady flows are found at higher Reynolds numbers. The flow field through the lattice structure has an intense jet flowing down the centerline of the cell encompassed by a relatively quiescent region. High wall shear stress and heat flux are observed on the down-stream portions of the cell, due to jet impingement on the windward side of the down-stream filaments. The friction factor correlation is similar to that found in flow through a packed bed of spheres and flow through a lamination of plain weave screens. The Stanton number correlation is lower than that of a packed bed of spheres; and, for higher Reynolds numbers, higher than that measured for flow through a screen lamination. Introduction of filament ellipticity resulted in an increase in surface shear stress and heat flux. Consequently, elliptic cross section filament box lattices have higher friction factor

and Stanton number correlations. Introduction of filament ellipticity also resulted in an increase in intensity of secondary flows within the matrix.

An investigation is conducted to assess the thermal performance of multi-layered screen laminates when used as extended surface matrices (ESM's) in vertical up-flow boiling. A dielectric coolant (FC-72) is used as the working fluid. Four specimens are constructed having different mesh-geometries and/or number of layers. Channel Reynolds numbers are varied from 2700 to 8500 and surface temperatures are varied from 50 °C to 100 °C.

Results indicate that devices equipped with this technology can tolerate steady heat fluxes up to 140 W/cm^2 (based on the base area of the ESM) with corresponding surface temperatures below 100°C. Reynolds number has a small effect on performance at low surface temperatures and a moderate effect at higher surface temperatures. Total capacity of the ESM (the product of heat flux and base area) increases approximately linearly with the thickness. A feature of this technology is that it greatly extends the working range over a bare surface.

The two major structural concerns are the strength and deformation when a structure is subjected to external loading. The deformation of a structure can be reliably simulated using the finite element method by implementing a suitable constitutive material deformation law. The strength of a structure needs to consider static loading and dynamic loading. For the static strength, the well-established von Mises criterion can be used after a stress analysis of the structure. The major concern of a structure is the fatigue strength. The current research has established an approach that can be used for the fatigue design and evaluation of an aluminum structure subjected to dynamic or fatigue loading.

The approach for the fatigue strength consists two steps. The first step is to determine the detailed stress-strain response of the material in the structure using the finite element method. A key element in the finite element stress analysis is the use of a suitable constitutive material law. The cyclic plasticity theory developed by Jiang and Sehitoglu has been widely accepted for the modeling of the stress-strain relationship of metallic materials. The current research confirms that the cyclic plasticity theory is well suited for the aluminum alloy that can be used as a heat exchanger. The cyclic plasticity model has been implemented into the finite element code.

Once the stress-strain response of the materials in a structure is known, a fatigue model is used to assess the fatigue strength of the material. The current research has generated extensive

deformation and fatigue results for 7075T6 aluminum alloy. The experimental results provide all the baseline mechanical properties of the material that are needed for the consideration of the mechanical properties of the aluminum structures. A robust fatigue model was developed and the model was validated with extensive experiments. A post-processor that implemented the fatigue model has been developed. The post-processor together with the finite element stress analysis can be directly applied to the fatigue design and evaluation of these multifunctional structures. Fabrication of the box lattice samples using an EDM is documented.

1. Introduction

A reticulated-filament open-cell structure, consisting of group-interconnected and *purposely oriented* thermally conductive ligaments, can be configured to have wide ranging porosity (ε) and a large specific surface area (β). When deployed as heat exchanger matrices, these structures produce high *ntu*-values (number of transfer units) because of the large specific surface area inherent to the media. *Anisotropic Organized Reticulated-Filament Structures* (AORS) can be configured by specification of ligament orientation, pitch, diameter and shape so that thermal properties such as the effective thermal conductivity vector ($\vec{k}_e$) and the structural strength and elastic characteristics can be tuned to a specific application. Because of the wide ranging porosity; high values of β and *ntu*; and, large $\vec{k}_e$ in a particular direction achieved, exchangers can be designed for applications where spatial temperature uniformity or high localized spot cooling is required. Furthermore, the ability to specify the elastic characteristics of the global structure provides that rigid structures can be fabricated.

Examples of structures with the above described characteristics are: laminations of orthogonal-weave and diamond weave fine-wire screen [Tong and London, 1957; Chang, 1990; Xu and Wirtz, 2003a, 2003b, 2005]; three-filament stacked weaves [Wirtz et al, 2003] and box lattice structures [Balantrapu et al, 2005; Sarde et al, 2006]. These structures can be configured to have a very large specific surface area (β), in excess of 50,000 m^{-1}. Effective thermal conductivities (ke) can approach 78% of base material values. Pore size can range from O(1 μm) to O(1 cm) or larger. Thin layers can be bonded to a plane surface, giving rise to a highly convoluted surface morphology. Monolithic open-pore structures can be assembled.

Figure 1.1 shows a lamination of plain-weave screen, which lies in the y-z plane. The filament diameter is D; and the "mesh number" *M* [filaments per inch] defines the filament pitch in the y- and z- directions. The product, *Md* gives the filament diameter-to-pitch ratio. The thickness of the plain-weave lamination is t.
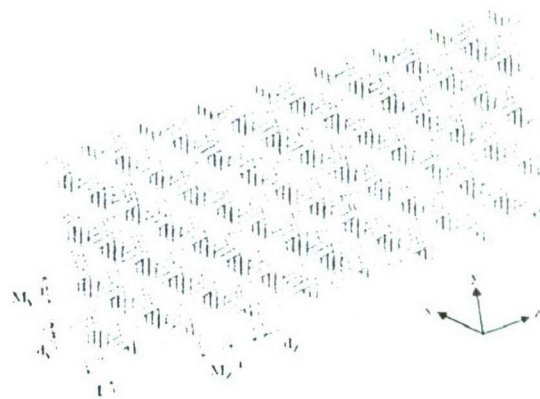

Fig. 1.1 Plain weave screen lamination

Anisotropy can be introduced by selection of different (M,d) for the y- and z-axis filaments; or specification of non-orthogonal (diamond) weaves.

Screens are woven on a loom. "Warp" filaments are those which emanate directly from the loom frame while "Shute" filaments are woven transverse to the warp filaments. Woven metal-filament screens are commercially available with $0.0005" \leq d \leq .120"$ and $2\ in^{-1} \leq M \leq 2800\ in^{-1}$ (see footnote[1]). Fine wire screen (Plain or Dutch weave) is stacked to form the lamination which is then diffusion bonded to form a monolith. Since fine-mesh screen can be bonded to course-mesh screen, composites having a large variation in pore size can be structured. These composite laminations could then be diffusion bonded to an un-enhanced surface, resulting in a highly convoluted heat transfer surface; or monolithic structures could be formed to be open cell, porous extended surfaces (fins) that are attached to a heat transfer surface.

Figure 1.2 compares a Plain Weave to a Dutch Weave. Whereas a Plain Weave has both warp and shute filaments that are serpentine, a "Dutch" weave has warp filaments that are straight. There may be some advantage with a Dutch weave since shute filaments can be spaced closely together resulting in a very dense three-dimensional structure with small cavities imbedded in the structure.
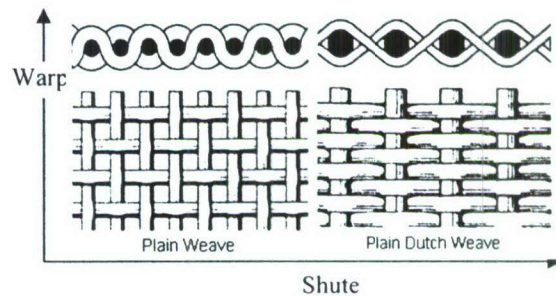
Fig. 1.2 Plain Weave–Dutch Weave comparison.

Table 1 Characteristics of some commercially available weaves.

M(warp)/M(shute) [inch⁻¹]	d(warp)/d(shute) [inch]	$\beta\ [m^2/m^3]$	βt	$D_h\ [\mu m]$
50/50 (plain)	0.008/0.008	6,750	2.7	390
200/200 (plain)	0.002/0.002	26,000	2.6	97
80/700 (Dutch)	0.004/0.003	45,000	11.4	9.6

Table 1 lists the physical characteristics of three commercially available weaves according to weave mesh number, M and filament diameter, D. The table lists specific surface area (β),

---

[1] In the United States, weaves are traditionally designated in British Gravitational units (inches)

surface area enhancement ratio (βt) and pore hydraulic diameter (D_h). The surface area enhancement ratio is the convoluted surface area provided by the screen divided by the area of an equal size plane surface. The hydraulic diameter is a measure of "pore size" of the weave. The table shows that even single-layer fine-filament weaves can be structured to have very large specific surface areas; large surface area enhancement ratios; and, pore sizes that can range from micron-scale to mm-scale (or larger).

Figure 1.3 shows a *box lattice structure* with elliptic cross section filaments bonded to a plane surface. Such structures offer increased design flexibility relative to woven structures since filament cross section shape (in addition to filament orientation) can be tailored to a specific application. Relative to a box lattice with circular cross section filaments, ellipticity adds surface area to the structure, as well as the possibility to streamline flow through the array. Die casting or a "sinker" Electro-Discharge Machine (EDM) is used to form slices of box lattice. The slices are then brazed or diffusion-bonded to a surface, as shown in Fig. 1.3.
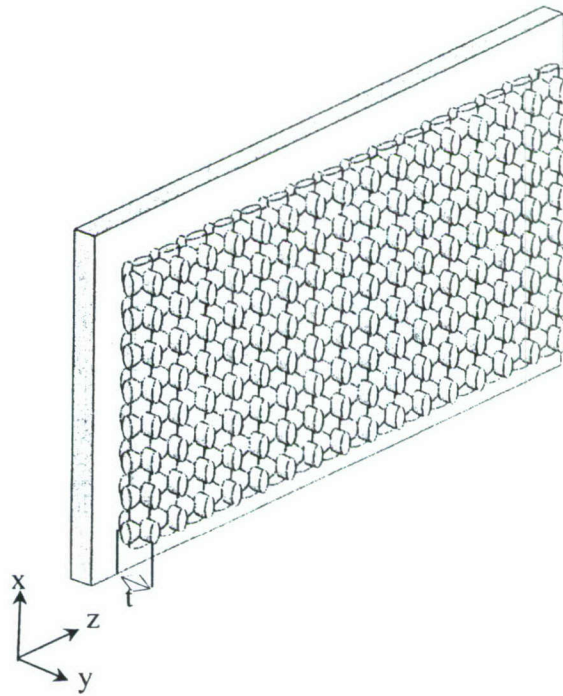
Fig. 1.3 Elliptic cross section filament box lattice

Additionally, a three-dimensional open-cell monolith can be formed, as shown in Fig. 1-4. In this case, the structure could be applied as an extended surface area enhancement matrix (ESM). Coolant flow is assumed to be through the porous media in the xz-plane whereas conduction (q_y,) is predominantly in the y-direction, so that heat flows primarily along the axis of y-filaments and then by convection to the coolant, with the z- and z-axis filaments acting as fins. Thermal properties can be tuned (and anisotropy introduced) by specification of different filament diameter, pitch or cross-section shape for the x-, y- and z-axis filaments. It is noted that the box-lattice extended surface presents a significant contact area to a wall that lies in the x-z plane.

In technical papers stemming from this work, Gullbrand et al. [2005] considered laminar and turbulent single-phase convection in circular cross section filament box lattices. Their work shows that steady laminar flow persists up to at least a Reynolds number of 150, with transition to unsteady flow at a Reynolds number of 440. Balantrapu et al. [2005] developed models for porosity, ε specific surface area, and dimensionless effective thermal conductivity, Ke of circular

Figure 1.4: Elliptic cross section filament box lattice monolithic structure.

cross section box lattices[2]. They have shown that metal fraction, dimensionless specific surface area and dimensionless effective thermal conductivity can range as: $0 \leq 1\text{-}\varepsilon \leq 0.94$, $0.93 \leq \beta d_y \leq \pi$ and $0 \leq Ke \leq \pi/4$. Sarde et al. [2006] developed similar geometric models for elliptic cross section box lattices. Their CFD simulations show that laminar flow persists to a mesh Reynolds number of 150. Friction factors are found to be about the same as those obtained with circular cross section filament box lattices while Stanton numbers (single phase convection) are approximately 50% greater.

It can be shown, based on the work of Park et al. [2002] that the performance of such structures deployed as single-phase heat exchanger extended surfaces is approximately proportional to $\sqrt{\beta \cdot ke}$. Therefore exchanger surfaces having both large specific surface area and effective thermal conductivity are expected to exhibit superior thermal performance. Figure 1.5 compares the $\beta d_y Ke_y$-product of the above
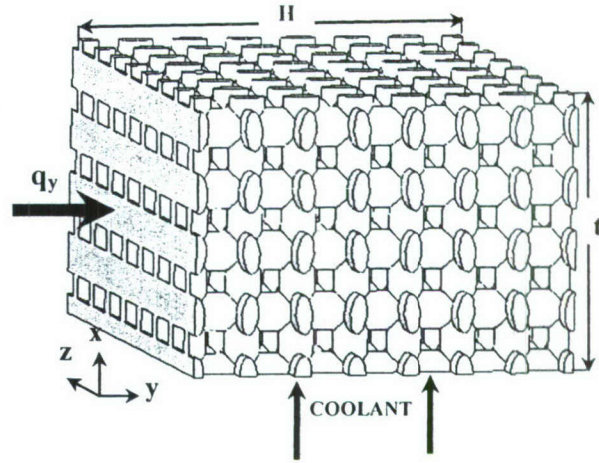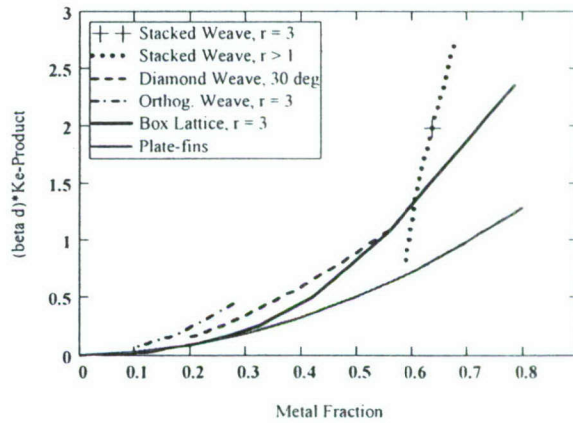

Fig. 1.5 $\sqrt{\beta d Ke_y}$ -product for representative structured porous media

---

[2] $Ke = ke/ks$ where ks is the filament thermal conductivity.

referenced structures with the $\beta t Ke_y$-product of a plate-fin extended surface, as a function of metal fraction $(1-\varepsilon)$. The plate-fin metal fraction is varied by varying the fin thickness-to-spacing ratio (t/P). With reference to the reticulated-filament structures $r = D_y/D_x$, with $D_x = D_z$ (3-filament structures). The diameter ratio r > 1 introduces anisotropy, resulting in an increase in effective thermal conductivity in the y-direction. Changes in filament pitch or weave angle will also introduce anisotropy. Figure 1.5 shows that the $\beta d_y Ke_y$-product of all of the reticulated filament structures shown have superior $\beta d_y Ke_y$-products relative to a traditional area enhancement[3]. This is because the reticulated filament structures have additional elements that increase their surface area per unit volume. Furthermore, filaments can be oriented to promote conduction in a particular direction. Finally, the structures are robust in that, while they are made up of very fine filaments, the aggregate structure is quite rigid.

1.1   Scope of Work

We were initially interested in woven-mesh AORS. The wire intersections would be jointed through vacuum or salt-bath brazing. A further study indicated that woven-mesh structures have relatively poor mechanical properties [Wirtz et al, 2003]. In addition, it became clear that the current weaving technology in the United States did not allow for reliable and quality fabrication of the woven-mesh structures. The wire intersection joints were difficult to bond either though brazing or diffusion bonding. An alternative was found to be a box lattice structure as shown in Fig.1-4. Such a structure has a much higher stiffness and strength than a woven-mesh AORS. Additionally, as mentioned in the above discussion, filaments can be configured to have wide ranging porosity, a large specific surface area and a large effective thermal conductivity in a particular direction, ke.

The overall objective of the research is to develop a methodology so that all the structural and thermal attributes of an AORS can be designed to achieve a high-performance heat exchanger matrix that possesses desirable strength, compliance or stiffness, and shock tolerance capabilities.

In Chapter 2, geometric models of porosity, specific surface area and effective thermal conductivity are developed for anisotropic box lattices having either circular cross section

---

[3] The $\beta d_y Ke_y$-product of a three-filament stacked weave is a function of (r) only. The cross symbol (+) shows the r = 3 solution.

filaments (Geometry I) or elliptic cross section filaments (Geometry II). In Chapter 3, single-phase flow and convection in Geometry I and II box lattice laminates (Fig. 1.4) are simulated with a CFD code. Both laminar and turbulent flows are considered. In Chapter 4, results of an experimental study of flow boiling of FC-72 in a screen laminate ESM are reported.

The mechanical characterization part of the research (Chapter 5) includes predictions of the deformation and failure of a box lattice structure subjected to external loading. A concentration is placed on the development and validation of a mechanical failure model. A high strength aluminum alloy was selected as a potential material for the box lattice heat exchanger structure. The characteristic material properties were obtained through basic experiments. Fabrication of the box lattice samples using EDM is documented. Results obtained from a systematic experimental investigation are reported. The failure models developed were validated with the experimental results.

2. Porosity, Specific Surface Area and Effective Thermal Conductivity of Box-Lattice Matrices

Analytical models for porosity, specific surface area and effective thermal conductivity of box lattices (Fig. 1.4) are developed. Two filament shapes are considered:

Geometry I: Filaments have circular cross sections. Anisotropy is introduced by changing the y-axis filament diameter or pitch relative to the x- and z-axis filament diameters or pitches.

Geometry II: Filaments have elliptic cross sections. Major/minor axes are arranged to promote streamline flow through the matrix, as shown in Fig. 1.4. Anisotropy is introduced by changing the ellipticity or pitch of the y-axis filaments relative to the x- or z-axis filaments

2.1 Geometry I: Circular Cross-Section Filament Box-Lattice Structures

Analytical models for porosity and specific surface area are developed by considering the unit cell shown in Fig. 2.1. The dimensions of the unit cell are $P_x P_y P_z$. The unit cell element consists of a y-direction circular cross section cylinder having diameter $2R_y$ and length P_y together with a cruciform shape, which includes the x-direction and z-direction cylinders. The x- and z-direction filaments have dimensions ($2R_x = D_x$, P_x) and ($2R_z = D_z$, P_z), respectively. For the present study, it is assumed that $2R_x = 2R_z$ and $P_x = P_z$.
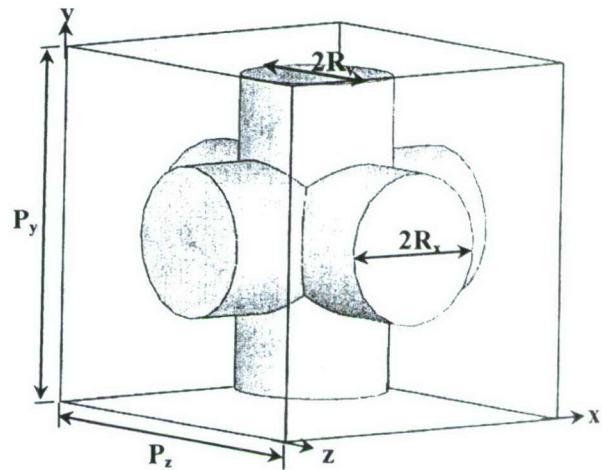
Fig.2.1 Solid Unit Cell-Circular cross-section

Porosity (ε) A geometric model for porosity for anisotropic box lattices is developed in terms of metal fraction of a single unit cell,

$$1 - \varepsilon = \frac{V_{Solid}}{P_x P_y P_z} = \overline{V}_{solid}$$

<div align="right">(2.1)</div>

To calculate the volume of solid in the unit cell, individual cylinders in the x-, y- z- direction are considered. Surplus material from x- and z-direction filaments is removed as shown in Fig. 2.2.
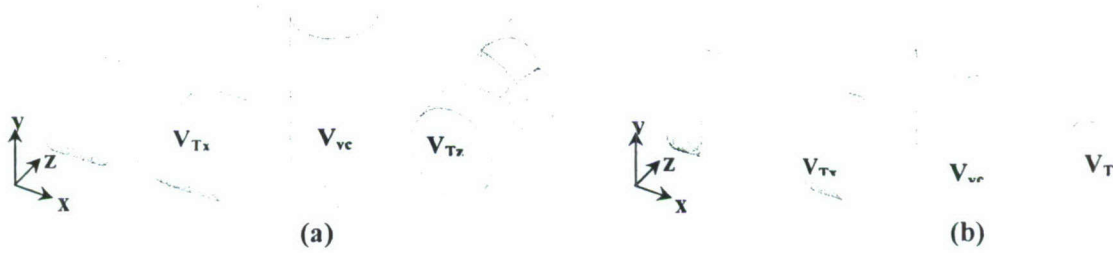

Fig. 2.2 Volumes required forming the solid structure in (a) Configuration 1 and (b) Configuration 2

The remaining components are assembled to form the solid shown in Fig. 2.1. The solid volume can then be written as

$$1 - \varepsilon = \overline{V}_{yc} + \overline{V}_{Tx} + \overline{V}_{Tz}$$

<div align="right">(2.2)</div>

The diameter of the y-filament when varied with respect to the diameter of the horizontal filaments (x- and z-filaments), leads to two cases of calculation as shown in Fig. 2.3. The two configurations are

Configuration 1: $R_x \leq R_y \leq \sqrt{2}R_x$, the y-axis filament diameter is enclosed within the cruciform intersection.

Configuration 2: $R_y \geq \sqrt{2}R_x$, the cruciform intersection is enclosed within the y-axis filament diameter.

$R_y < \sqrt{2} R_x$ $R_y = \sqrt{2} R_x$ $R_y > \sqrt{2}R_x$
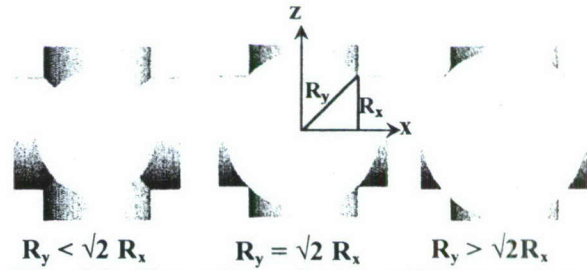
Fig. 2.3 Top view of the solid structure illustrating the two cases

In Eq. (2.2) $\overline{V}_{Tx}$, $\overline{V}_{yc}$ and $\overline{V}_{Tz}$ are the final volumes of the filaments in y-, x- and z- directions, respectively, normalized by the volume of unit cell. These elements are shown in Fig. 2.3. $\overline{V}_{yc}$ represents the volume of the whole filament in the y-direction,

$$\overline{V}_{yc} = \frac{\pi R_y^2 P_y}{P_x^2 P_y} \tag{2.3}$$

Consider the x-axis filament volume.

$$\overline{V}_{Tx} = \overline{V}_{xc} - \overline{V}_{xp} \tag{2.4}$$

$\overline{V}_{xc}$ is the volume of whole cylinder in x- direction and $\overline{V}_{xp}$ is that part of the volume that is removed to form the cruciform.

$$\overline{V}_{xc} = \frac{\pi R_x^2 P_x}{P_x^2 P_y} \tag{2.5}$$

$$\overline{V}_{xp} = \frac{8}{P_x^2 P_y} \left[\int_0^{R_x} \int_0^{\sqrt{R_y^2+y^2-R_x^2}} \sqrt{R_x^2 - y^2}\, dxdy + \int_{\sqrt{R_y^2-R_x^2}}^{R_y} \int_0^{\sqrt{R_x^2+x^2-R_y^2}} \sqrt{R_y^2 - x^2}\, dydx \right] \tag{2.6}$$

The volume, $\overline{V}_{Tz}$ is different for Configurations 1 and 2. In Configuration 2 the extra volume to be removed from the z-filament is exactly the part that lies inside the y-filament volume. Therefore, for Configuration 1:

$$\overline{V}_{Tz} = \overline{V}_{zc} - \left(\overline{V}_{zp} + \overline{V}_{zfp} \right) \tag{2.7}$$

and for Configuration 2:

$$\overline{V}_{Tz} = \overline{V}_{zc} - \overline{V}_{zp} \tag{2.8}$$

where,

$$\overline{V}_{xc} = \overline{V}_{zc} \tag{2.9}$$

$$\overline{V}_{xp} = \overline{V}_{zp} \tag{2.10}$$

$$\overline{V}_{zfp} = \frac{16}{P_x^2 \cdot P_y} \int\limits_{\sqrt{\frac{R_y^2}{2}}}^{R_x} \int\limits_{\sqrt{R_x^2 - z^2}}^{z} \sqrt{R_x^2 - z^2}\, dxdz \tag{2.11}$$

To enable scaling of the results and to simplify the equations, non-dimensional parameters are introduced.

$$r = \frac{R_y}{R_x} \tag{2.12}$$

$$\overline{P}_x = \frac{P_x}{2R_y} \tag{2.13}$$

$$\overline{P}_y = \frac{P_y}{2R_x} \tag{2.14}$$

Equations 2.3 – 2.11 can be written as follows:

$$\overline{V}_{yc} = \frac{\pi}{4 \cdot \overline{P}_y^2} \tag{2.15}$$

$$\overline{V}_{xc} = \overline{V}_{zc} = \frac{\pi}{4 \cdot \overline{P}_y \cdot \overline{P}_y \cdot r} \tag{2.16}$$

$$\overline{V}_{xp} = \overline{V}_{zp} = \int\limits_{0}^{\frac{1}{r}} \int\limits_{0}^{\sqrt{r^2(y+1)-1}} \frac{\sqrt{1 - y^2 \cdot r^2}}{\overline{P}_y \cdot \overline{P}_x^2 \cdot r}\, dxdy + \int\limits_{\sqrt{r^2-1}}^{r} \int\limits_{0}^{\sqrt{\frac{x^2+1}{r^2}-1}} \frac{\sqrt{r^2 - x^2}}{\overline{P}_y \cdot \overline{P}_x^2 \cdot r}\, dydx \tag{2.17}$$

· Note: Rx = Rz, Px = Pz and $\overline{P}_x = \overline{P}_z$

$$\overline{V}_{zfp} = \int\limits_{\sqrt{\frac{r^2}{2}}}^{1} \int\limits_{\sqrt{r^2-z^2}}^{z} \frac{2\sqrt{1 - z^2}}{\overline{P}_y \cdot \overline{P}_x^2 \cdot r^2}\, dxdz \tag{2.18}$$

13

Table 1 compares the results of the current model with numerical estimates from a solid modeling code [ProEngineer/Wildfire]. Integral expressions, Eqs. 2.17 and 2.18, are evaluated using an adaptive Romberg solver. Three cases of geometry are considered with varying diameters and pitches. There is a negligible difference when compared to the numerical estimates of the solid modeling code. The model is verified for asymptotic limits where P_y/D_x is large, P_x/D_x and r are equal to 1. It is observed that the volume fraction is equal to $\pi/4$, i.e. the volume of single cylinder in a box.

TABLE 1 Comparison of *1-ε* from current model with Solid Modeling Code Estimates

r	$\overline{P}_x$	$\overline{P}_y$	*1-ε* (Solid Modeling Software)	*1-ε* (Present)	% Difference
1	1.550	1.55	0.60095	0.60094	< .01%
2	1.025	1.05	0.78832	0.78834	< .01%
2	1.055	1.10	0.76568	0.76567	< .01%
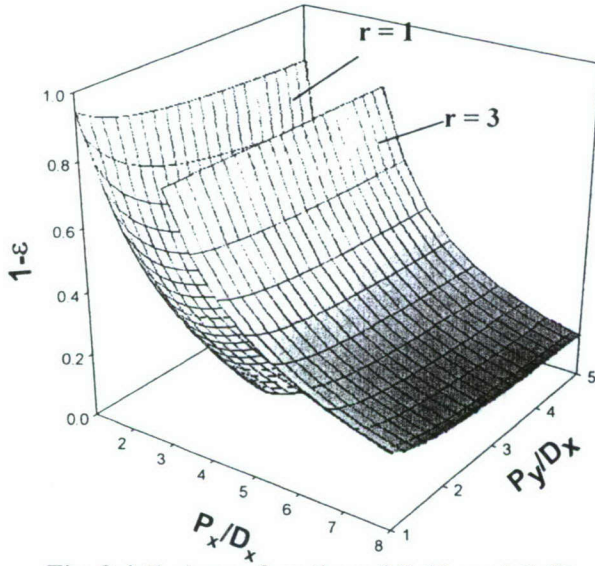
Fig. 2.4 (1-ε) as a function of P_x/D_x and P_y/D_x

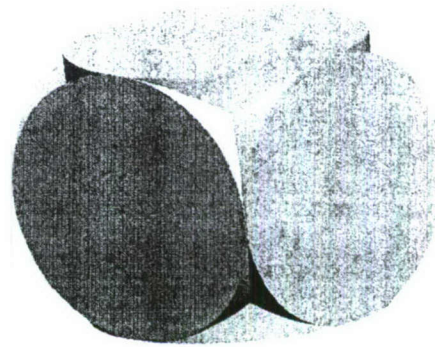Fig. 2.5 Box Lattice with Maximum metal fraction and minimum surface area

Figure 2.4 is a surface plot of the volume fraction (*1-ε*) plotted against the two dimensionless parameters $\overline{P}_x r = P_x / D_x$ and $\overline{P}_y$ for two values of r, $r=1$ and $r=3$. It is observed that the volume fraction decreases with increasing P_x/D_x and remains essentially constant as P_y increases.

When the model is tested under the limit $P_x/D_x = 1$, $r=1$, and $P_y/D_x = 1$, $1-\varepsilon$ is observed to be 0.942. This limit corresponds to the densest configuration of the unit cell, as shown in Fig. 2.5.

Specific surface area (β) The specific surface area (β) is defined as the ratio of the surface area of the solid in the unit cell to the volume of the unit cell.

$$\beta = \frac{S_{Solid}}{P_x P_y P_z} \tag{2.19}$$

The calculation of specific surface area employs the same methodology as used for the metal fraction calculation. To model the surface of the structure shown in Fig. 2.1, the x-, y- and z- direction circular cross section filament surfaces, with areas $\overline{S}_{xc}$, $\overline{S}_{yc}$ and $\overline{S}_{zc}$, are considered. Pieces having areas, $\overline{S}_{xp}$, $\overline{S}_{yp}$ and $\overline{S}_{zp}$ are removed so that the remaining surfaces shown in Fig. 2.6 fit together to form the completely hollow surface shown in Fig. 2.1.

As shown in Fig. 2.6 the filament surface area are different for Configurations 1 and 2. To

(a)   (b)
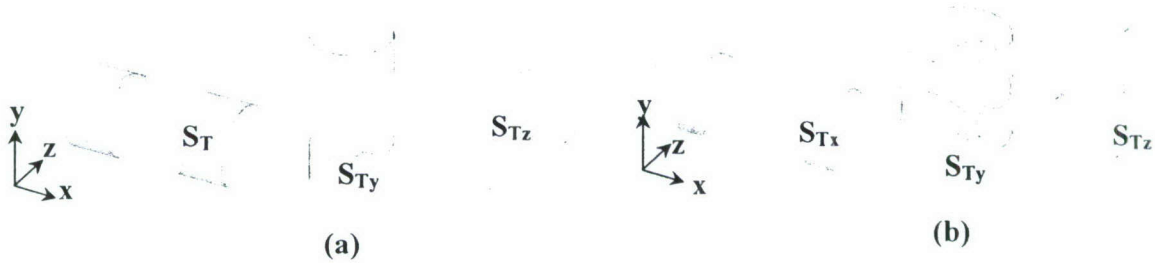
Fig.2.6 Final surface areas of the filaments in x-,y- and z- directions for (a) Configuration 1 and (b) Configuration 2

express the specific surface area in terms of non-dimensional parameters (Eqs. 2.12-2.14), the product of β and y filament diameter, $D_y = 2R_y$ is considered where

$$\beta D_y = \overline{S}_{Tx} + \overline{S}_{Ty} + \overline{S}_{Tz} \tag{2.20}$$

For Configuration 1,

$$\overline{S}_{Tx} = \overline{S}_{Tz} = \overline{S}_{xc} - (\overline{S}_{xp} + \overline{S}_{xfp}) \tag{2.21}$$

and for Configuration 2:

$$\overline{S}_{Tx} = \overline{S}_{Tz} = \overline{S}_{xc} - \overline{S}_{xp} \tag{2.22}$$

15

with,

$$\overline{S}_{xc} = \frac{2\pi R_x P_x D_y}{P_x^2 P_y} \tag{2.23}$$

$$\overline{S}_{xp} = \frac{D_y}{P_x^2 P_y} \int_0^{2\pi} \int_{-\sqrt{R_y^2 - R_x^2 \cos^2\theta}}^{\sqrt{R_y^2 - R_x^2 \cos^2\theta}} R_x \, dz \, d\theta \tag{2.24}$$

$$\overline{S}_{xfp} = \frac{D_y}{P_x^2 P_y} \int_{-\theta_3}^{\theta_3} \int_{-\sqrt{R_y^2 - R_x^2 \cos^2\theta}}^{\sqrt{R_y^2 - R_x^2 \sin^2\theta}} R_x \, dz \, d\theta \tag{2.25}$$

and

$$\theta_3 = \cos^{-1}\left(\frac{R_y}{\sqrt{2}R_x}\right) \tag{2.26}$$

Similarly for the y-filament, for Configuration 1:

$$\overline{S}_{Ty} = \overline{S}_{yc} - (\overline{S}_{yp} - \overline{S}_{yfp}) \tag{2.27}$$

and for Configuration 2:

$$\overline{S}_{Ty} = \overline{S}_{yc} - \overline{S}_{yp} \tag{2.28}$$

where,

$$\overline{S}_{yc} = \frac{\pi D_y^2 P_y}{P_x^2 P_y} \tag{2.29}$$

$$\overline{S}_{yp} = \frac{D_y}{P_x^2 P_y} \int_{-\theta_1}^{\theta_1} \int_{-\sqrt{R_x^2 - R_y^2 \sin^2\theta}}^{\sqrt{R_x^2 - R_y^2 \sin^2\theta}} R_y \, dz \, d\theta \tag{2.30}$$

$$\theta_1 = \sin^{-1}\left(\frac{R_x}{R_y}\right) \tag{2.31}$$

$$\overline{S}_{yfp} = \frac{D_y}{P_x^2 \cdot P_y}\left[\int_{\frac{\pi}{4}}^{\frac{\pi}{4}+\theta_2} \int_{-\sqrt{R_x^2 - R_y^2 \cos^2\theta}}^{\sqrt{R_x^2 - R_y^2 \cos^2\theta}} R_y \, dz \, d\theta - \int_{\frac{\pi}{4}+\theta_1}^{\frac{\pi}{4}} \int_{-\sqrt{R_x^2 - R_y^2 \cos^2\theta}}^{\sqrt{R_x^2 - R_y^2 \cos^2\theta}} R_y \, d\theta \, dz \right] \tag{2.32}$$

16

$$\theta_2 = \cos^{-1}\left(\frac{R_x}{R_y}\right) \tag{2.33}$$

The specific surface area is defined in terms of dimensionless parameters in Eqs. (2.12-2.14).

$$\overline{S}_{xc} = \frac{\pi}{\overline{P}_x^2} \tag{2.34}$$

$$\overline{S}_{xp} = \int\limits_0^{2\pi} \int\limits_0^{\sqrt{r^2 - \cos^2\theta}} \frac{1}{2r\overline{P}_x^2\overline{P}_y} dz\, d\theta \tag{2.35}$$

$$\overline{S}_{xfp} = \int\limits_0^{\theta_3} \int\limits_{-\sqrt{r^2-\cos^2\theta}}^{\sqrt{1-\sin^2\theta}} \frac{1}{2r\overline{P}_x^2\overline{P}_y} dz\, d\theta \tag{2.36}$$

$$\theta_3 = \cos^{-1}\left(\frac{r}{\sqrt{2}}\right) \tag{2.37}$$

$$\overline{S}_{yc} = \frac{\pi}{\overline{P}_x\overline{P}_y} \tag{2.38}$$

$$\overline{S}_{xp} = \int\limits_0^{\theta_1} \int\limits_0^{\sqrt{1-r^2\sin^2\theta}} \frac{1}{\overline{P}_x^2\overline{P}_y} dz\, d\theta \tag{2.39}$$

$$\theta_1 = \sin^{-1}\left(\frac{1}{r}\right) \tag{2.40}$$

$$\overline{S}_{xfp} = \int\limits_{\frac{\pi}{4}}^{\frac{\pi}{4}+\theta_2} \int\limits_0^{\sqrt{1-r^2\cos^2\theta}} \frac{1}{\overline{P}_x^2\overline{P}_y} dz\, d\theta \tag{2.41}$$

$$\theta_2 = \cos^{-1}\left(\frac{1}{r}\right) \tag{2.42}$$

The model, Eqs. 2.34 – 2.40, is also benchmarked against numerical estimates of ProEngineer/Wildfire. Table 2 compares results of the current model with the solid modeling

software predictions. In all cases considered it is observed that the difference is negligible. For the validation of the model, it is tested for asymptotic limits where P_y/D_x is large and P_x/D_x and r are equal to 1. This limit represents a single vertical cylinder in the unit cell. Therefore, we get a value of π.

TABLE 2 Comparison of βD_y from current model with Solid Modeling Code Estimates

r	$\overline{P}_x$	$\overline{P}_y$	βD_y(Solid Modeling Software)	βD_y (Present)	% Difference
1	1.55	1.55	1.6640	1.6639	< .01%
2	1.025	1.05	2.034071	2.034063	< .01%
2	1.055	1.1	2.109306	2.109296	< .01%

Figure 2.7 is a surface plot of βD_y against the two dimensionless parameters $\overline{P}_x r = P_x / D_x$ and P_y/D_x for two values of r. The graph shows that βD_y increases with increasing radius ratio. An increase in P_x results in decrease in βD_y. Variations in P_y have less impact on the βD_y. From Fig. 2.5, the densest configuration in a unit cell, we can conclude that the 0.939 is the lowest limit of βD_y.

Fig. 2.7 βD_y as a function of P_x/D_x and P_y/D_x

Effective Thermal Conductivity Assume there is a vertical temperature gradient across the unit cell so that heat is conducted is along the vertical filament and across the horizontal-filament cruciform of Fig. 2.8. The effective thermal conductivity, ke_y can be defined such that

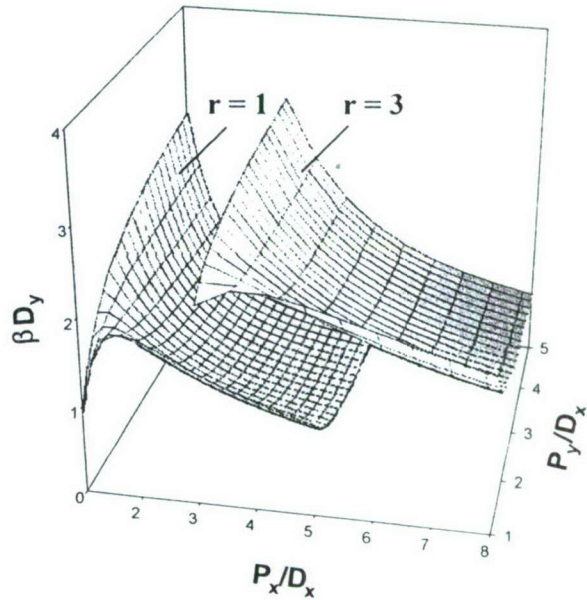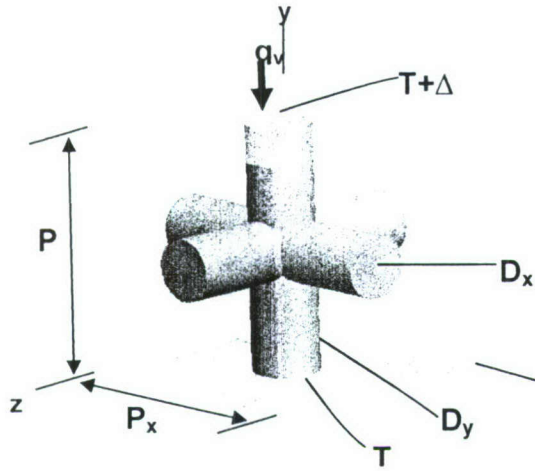$$q_y = ke_y \frac{P_x^2 \Delta T}{P_y} \qquad (2.43)$$

18

Fig. 2.8 Unit Cell with temperature   Fig. 2.9 Transformed Unit Cell
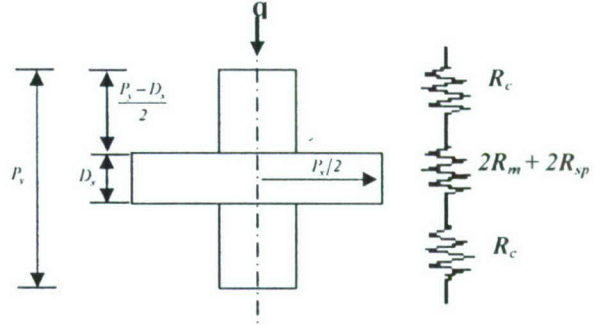
We model the cruciform structure as a disk of diameter P_x and thickness D_x, where the vertical-filament segment/disk interface is assumed to be isothermal, as shown in Fig. 2.9 Then, with reference to the thermal circuit (Fig. 2.9)

$$ke_y = \frac{P_y}{P_x^2 (2R_c + 2R_m + 2R_{sp})} \tag{2.44}$$

where $2R_c$ is the 1-D thermal resistance of the vertical-filament segments above and below the horizontal disk,

$$2R_c = \frac{P_y - D_x}{\frac{\pi}{4} k_s D_y^2}, \tag{2.45}$$

With k_s he thermal conductivity of the filament material. The quantity $2(R_m + R_{sp})$ is the thermal resistance across the horizontal disk, where $2R_m$ and $2R_{sp}$ are material and spreading thermal resistances, respectively

$$2R_m = \frac{D_x}{\frac{\pi}{4} ke_m P_x^2} \tag{2.46}$$

and

$$2R_{sp} = \frac{\psi}{ke_m D_y \sqrt{\pi}} \tag{2.47}$$

19

ψ is the dimensionless spreading resistance for the disk ,

$$\psi = \frac{1}{2}\left[1 - \frac{D_y}{P_x}\right]^{\frac{3}{2}} \tanh \lambda_c \frac{D_x}{P_x} \tag{2.48}$$

and λ_c is the approximate solution characteristic [Lee et al, 1995]

$$\lambda_c = \pi + \frac{1}{\sqrt{\pi}\left(\dfrac{D_y}{P_x}\right)} \tag{2.49}$$

The effective thermal conductivity of the disk (ke_m in Eqs. 2.46, 2.47) is the thermal conductivity of the filament material, k_s weighted by the ratio of the (approximate) cruciform volume to disk volume, where C is an arbitrary constant.

$$ke_m = C\,k_s\,\frac{\dfrac{\pi}{4}D_x^{\,2}(2P_x)}{\dfrac{\pi}{4}P_x^{\,2}D_x} = C\,k_s\,\frac{2D_x}{P_x} \tag{2.50}$$

When expressed in terms of non-dimensional parameters, Eqs. (2.12 – 2.14), the dimensionless effective thermal conductivity can be written as:

$$Ke_y = \frac{ke_y}{k_s} = \frac{\dfrac{\pi}{4}}{2(\overline{R}_c + \overline{R}_m + \overline{R}_{sp})} \tag{2.51}$$

where

$$\overline{R}_c = \overline{P}_x^{\,2}\left(1 - \frac{1}{\overline{P}_y}\right) \tag{2.52}$$

$$\overline{R}_m = \frac{1}{F\overline{P}_y} \tag{2.53}$$

$$\overline{R}_{sp} = \frac{\sqrt{\pi}\,r\,\overline{P}_x^{\,2}\,\overline{\psi}}{F\overline{P}_y} \tag{2.54}$$

20

$$F = \frac{2C}{r\overline{P}_x} \tag{2.55}$$

$$\overline{\psi} = \frac{1}{2}\left[1 - \frac{1}{\overline{P}_x}\right]^{\frac{3}{2}} \tanh\left(\frac{\overline{\lambda}_c}{r\overline{P}_x}\right) \tag{2.56}$$

$$\overline{\lambda}_c = \pi + \frac{\overline{P}_x}{\sqrt{\pi}} \tag{2.57}$$

TABLE 1 Comparison of Key estimates to present model and finite volume code; $C = 1.4$

r	$\overline{P}_x$	$\overline{P}_y$	Ke_y (F.V. Code)	Ke_y (Present)	% Difference
1	1.55	1.55	0.4385	0.4357	0.6
1.5	1.33	2	0.5154	0.5039	2.2
1.5	1.55	2.33	0.3776	0.362	4.1
2	1.16	4.67	0.6123	0.5916	3.5
3	1.15	6.92	0.6192	0.5914	4.7

The model, Eqs. (2.51 – 2.57), is calibrated to determine an appropriate value of the arbitrary constant, C (Eq. 2.50) by comparison with numerical computations of Ke_y obtained from a finite volume code [Fluent]. Results are summarized in Table 1 where it is shown that $C = 1.4$ results in an rms difference between the two methods is 3.4 %.

Figure 2.10 shows a surface plot of Ke_y versus P_x/D_x and P_y/D_x for diameter ratios, $r = 1$ and 3. It is observed that higher diameter ratios result in an increase in effective thermal conductivity, and Ke_y is inversely proportional to P_x/D_x. Furthermore, variations of the vertical pitch of the horizontal cruciform have a negligible impact on the effective thermal conductivity. However, because of the physical limitations of the geometry, there are
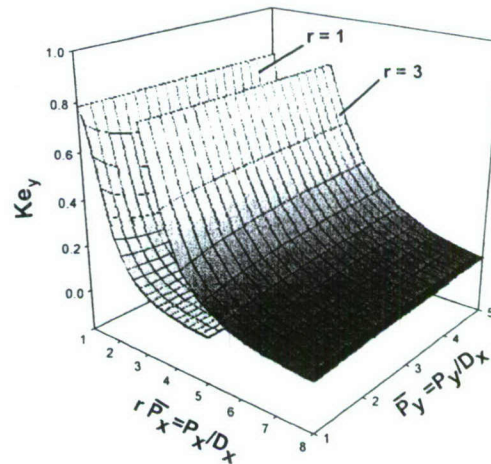

Fig. 2.10 Effective Thermal Conductivity circular cross section filament box lattice.

limiting conditions applied over the model. For $P_x/D_x=1$, with any value of r, and $\overline{P}_y$, the value of effective thermal conductivity does not exceed $\pi/4$.

In summary, an analytical model for effective thermal conductivity is developed by considering the unit cell shown in Fig. 2.8. The dimensionless effective thermal conductivity is shown to be a function of three non-dimensional parameters: $r = \dfrac{D_y}{D_x}$, $\overline{P}_x = \dfrac{P_x}{D_y}$, $\overline{P}_y = \dfrac{P_y}{D_x}$. The effective thermal conductivity model is based on the assumption that a disk of reduced thermal conductivity (Eq. 2.50) can represent the horizontal cruciform component. The model shows that the dimensionless effective thermal conductivity, Ke_y increases with increasing r, and decreasing $\overline{P}_x$. When $\overline{P}_x \to 1$ for any value of r, Ke_y has a maximum value of $\pi/4$. It is also observed that $\overline{P}_y$ has a negligible effect on Ke_y.

2.2 Geometry II: Elliptic cross-section filament box-lattice structures

Analytical models for porosity and specific surface area are developed by considering the unit cell shown in Fig. 2.11. The dimensions of the unit cell are $P_xP_yP_z$. The unit cell element consists of a y-direction elliptic cross section cylinder having major and minor diameters $2R_y$, $2r_y$, respectively; and, length P_y together with a cruciform shape, which includes the x-direction and z-direction elliptic cylinders. The x- and z-direction filaments have $2R_x$, $2r_x$, P_x and $2R_z$, $2r_z$, P_z dimensions
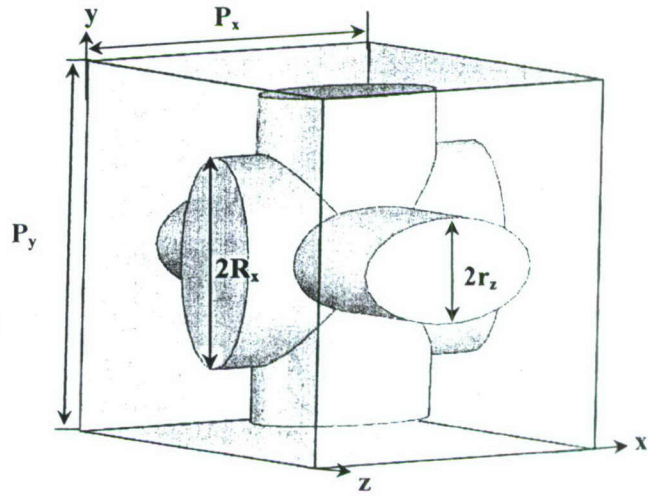

Fig.2.11 Unit Cell with elliptic cross-section filaments.

respectively. For the present study it is assumed that $2R_y = 2R_z$ and $2r_y = 2r_x$. It is noted with reference to Fig. 10 that physically realizable structures such as the one shown in Fig. 1 must have $2R_x \le P_y$, $2r_x \le P_z$, etc.
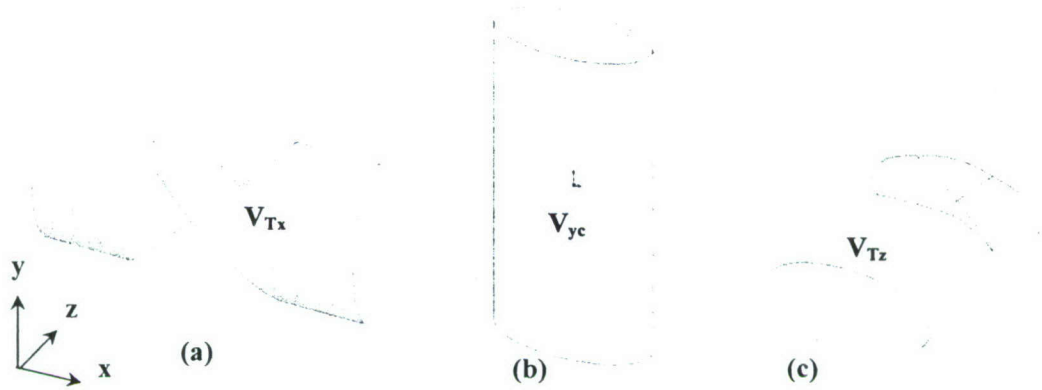
Fig. 2.12 Volumes required to form the solid structure in x-, y-, z-direction respectively

Porosity (ε) Similar to the cylinders model for porosity, a geometric model for porosity for anisotropic box lattices with elliptic cross section filaments is developed in terms of metal fraction of a single unit cell (Fig. 2.11). To calculate the volume of solid in the unit cell, individual cylinders in the x-, y- z- direction are considered. Surplus material from x- and z-direction filaments is removed as shown in Fig. 2.12. The remaining components are assembled to form the solid shown in Fig. 2.11. The solid volume can then be written as

$$1 - \varepsilon = \overline{V}_{yc} + \overline{V}_{Tx} + \overline{V}_{Tz} \tag{2.58}$$

where $\overline{V}_{Tx}$, $\overline{V}_{yc}$ and $\overline{V}_{Tz}$ are the final volumes of the filaments in y-, x- and z- directions, respectively, normalized by the volume of unit cell. $\overline{V}_{xc}$ is the volume of the whole cylinder in x- direction

$$\overline{V}_{yc} = \frac{\pi R_y r_y P_y}{P_x P_y P_Z} \tag{2.59}$$

$$\overline{V}_{Tx} = \overline{V}_{xc} - \overline{V}_{xp} \tag{2.60}$$

In Eq. (2.60), $\overline{V}_{xp}$ is that part of the volume that is removed to form the cruciform.

$$\overline{V}_{Tz} = \overline{V}_{zc} - \left(\overline{V}_{zp} + \overline{V}_{zfp}\right) \tag{2.61}$$

Similarly $\overline{V}_{zc}$ represents the volume of whole z-filament and $\overline{V}_{zp}$ and $\overline{V}_{zfp}$ represent the surplus volumes to be removed from the z-filament to enable a perfect fit with the cruciform already constructed from the x- and y- filaments

$$\overline{V}_{xc} = \frac{\pi R_x r_x P_x}{P_x P_y P_Z} \tag{2.61}$$

$$\overline{V}_{xp} = \frac{8}{P_x P_y P_z} \left[\begin{array}{l} \int\limits_{0}^{R_x} \int\limits_{0}^{y\frac{R_y}{R_x}} r_x \sqrt{1 - \frac{y^2}{R_x^2}}\, dxdy \quad + \\[4mm] \int\limits_{0}^{R_y} \int\limits_{0}^{x\frac{R_x}{R_y}} r_y \sqrt{1 - \frac{x^2}{R_y^2}}\, dydx \end{array} \right] \tag{2.62}$$

$$\overline{V}_{zc} = \frac{\pi R_z r_z P_z}{P_x P_y P_Z} \tag{2.63}$$

$$\overline{V}_{zp} = \frac{8}{P_z P_y P_z} \left[\begin{array}{l} \int\limits_{0}^{R_z} \int\limits_{0}^{r_x\sqrt{\frac{r_z^2}{R_x^2}\left(\frac{x^2}{R_z^2}-1\right)+1}} r_z \sqrt{1 - \frac{x^2}{R_z^2}}\, dzdx \quad + \\[4mm] \int\limits_{r_x\sqrt{1-\frac{r_z^2}{R_x^2}}}^{r_x} \int\limits_{0}^{R_z} R_x \sqrt{1 - \frac{z^2}{r_x^2}}\, dxdz \end{array} \right] \tag{2.64}$$

$$\overline{V}_{zfp} = \frac{8}{P_x P_y P_z} \left[\int\limits_{\frac{r_z R_x}{\sqrt{R_x^2+r_z^2}}r_x\sqrt{1-\left(\frac{y}{R_x}\right)^2}}^{r_z} \int\limits_{0}^{y\frac{r_y}{r_z}} R_z \sqrt{1 - \frac{y^2}{r_z^2}}\, dzdy + \int\limits_{\frac{r_y R_x}{\sqrt{R_x^2+r_z^2}}R_x\sqrt{1-\left(\frac{z}{r_x}\right)^2}}^{r_y} \int\limits_{0}^{z\frac{r_z}{r_y}} R_y \sqrt{1 - \frac{z^2}{r_y^2}}\, dydz \right] \tag{2.65}$$

24

To enable scaling of the results and to simplify the equations, non-dimensional parameters are introduced. Eqs (2.66 – 2.68) are aspect ratios (radius ratios) of the ellipses in x-, y- and z-directions, respectively. Pitch-to-radius ratios are shown in Eqs. (2.69 – 2.71). The values of aspect ratios are not less than 1 and similarly, dimensionless pitches are always greater than or equal to 2

$$a_x = \frac{R_x}{r_x} \quad (2.66) \qquad a_y = \frac{R_y}{r_y} \quad (2.67) \qquad a_z = \frac{R_z}{r_z} \quad (2.68)$$

$$\overline{P}_x = \frac{P_x}{R_y} \quad (2.69) \qquad \overline{P}_y = \frac{P_y}{R_x} \quad (2.70) \qquad \overline{P}_z = \frac{P_z}{r_y} \quad (2.71)$$

The components of metal fraction shown in Eq. (2.58) are expressed in terms of non-dimensional parameters:

$$\overline{V}_{yc} = \frac{\pi}{\overline{P}_x \overline{P}_z} \tag{2.72}$$

$$\overline{V}_{xc} = \frac{\pi}{\overline{P}_y \overline{P}_z} \tag{2.73}$$

$$\overline{V}_{xp} = \frac{8}{\overline{P}_x \overline{P}_y \overline{P}_z}\left[\int_0^1 \int_0^y \sqrt{1 - y^2}\, dxdy \;+\; \int_0^1 \int_0^x \sqrt{1 - x^2}\, dydx \right] \tag{2.74}$$

$$\overline{V}_{zc} = \frac{\pi a_y}{\overline{P}_y \overline{P}_z a_x a_z} \tag{2.75}$$

$$\overline{V}_{zp} = \frac{8}{\overline{P}_x \overline{P}_y \overline{P}_z}\left[\int_0^1 \int_0^{\sqrt{\left(\frac{a_y}{a_x a_z}\right)^2 (x^2-1)+1}} \frac{a_y}{a_z a_x}\sqrt{1-x^2}\, dzdx \;+\; \int_{\sqrt{1-\left(\frac{a_y}{a_x a_z}\right)^2}}^1 \int_0^{\sqrt{1-\left(\frac{a_x a_z}{a_y}\right)^2 (1-z^2)}} \sqrt{1-z^2}\, dxdz \right] \tag{2.76}$$

25

$$\overline{V}_{zfp} = \frac{8}{\overline{P}_x \overline{P}_y \overline{P}_z} \left[\int_{\frac{a_y}{\sqrt{a_y^2 + (a_x a_z)^2}}}^{\frac{a_y}{a_x a_z}} \int_{\sqrt{1-y^2}}^{\frac{y a_x a_z}{a_y}} \sqrt{1 - \left(\frac{y a_x a_z}{a_y}\right)^2} \, dz \, dy \; + \right.$$

$$\left. \int_{\frac{a_x a_z}{\sqrt{a_y^2 + (a_x a_z)^2}}}^{1} \int_{\sqrt{1-z^2}}^{\frac{z a_y}{a_x a_z}} \sqrt{1 - z^2} \, dy \, dz \right] \tag{2.77}$$

To study the effect of adding ellipticity to the filaments, metal fraction is plotted against aspect ratio in Fig. 2.13. The graph shows 1-ε versus aspect ratio at constant pitch-to-major radius ratios, P/R= 2, 4, 6. In the case shown all the aspect ratios and pitch-to-major radius ratios are considered equal. At aspect ratio, a=1 the filaments represent cylinders with circular cross section. The densest form of solid unit cell is attained at P/R = 2 (a physically realizable limit). The maximum
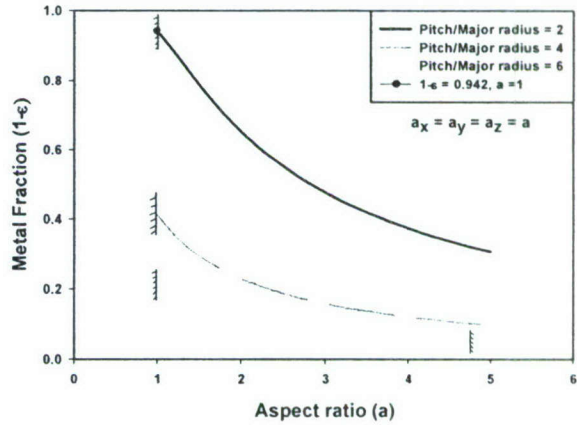

Fig. 2.13   1-ε Vs Aspect ratio; Effect of streamlining

value of metal fraction, 1-ε = 0.942 is shown in Fig. 2.13. It is observed from Fig. 2.13 that metal fraction decreases as aspect ratios increase. Furthermore, there is a decrease in metal fraction as pitch-to-radius ratio increases.

Fig. 2.14 plots metal fraction as a function of a_x/a_y. This graph illustrates the effect on the metal fraction of introducing anisotropy to the structure. It is observed that as a_x/a_y increases or the structure is tending towards isotropy, the metal fraction is decreasing.   Note, the endpoints of the curve represent physically realizable limits for the conditions shown in the legend.
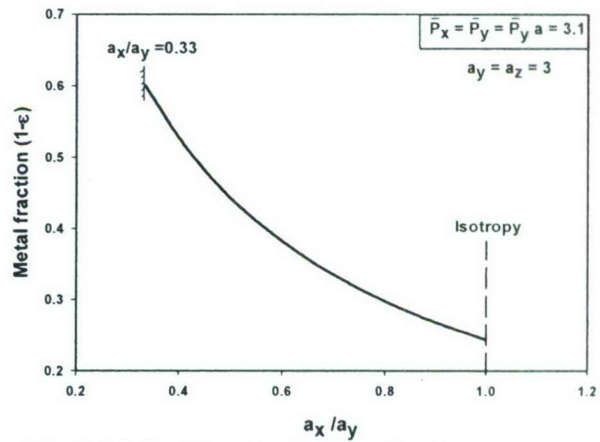

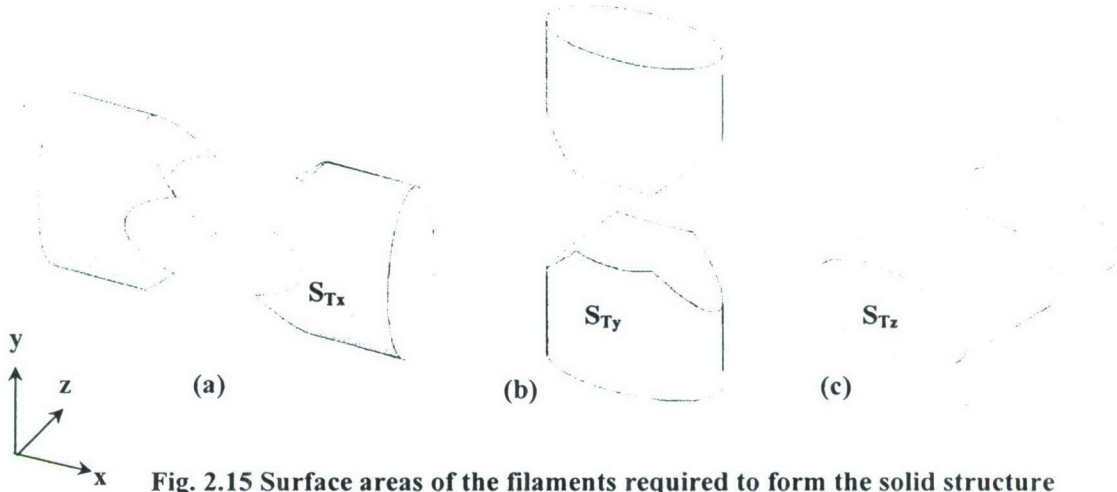Fig. 2.14 1-ε Vs a_x/a_y; Effect of anisotropy

Fig. 2.15 Surface areas of the filaments required to form the solid structure

Specific surface area (β) The calculation of specific surface area employs the same methodology as used for the metal fraction calculation. To model the surface of the structure shown in Fig. 2.11, the x-, y- and z-direction elliptic cross section filament surfaces, with areas $\overline{S}_{xc}$, $\overline{S}_{yc}$ and $\overline{S}_{zc}$, are considered. Pieces having areas, $\overline{S}_{xp}$, $\overline{S}_{yp}$ and $\overline{S}_{zp}$ are removed so that the remaining surfaces shown in Fig. 2.15 fit together to form the completely hollow surface shown in Fig. 2.11. To express the specific surface area in terms of non-dimensional parameters (Eqs. 2.66 – 2.71), the product of β and effective radius, $r_e = \sqrt{R_y r_y}$ is introduces.

$$\beta r_e = \overline{S}_{Tx} + \overline{S}_{Ty} + \overline{S}_{Tz} \qquad (2.78)$$

with

$$\overline{S}_{Tx} = \overline{S}_{xc} - \overline{S}_{xp} \qquad (2.79)$$

$$\overline{S}_{Ty} = \overline{S}_{yc} - \overline{S}_{yp} \qquad (2.80)$$

$$\overline{S}_{Tz} = \overline{S}_{zc} - \overline{S}_{zp} \qquad (2.81)$$

where $\overline{S}_{Tx}, \overline{S}_{Ty}, \overline{S}_{Tz}$ are the remaining area of the cylinder in x-, y- and z- direction as shown in Fig. 2.15. Following the analysis of circular cross section filaments, and introducing dimensionless parameters (Eqs 2.66 – 2.71)

27

$$\overline{S}_{xc} = \frac{4\sqrt{a_y}}{\overline{P}_z \overline{P}_y a_x} \left[\int_0^{\frac{\pi}{2}} \sqrt{\sin^2\theta + a_x^2 \cos^2\theta}\, d\theta \right] \qquad (2.82)$$

$$\overline{S}_{xp} = \frac{\sqrt{a_y}}{\overline{P}_x \overline{P}_y \overline{P}_z a_x} \left[\int_0^{tan^{-1}\left(\frac{a_y}{a_x a_z}\right)} \int_0^{\sqrt{1-\left(\frac{a_x a_z}{a_y}\sin\theta\right)^2}} \sqrt{\sin^2\theta + a_x^2 \cos^2\theta}\, dx d\theta + \right. $$
$$\left. \int_0^{tan^{-1}\left(\frac{a_y}{a_x a_z}\right)\cos\theta} \int_0 \sqrt{\sin^2\theta + a_x^2 \cos^2\theta}\, dx d\theta \right] \qquad (2.83)$$

$$\overline{S}_{yc} = \frac{4\sqrt{a_y}}{\overline{P}_z \overline{P}_x} \left[\int_0^{\frac{\pi}{2}} \sqrt{\sin^2\theta + \frac{\cos^2\theta}{a_y^2}}\, d\theta \right] \qquad (2.84)$$

$$\overline{S}_{yp} = \frac{\sqrt{a_y}}{\overline{P}_x \overline{P}_y \overline{P}_z} \left[\int_0^{tan^{-1}\left(\frac{a_x a_z}{a_y}\right)\cos\theta} \int_0 \sqrt{\sin^2\theta + \frac{\cos^2\theta}{a_y^2}}\, dy d\theta + \int_{tan^{-1}\left(\frac{a_x a_z}{a_y}\right)}^{\frac{\pi}{2}} \int_0^{\frac{a_y \sin\theta}{a_x a_z}} \sqrt{\sin^2\theta + \frac{\cos^2\theta}{a_y^2}}\, dy d\theta \right] \qquad (2.85)$$

$$\overline{S}_{zc} = \frac{4\sqrt{a_y}}{\overline{P}_x \overline{P}_y a_x} \left[\int_0^{\frac{\pi}{2}} \sqrt{\sin^2\theta + \frac{\cos^2\theta}{a_z^2}}\, d\theta \right] \qquad (2.86)$$

$$\overline{S}_{zp} = \frac{\sqrt{a_y}}{\overline{P}_x \overline{P}_y \overline{P}_z a_x} \left[\int_0^{tan^{-1}\left(\frac{a_y}{a_x a_z}\right)\cos\theta} \int_0 \sqrt{\sin^2\theta + \frac{\cos^2\theta}{a_z^2}}\, dz d\theta + \int_{tan^{-1}\left(\frac{a_y}{a_x a_z}\right)}^{\frac{\pi}{2}} \int_0^{\sin\theta} \sqrt{\sin^2\theta + \frac{\cos^2\theta}{a_z^2}}\, dz d\theta \right] \qquad (.2.87)$$

Figure 2.16 shows dimensionless specific surface area, βr_e plotted against aspect ratio holding metal fraction constant. The three cases considered are 1-ε = 0.26, 0.60 and 0.8, and all the aspect ratios and pitch to major radius ratios are considered equal. It is observed from the Fig. 2.17 that βr_e increases with the metal fraction. Adding ellipticity (increasing aspect ratio) also results in an increase in dimensionless specific surface area. Figure 2.17 shows the effect
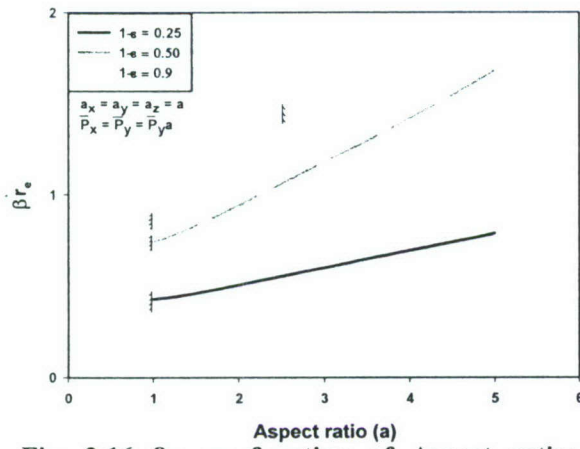
Fig. 2.16 βr_e as function of Aspect ratio: Effect of streamlining
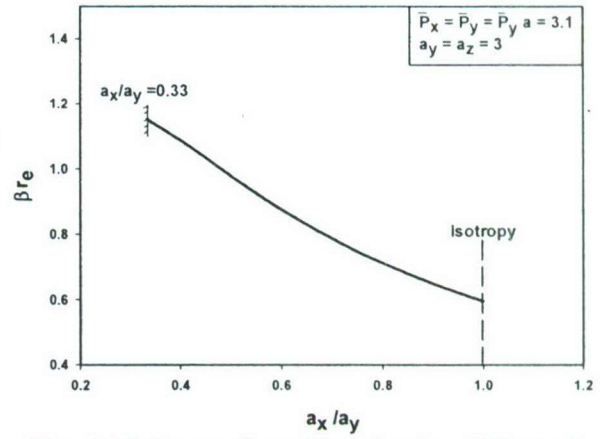

Fig. 2.17 βr_e as function of a_x/a_y: Effect of anisotropy

on βr_e of introducing anisotropy to the structure. As the value of a_x/a_y increases βr_e decreases and the structure tends toward isotropy $\left(\dfrac{a_x}{a_y} = 1\right)$.

29

3 Thermal/Fluid Characteristics of Box-Lattice Matrices: Single-Phase Convection

Monolithic box-lattice matrices (Fig. 1.4) can be configured as extended surface area enhancements (porous fins). Numerical simulations are performed to evaluate the flow and transport characteristics of these structures. In the simulations, the fluid is water with Pr = 7.0. The mesh Reynolds number range of interest is Re = 3 to 1000. Flow fields investigated are found to be both laminar and turbulent. The laminar flow fields are resolved using direct numerical simulations (DNS), while the turbulent flows are modeled using large eddy simulations (LES).

Box lattice matrices having equal sized (diameter and pitch) circular cross section filaments are studied as the base geometry. The effect of streamlining the flow through the array is evaluated by introduction of ellipticity to filament shape.

3.1   Heat Exchanger Implementation

As an example application of this technology, imagine that the box lattice matrix shown in the Figure 1.4 is deployed as an area enhancement between the plates of a plate-fin heat exchanger (plate spacing = H), as shown in Fig. 3.1. Heat conduction is primarily along the axis of y-filaments. The coolant flows in the x-direction. The filaments in x- and z- direction act as fins by increasing the surface area of the structure. Initially the
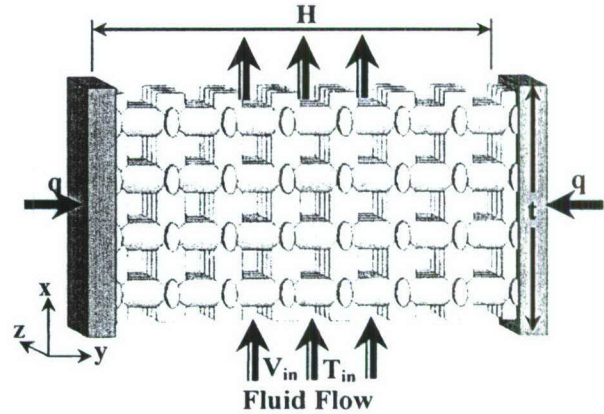
Fig. 3.1 Heat Exchanger Implementation

coolant approaches with a superficial velocity of V_{in} and temperature T_{in}. The coolant flows through the matrix and cools it by convection. The average pore velocity, V is related to the superficial velocity as: $V = \dfrac{V_{in}}{\varepsilon}$. The mesh Reynolds number that characterizes the flow is

$$Re = \frac{\rho V D_h}{\mu} \qquad (3.1)$$

where D_h is the pore hydraulic diameter,

$$D_h = \frac{4\varepsilon}{\beta} \qquad\qquad (3.2)$$

3.2 Flow Domain and Boundary Conditions

Since heat exchanger matrices consist of a large number of cells (or elements), and it is not feasible to resolve the flow field using the whole structure; rather one "unit cell" flow volume of the matrix, of dimension P_x x P_y x P_z, is used in the simulations. Studying flow and thermal characteristics of the unit cell is expected to give a good representation of the performance of the heat exchanger. However, the study of a single element will not show any entrance or wall effects. With a packed bed of spheres, wall effects are shown to influence the flow characteristics for the first 1.5 sphere diameters from the boundary walls [Mickley et al, 1965], while entrance effects may be important 2 P_x or more down stream.

The solution domain used in the numerical simulations is shown in Fig. 3.2. The outer dimensions of the domain have edge length P_x x P_y x P_z. Concave surfaces are fluid-to-filament surface interfaces. Plain surfaces are openings that connect to adjacent unit cell fluid volumes.

Fig. 3.2 Solution domain for numerical simulations.

The simulations are performed by applying a specified mass flow into the domain in the x-direction. Periodic boundary conditions are applied in the x-direction to enforce global mass conservation; the same amount of mass flow entering through the inlet plane also leaves through the outlet. The periodic boundary condition is also used for the lateral plane surfaces that are not in the main flow direction. These periodic conditions enforce mass conservation and allow the domain to interact with surrounding fluid domains in the matrix. If fluid is entering through one surface, the same amount must also leave through the opposite surface. Fluid can therefore pass in or out of the domain through the lateral planes that are not in the main flow direction.
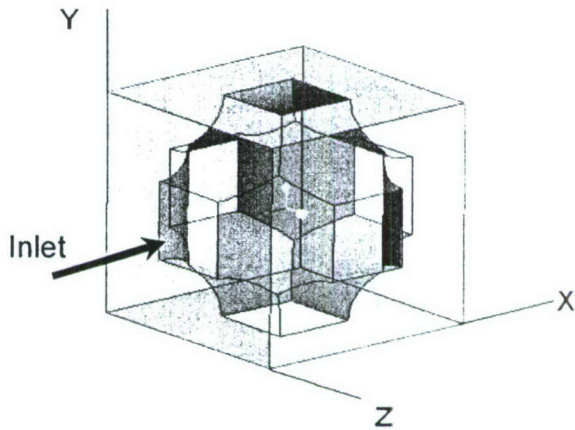
In the simulations, the fluid-solid interfaces are assumed to be isothermal at temperature, T_s. While the temperature drop over the whole exchange matrix may be substantial, the solid phase is approximated to be isothermal due to the unit cell's small size (mm-scale). This approximation can be justified by a simple scale analysis: Assume that the temperature difference between the wall and the approaching coolant is $T_{wall} - T_{in} = 10°C$, and the temperature drop across a 1 cm exchange matrix is 1°C (90 % efficiency), then the temperature drop across a 1 mm feature of the exchange matrix is 0.1°C or 1 % of the driving temperature difference.

The thermal boundary conditions for the openings are periodic. The inlet and the outlet temperatures of the fluid are different. But periodicity is applied by requiring that the dimensionless temperature,

$$\theta = \frac{T - T_{mean}}{T_s - T_{mean}} \tag{3.3}$$

at entrance and exit be equal resulting in a periodically fully developed flow. T_{mean} is the volume averaged temperature of the fluid.

All the simulations are started from a zero velocity field. Thereafter, the simulations are advanced in time. The low Reynolds number flows converge to a steady solution, while the high Reynolds number flows break down to unsteady flows. Integral quantities, such as friction factor and Stanton number are determined by time-averaging a sequence of solutions.

3.3   Computational Grid and Convergence Criteria

The computational grid of the flow domain consists of boundary layer grids in the near wall region of the flow, and an unstructured grid in the computational zones far from the walls. The boundary layer grids are needed to resolve the flow physics in the near wall region. The grid resolution in the outer part of the flow does not need to be as fine as in the near wall region. The total number of node points needed in the simulations is different in each simulation. In all simulations, the flow fields are resolved in time, and the laminar flow fields converge to a steady flow. One computational grid is used to resolve the laminar flow field at a specific Reynolds number. Thereafter, the computational grid is refined, and the simulations are redone. The friction factor is calculated from the simulated results. If the friction factor is not changing more than 1 % in the two computational grids, the simulated results are determined to be grid

converged. Laminar simulations typically require 50k sub-volumes for convergence while the turbulent flow simulations have required 80k sub-volumes.

With the LES simulations, boundary layer grids are used on all the wall/fluid boundaries to resolve the near wall flow region of the unsteady flow fields. The boundary layer grids are employed to ensure that the first computational grid point is located at a distance of $s^+ \leq 1$ from the wall. This is the resolution that is required to resolve the important near wall region. The simulated data is averaged over time to determine the mean velocity profiles, velocity fluctuations, friction factor, and Stanton number.

3.4   Numerical Methods

The governing equations for an incompressible, constant property (no body forces) flow are the continuity equation, the Navier-Stokes equations, and the energy equation. Written in Cartesian coordinates, the equations are:

$$\frac{\partial u_i}{\partial x_i} = 0 \tag{3.4}$$

$$\frac{\partial u_i}{\partial t} + u_j \frac{\partial u_i}{\partial x_j} = -\frac{1}{\rho}\frac{\partial p}{\partial x_i} + v\frac{\partial^2 u_i}{\partial x_j^2} \tag{3.5}$$

and

$$\frac{\partial T}{\partial t} + u_j \frac{\partial T}{\partial x_j} = \frac{k}{\rho c}\frac{\partial^2 T}{\partial x_j^2} \tag{3.6}$$

Laminar Flows The time-resolved equations are solved from some initial state to the final steady flow state.

Turbulent Flows In LES, the governing equations are filtered in space. The filtering procedure is applied to every flow field variable according to:

$$\bar{u}_i = \int_{-\infty}^{\infty} G(x, x', \Delta) u_i(x', t) dx', \tag{3.7}$$

where G is the filter function and Δ the filter width. The filtering of the variables can be applied either implicitly or explicitly. The most commonly used filtering procedure is the implicit one, where the computational grid and the discretization operators are considered as the filtering of

the governing equations. In the explicit procedure, an explicit expression of the filter function is used. In this investigation, the implicit filtering procedure is applied. The filtered governing equations can be written as

$$\frac{\partial \bar{u}_i}{\partial x_i} = 0 \tag{3.8}$$

$$\frac{\partial \bar{u}_i}{\partial t} + \bar{u}_j \frac{\partial \bar{u}_i}{\partial x_j} = -\frac{1}{\rho}\frac{\partial \bar{p}}{\partial x_i} + v\frac{\partial^2 \bar{u}_i}{\partial x_j^2} - \frac{\partial \tau_{ij}}{\partial x_j} \tag{3.9}$$

and

$$\frac{\partial \bar{T}}{\partial t} + \bar{u}_j \frac{\partial \bar{T}}{\partial x_j} = \frac{k}{\rho c}\frac{\partial^2 \bar{T}}{\partial x_j^2} - \frac{\partial \sigma_{ij}}{\partial x_j} \tag{3.10}$$

where the turbulent stresses are defined as $\tau_{ij} = \overline{u_i u_j} - \bar{u}_i \bar{u}_j$ in the momentum equation and the energy transport tensor in the energy equation is $\sigma_{ij} = \overline{u_j T} - \bar{u}_j \bar{T}$. The filtered N-S equations and energy equations are not closed due to the non-linear terms that need to be modeled; i.e. $\overline{u_i u_j}$ in the momentum equation and $\overline{u_j T}$ in the energy equation.

Subgrid-Scale Model The aim of subgrid-scale modeling is to accurately capture the influence from the small unresolved scales on the resolved ones by using the resolved flow field quantities. Several SGS models have been proposed in the literature, but the eddy viscosity model proposed by Smagorinsky [1963] is the most commonly used. The Smagorinsky model (SM) is

$$\tau_{ij} = -2v_t \bar{S}_{ij} = -2(C_s \Delta)^2 |\bar{S}| \bar{S}_{ij} = -2(C_s \Delta)^2 (2\bar{S}_{kl}\bar{S}_{kl})^{1/2} \bar{S}_{ij} \tag{3.11}$$

where v_t is the turbulent eddy viscosity, C_s is the Smagorinsky constant, and S_{ij} the strain rate tensor. The SM is purely a dissipative model that is easy to implement and has shown to perform reasonably well in a variety of flows. However, the model is not universal and the model coefficient (C_s) used needs to be changed for different flow fields. Germano et al. [1991] propose a dynamic procedure to recalculate the model coefficient during the simulation to depend upon local flow field characteristics. In the dynamic procedure, the model parameter, or actually the product ($C_s\Delta$), is recalculated during the entire simulation. The advantage of including the length-scale Δ in the dynamic procedure is to avoid the ambiguity associated with determining

the appropriate length-scale especially when using an unstructured computational grid. In the dynamic procedure, a test filter function is used that has a larger filter width than the filter function applied to the governing equations. In computations that applies unstructured computational grids, a volume average is usually applied as the test filter function. In the simulations presented in this paper, a volume average of the flow variables is used, and also the model coefficient is volume averaged before it is applied. The least-square method suggested by Lilly [1992] is used to determine one model parameter from the six independent equations. The minimum viscosity in the simulations is limited to zero and therefore, the smallest value the eddy viscosity can attain is $-\nu$.

3.5 Computational Code

Fluent (version 6.1.xx) is used in the current simulations. The flow solver is based upon finite volume collocated second-order spatial discretization. In the simulations presented here, second-order central differencing has been used for the convective terms. The SIMPLEC algorithm is used to enforce the coupling between the velocity and pressure field and to impose the divergence-free condition. A dual time stepping technique is employed to advance the simulation in time. The dual technique consists of an outer and an inner loop, where the outer loop is based upon three-level second-order time advancement, while the inner iteration uses an algebraic solver with a Gauss-Seidel smoother. Ten inner iterations are used for each time step. The time advancement is continued until time averaged mean flow quantities are obtained that no longer change.

3.6 Geometry I: Isotropic Box Lattice, Circular Cross Section Filaments

The lattice consists of equal diameter and pitch, circular cross section filaments ($\overline{P}_x = \overline{P}_y = \overline{P}_z$). Setting the pitch-to-diameter ratio, $\overline{P} = 1.55$ gives a lattice with porosity, $\varepsilon = 0.4$ and $\beta D = 1.664$ and Ke = 0.446. For these calculations, D = 2 mm. While the simulations deal with a specific diameter and pitch, the results scale with the geometry and are valid for all isotropic circular cross section filament box lattice structures with a porosity of $\varepsilon = 0.4$ and $\beta d = 1.66$.

A 40% porosity is typical of a packed bed of spheres, so results obtained here can be compared to correlations available in the literature. Furthermore, a screen lamination can be configured to have a porosity of 40%, allowing us to compare the present result to the work of Park et al. [2002].

Solutions have been obtained for Re = 5, 15, 50, 150, 440 and 1500. The flow is steady (laminar) for Re ≤ 150. Unsteady flow solutions are obtained for Re = 440 and 1500. This is consistent with the findings of Dybbs and Edwards [1984], who investigated flow in a packed bed of spheres. They found that flow characteristics could be divided into four regimes: creeping flow, Re < 1; laminar flow, 1 < Re < 150; unsteady laminar flow, 150 < Re < 300; and, turbulent flow, Re > 350.

Normalized stream wise velocity contours (u/V) for Re = 150 are shown in Fig. 3.3 at two different cross-sections of the flow domain. The figure is typical for flows with Re ≤ 150. The cross-sections are centered in the flow domain. The flow is in the positive x-direction. In the left portion of the figure, the inlet is on the left side of the domain and the outlet is at the right side. The flow is steady and laminar.

Fig. 3.3 Stream wise velocity contours for Re = 150.
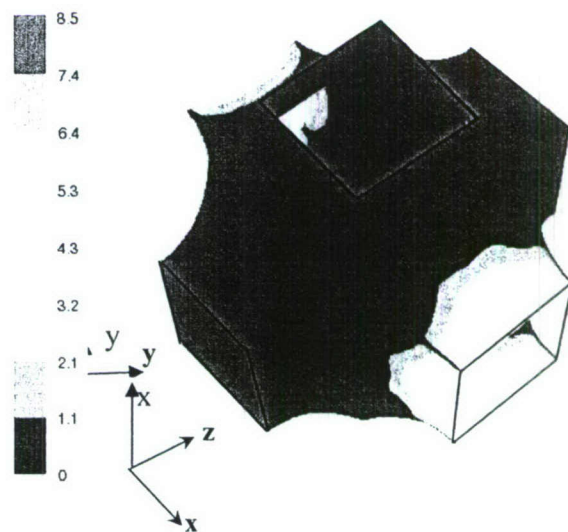
Fig. 3.4 Wall shear stress contours [Pa] at Reynolds number, Re = 150.

The figure shows a jet-like flow field through the domain, with the centerline stream wise velocity approximately 5 times larger than the pore-average velocity. The flow area outside of the jet is essentially stagnant, with slow recirculation. The jet expands as the cross-sectional flow area increases, and then contracts as it impinges on the down stream filament. The right portion of the figure shows a cross-section of the jet. This figure shows that the jet has a diamond shape cross section. Figure 3.4 shows surface shear stress contours (units = Pa). Jet impingement on the down stream filament surfaces accounts for the majority of the frictional component of the pressure drop across the cell.
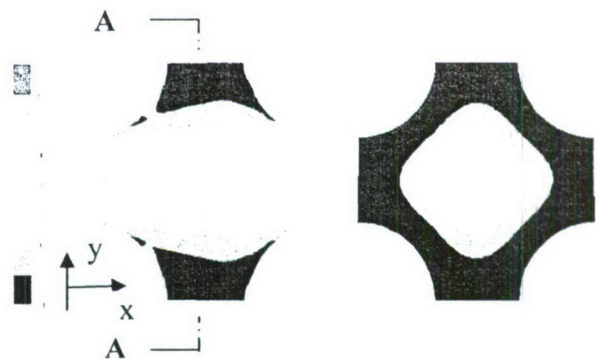
Figure 3.5 shows temperature contours (θ) at the same two locations as the velocity contours in Fig. 3.3. The jet like character is visible also for the temperature field. The recirculation zones encompassing the jet are essentially at the filament temperature. A thin thermal boundary layer coincides with the regions of high shear stress; and, Fig. 3.6 shows that regions of high heat flux are coincident with these high shear stress regions.

The unsteady simulations (Re = 440 and Re = 1500) show the same qualitative flow and thermal behavior in mean flow quantities as the laminar steady simulations do. However, Figure 3.7 (Re = 1500) shows that the central jet has broadened, with maximum centerline velocity only about 3 times V. The instantaneous picture of the flow, Fig. 3.8, shows a range of length-scales present in the unsteady jet, with considerably more interaction with the encompassing stagnant region.

The mean velocity profiles of the stream-wise velocity and velocity fluctuations for the two unsteady flows are shown in Fig. 3.9. The mean velocity profiles are plotted as a function of the distance from the center-point of the flow domain for different Reynolds number simulations. The velocity profiles are
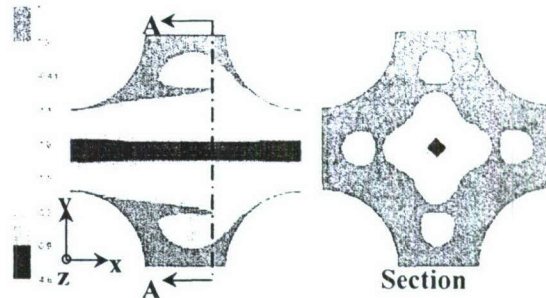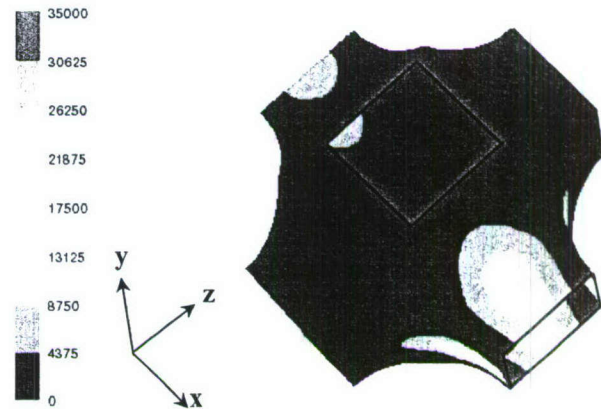

Fig. 3.5 Temperature contours (θ), Re = 150

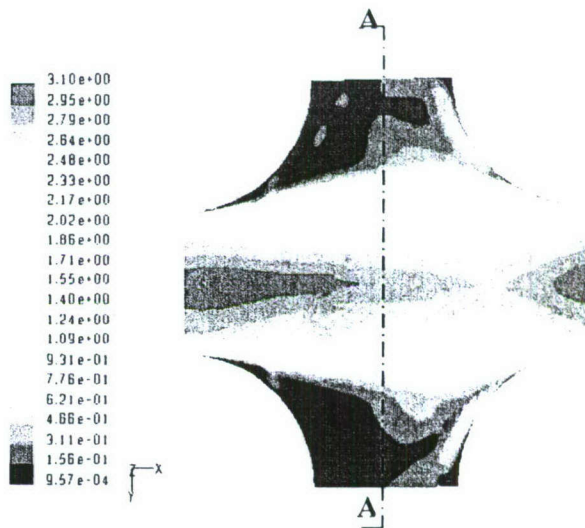Fig. 3.6 Contours of surface heat transfer coefficient (W/m^{2}K).

Fig. 3.7 Time-averaged stream wise velocity contours, Re = 1500

obtained along line AA shown in Fig. 3.7. The center of the jet is the reference location (zero location) in Fig. 3.9 and the velocity profiles are plotted in the y-direction (transverse direction). The results are all normalized with the average pore velocity (V).

Fig. 3.8 Instantaneous stream wise velocity contours, Re = 1500.

The results from the Re = 440 flow falls into the unsteady laminar regime proposed by Dybbs and Edwards [1984]. This seems to be a likely classification of the present flow field. The flow field is clearly unsteady and large unsteady structures are observed in the flow. A RANS simulation was performed (Spalart-Almares one-equation model used) of the flow field to determine the ratio between the turbulent viscosity and the molecular viscosity. This viscosity ratio can then be used to determine if the flow field is turbulent or not. The maximum ratio came out to be 5, which

Fig. 3.9 Mean velocity and velocity fluctuations as a function of Reynolds number for unsteady flows.

indicates that the flow field is not turbulent. On the other hand, the Re = 1500 flow is most likely a turbulent flow field, but not fully developed. The same RANS simulation was performed for Re = 1500 and the maximum ratio between the turbulent and molecular viscosities are 25. This ratio is higher than for Re = 440 but it indicates that the flow field is not fully turbulent. However, the dynamic Smagorinsky model is used only in the LES calculations of Re = 1500, and not in the calculations of the unsteady flow of Re = 440. The mean velocity profile is broader for the Re = 1500 than in the Re = 440 simulation. The peak value of the mean velocity profiles shows a reversed dependence upon the Reynolds number when compared to the steady laminar profiles.

The lower curves in Fig. 3.9 show the root-mean-square (rms) value of the velocity fluctuations. The fluctuations obtained in the Re = 1500 simulations have a maximum normalized value of 0.93 (normalized with the average pore velocity), which results in fluctuations of 26 % of the maximum mean velocity. These results are consistent with the findings of Yevseyev and co-
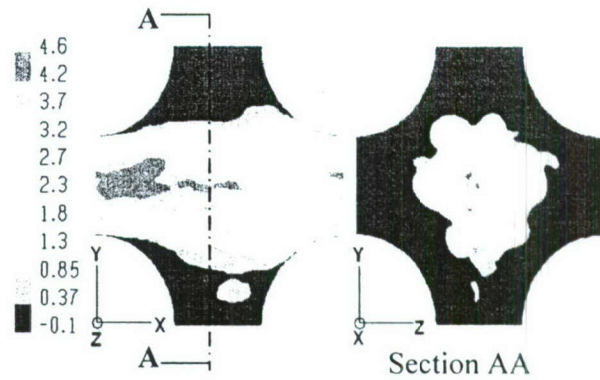
workers [1991], who observed maximum rms fluctuations of about 20 % of the mean velocity profile in a packed bed of spheres for Re = 6300. Two peaks are observed in the velocity fluctuations, where the shear stress is largest.

Fig. 3.10 shows the friction factor as a function of Reynolds number. The friction factor is calculated according to

$$f = \frac{2\Delta p D_h}{\rho V^2 P_x} \qquad (3.12)$$

where Δp is the pressure drop. The friction factor of the box lattice structure is compared to two references. The first reference is the Ergun correlation for a packed bed of spheres

Fig. 3.10 Friction factor as a function of Reynolds number. ε =0.4.

[Bird et al, 1966], and the second reference is experimental data for woven stacked screen laminates [Park et al, 2002]. The porosity of the screen laminates are ε = 0.69 and the experimental data is obtained for ten stacked screens. The experimental data is expected to include entrance and wall effects, while the simulated results do not. The Ergun correlation has been evaluated with ε = 0.4.

At low Reynolds number, the friction factor calculated from the simulated results for the box lattice structure is essentially the same as that of both the packed bed of spheres and the screen laminates. The friction factor decreases as the Reynolds number increases for the low Reynolds number laminar flow fields. As the flow fields become unsteady and/or turbulent with an increasing Reynolds number, the friction factor levels out and becomes constant. Thus, at low Reynolds number, wall shear dominates; while at high Re, inertial effects dominate. At high Reynolds number, the order in magnitude is: packed bed, highest; screen laminates, mid; box lattice, lowest. This ranking correlates with the amount of torturousity in the flow.

The Stanton number as a function of Reynolds number is shown in Fig. 3.11. In the numerical simulations, the Stanton number is based upon the temperature difference between the fluid/solid interface and the volume average flow temperature. The Stanton number for the box lattice structure is compared to two different reference cases. The first reference is an algebraic
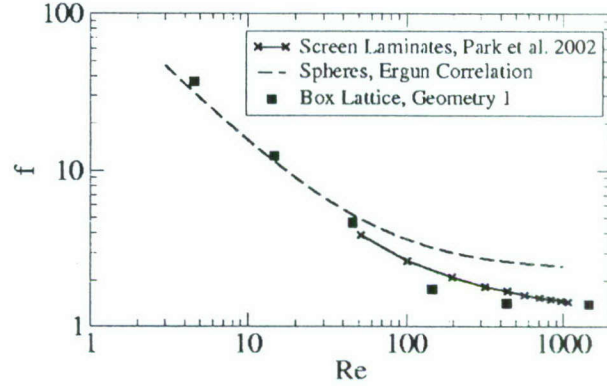
correlation function for a packed bed of spheres proposed by Wakao and Kaguei [1982]. The second reference is experimental data of screen laminates [Park et al, 2002]. The experimental data was obtained for a constant heat flux for a stack of ten screens. The Stanton number in this case is based on the superficial flow inlet temperature.
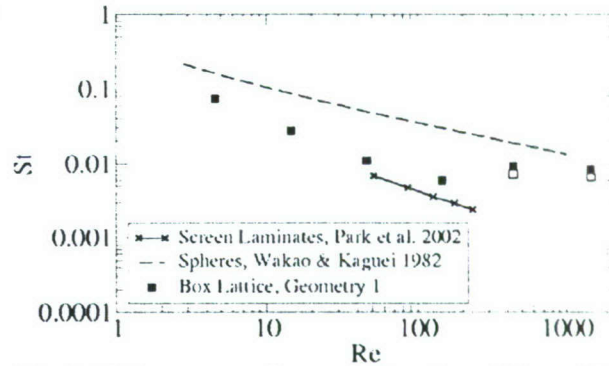

Fig. 3.11 Stanton number as a function of Reynolds number. ε =0.4.

The Stanton number results for the open lattice structure are between the results from the packed bed of spheres and the screen laminates. All correlations tend to converge with Re $\rightarrow$ 0; and, at high Reynolds number, the box lattice and packed bed results also tend to converge.

A jump in the simulated values of the Stanton number is observed as the flow field becomes unsteady (Re = 440). The data points denoted with a solid square for the unsteady flow fields in Fig. 3.11 are the result of solving the filtered governing equations (Eqs. 3.8 – 3.10) simultaneously and averaging the Stanton number over time. In the simulations, a same time step and number of inner iterations are used for solving the N-S equations and the energy equation. The data denoted by the open squares represent results from simulations where the energy equation is solved for a frozen flow field. The data calculated for several different flow fields are then averaged. These simulations result in a lower value of the Stanton number. The differences observed in the data between the two approaches are due to the time derivative of the temperature field ($\frac{\partial \overline{T}}{\partial t}$). The reason for performing the simulations of solving the energy equation separately was to determine the influence of the time term in the energy equation and to verify that the jump in the Stanton number observed for the unsteady flow fields was not due to the handling of the time term. The values of the Stanton number from solving the equations simultaneously might be slightly reduced as the time step is decreased and the number of inner iterations is increased. However, the value is expected to be somewhere in the range between the solid and open square value.

Conclusions Numerical simulations are performed of the flow and heat transport in an isotropic box lattice structure ($\varepsilon = 0.4$ and $\beta D = 1.66$) to determine the performance of the structure as a heat exchange surface. The simulations deal with a specific diameter and pitch. However, the results scale with the geometry and are valid for all isotropic circular cross section filament box lattice structures with a porosity of $\varepsilon = 0.4$ and $\beta d = 1.66$. The simulations are time resolved to capture any unsteadiness in the flow fields. The low Reynolds number flows were simulated using direct numerical simulations, while the unsteady flows were simulated using large-eddy simulations.

The mean velocity profiles and velocity fluctuations were studied in the pores of the heat exchanger. The flow and thermal fields were simulated for six different Reynolds numbers, Re = 5, 15, 50, 150, 440, and 1500. The four lowest Reynolds numbers resulted in steady laminar flow, consistent with the findings for a packed bed of spheres reported by Dybbs and Edwards [1984]. The flow fields of the two highest Reynolds numbers resulted in unsteady flows. Simulations using Reynolds-Averaged Navier-Stokes equations were used to determine if the flow fields where turbulent or unsteady laminar. The Re = 440 flow was found to most likely be an unsteady laminar flow, while the Re = 1500 flow shows tendencies to be a turbulent flow.

The flow field through the lattice structure has an intense jet flowing down the centerline of the cell encompassed by a relatively quiescent region. The steady laminar flow fields showed a peak value of the mean velocity profile that increased with an increasing Reynolds number. The two unsteady flows had jet velocity profiles that broadened with increase in Re; and, velocity fluctuations increased with increasing Reynolds number. Velocity fluctuations of 26 % of the maximum mean velocity was observed for Re = 1500.

High wall shear stress and heat flux is observed on the down-stream portions of the cell, due to jet impingement on the windward side of the down-stream filaments. The friction factor correlation is similar to that found in flow through a packed bed of spheres and flow through a lamination of plain weave screens. The Stanton number correlation is lower than that of a packed bed of spheres; and, for higher Reynolds numbers, higher than that measured for flow through a screen lamination. This may be due to the fact that the lattice structure has additional (x-axis) filaments that the screen laminate lacks. The laminar-to-turbulent flow jump in Stanton

number is presumably due to increased mixing with the warm, stagnant ring that surrounds the center-line jet flow in the cell.

3.7   Geometry II: Box Lattice With Elliptic Cross Section Filaments

High Reynolds number flows (Re > 440) have $\Delta p \propto V^2$, so box lattice-based heat exchangers should probably be operated in the laminar regime to maintain pressure drop at reasonable levels. On the other hand, the laminar jet flows depicted in Figs. 3.3 – 3.6 have the cool jet fluid shrouded by a relatively warm stagnant fluid with little interaction between the two flow regimes. Consequently, regions of high heat flux are limited to the windward side of the down-stream filaments; and, this limits performance. Adding ellipticity to lattice filaments to streamline the flow through the cell at laminar flow could reduce the friction factor while at the same time increase the surface area (increased β) leading to larger areas of high heat flux, which would give rise to an increase in the Stanton number correlation.

To study the behavior of elliptic cross section filament box lattices (Fig. 1.4), two geometries with varying aspect ratios are considered. These are stretched versions of the circular cross section filament base case considered in the previous section. The objective is to introduce increasing ellipticity to the y-axis and z-axis filaments (flow is perpendicular to these filaments) while maintaining ε and Ke_y constant. The stream wise (x-axis) filaments retain a circular cross section.

To introduce ellipticity, the base case structure is stretched along x-direction as a function of aspect ratio. But by doing so, the volume fraction is reduced by approximately 50%. And the y-axis effective thermal conductivity is expected to reduce proportionally. Therefore to hold the volume fraction and y-axis effective thermal conductivity constant, the stretched structure is then scaled to maintain a constant cross sectional area of y-filament. The two cases considered in the present study have constant volume fraction and essentially constant Ke_y .

Table 3.1 summarizes the physical attributes of the Base Case (Geometry I) and two elliptic cases (Geometry II) to be analyzed. The table shows that all three geometries have the same filament pitches ($\overline{P}_x = \overline{P}_y = \overline{P}_z = 1.55$); the stream wise filaments have circular cross sections (a_x = 1); and, they have the same porosity ($\varepsilon = 0.4$).   Geometry II, **Case A** has y-axis and z-axis filaments with 1.5-to-1 aspect ratio and a 9.5% increase in surface area relative to Geometry I. Geometry II, Case B has y-axis and z-axis filaments with 3-to-1 aspect ratio and a 41% increase

in surface area relative to Geometry I. Furthermore, all three designs have the same filament pitch and essentially the same y-component effective thermal conductivity. The final column of the table shows the solution domain for the three geometries considered.

TABLE 3 Geometric details of the base case and two elliptic cross section filament cases considered for numerical analysis. $\varepsilon = 0.4$, $\overline{P}_x = \overline{P}_y = \overline{P}_z = 1.55$, $a_x = 1$

Case	Geometry	β2r$_e$	Ke$_y$	Domain
Geometry I (Base Case)	$a_y = a_z = 1$	1.644	0.446	
Geometry II (Case A)	$a_y = a_z = 1.5$	1.80	0.42	
Geometry II (Case B)	$a_y = a_z = 3$	2.32	0.4169	

Simulations are performed with water (Pr = 7) for three laminar flows, Re = 30, 100 and 150 with the same boundary conditions, solution algorithm and convergence criteria as described in the previous section. The grid structure is similar to the one used in the Base Case study, with approximately 50k sub-volumes giving convergent solutions [Sarde, 2006].
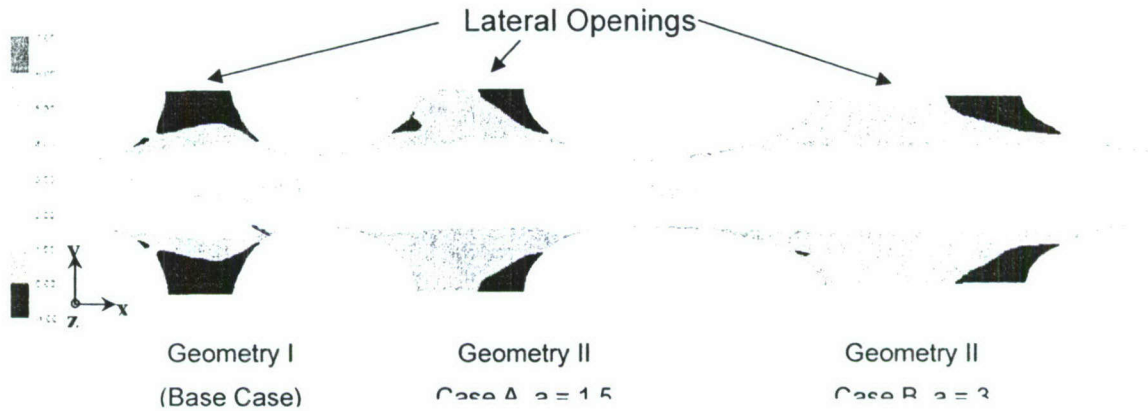
Fig. 3.12 Stream wise velocity contours at Re = 150

Figure 3.12 shows normalized stream wise velocity contours (u/V) at Re = 150 for circular cross section filament box lattices and the two cases of elliptic cross section filament box lattices. The velocity contours are normalized by the average pore velocity. The flow is in the positive x-direction. The Re = 150 example is typical of what is observed for lower Reynolds number flows [Sarde, 2006]

The figure shows that the circular cross section case (Geometry I) has more intense centerline flow than either of the elliptic cross section cases. Furthermore, the Geometry II jets disperse, leading to a reduction in centerline velocity as one proceeds downstream. The two cases of elliptic cross section filament box lattices have recirculation zones only at the down stream edges of the cell; whereas, Geometry I has recirculation zones spread in the regions above and below (and on either side of) the jet area. Geometry II, Case A exhibits some asymmetry in that the flow is skewed upwards near the flow outlet. as shown in the figure.
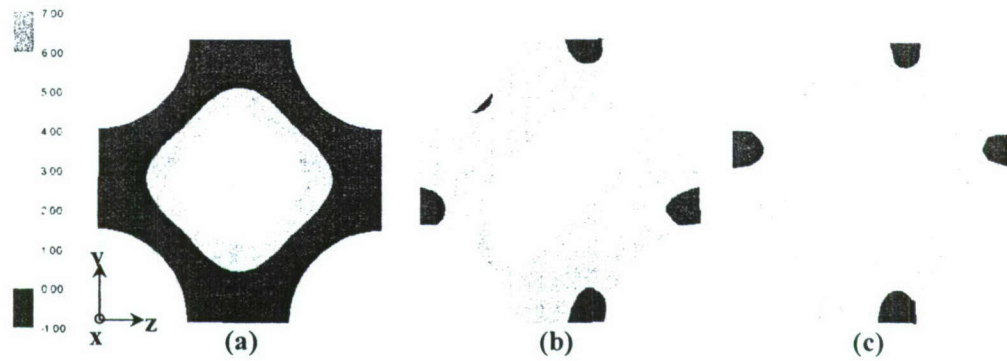
Fig. 3.13 Steam wise velocity contours at Re = 150; y-z cross section of the jet
(a) Geometry I (b) Geometry II, a = 1.5 (c) Geometry II, a = 3

Figure 3.13 shows normalized stream wise velocity contours in the y-z plane at mid-span for Geometry I and II. The figure shows that as filament aspect ratio increases, the Geometry II jet cross sections are increasingly more complex and asymmetric than Geometry I.
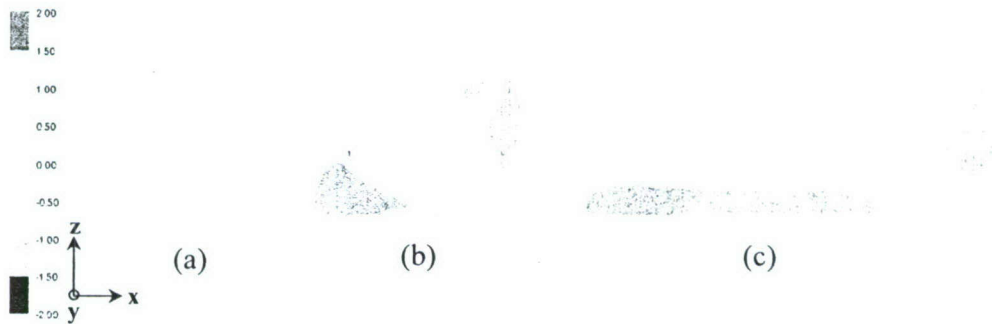
Fig. 3.14 y-velocity contours in the x-z plane lateral openings at Re = 150:
(a) Geometry I, (b) Geometry II, Case (A), (c) Geometry II Case (B)

Figures 3.12 and 3.13 illustrate that as ellipticity is introduced, the flow through the cell becomes increasingly complex. This is further illustrated in Fig. 3.14, which are y-component normalized velocity contours in the x-z lateral opening plane of the cell (note Fig. 3.12). A weak inflow/outflow exists across each Geometry I lateral opening. This intensifies when filament ellipticity is introduced so that maximum inflow/outflow velocities are greater than the pore average velocity, V.

Figure 3.15 shows the shear stress contours [units = Pa] at Re = 150 for Geometries I and II. The Figure shows that introduction of filament ellipticity does increase the area of high wall shear stress as well as increase the magnitude of the wall shear. The average shear stress of Geometry
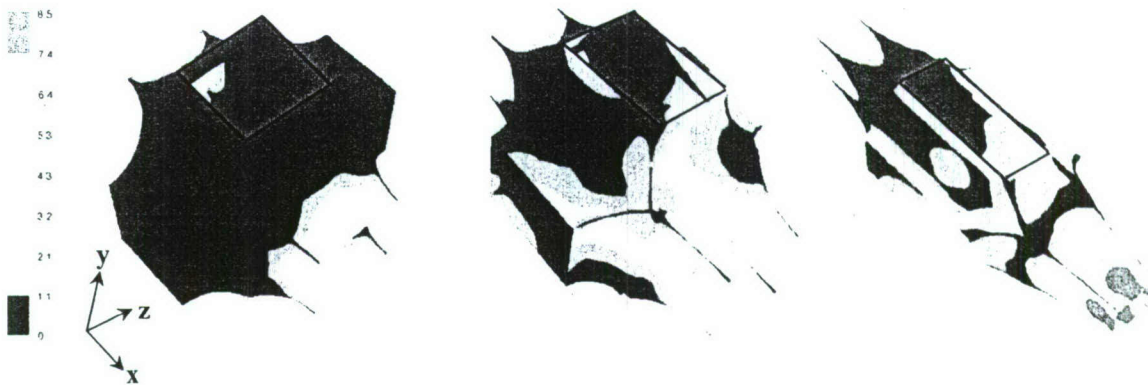
Fig. 3.15 Wall shear stress (Pa) contours, Re = 150 (a) Geometry I, (b) Geometry II Case (A), (c) Geometry II Case (B)
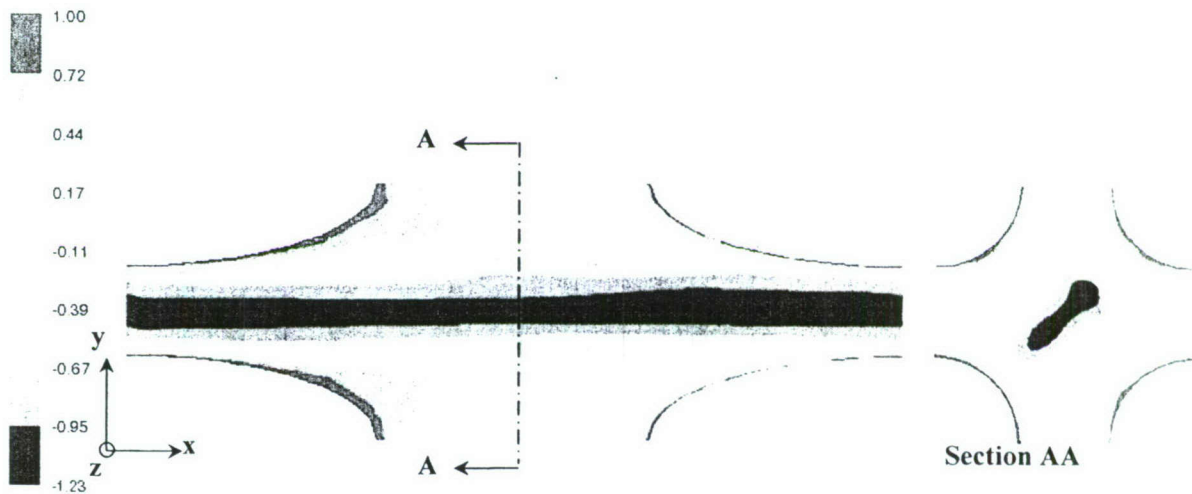
Fig. 3.16 Temperature contours (θ) for Geometry II, Case B at Re = 150.

II Case A is 63% higher than that of Geometry I; and, Case B average wall shear stress is in turn 32% higher than that of Case A.

Figure 3.16 shows non-dimensional temperature contours (θ) at Re = 150 for Geometry II, Case B. The Figure is typical of what is observed for Case A and lower Reynolds numbers [Sarde, 2006]. The figure shows that separation of the jet-flow is delayed and a thermal boundary layer now exists along the leeward surface of the up-stream filaments, as well as on the windward surface of the down-stream filaments. Furthermore, in comparison to Fig. 3.5, the recirculation zones that encompass the cool jet flow are now at a lower temperature. This leads to an increase in the area of high heat flux, as well as the magnitude of the heat flux, as shown in Fig. 3.17.

Geometry I
Base Case

Geometry II
Case B, a = 3
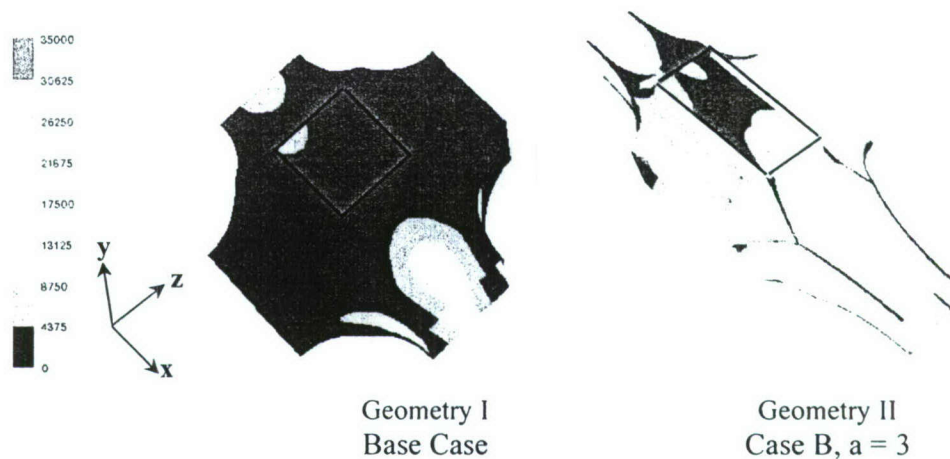
Fig. 3.17 Contours of surface heat transfer coefficient (W/m²K) for at Re = 150: Geometry I and Geometry II, Case B.

Figure 3.18 compares the friction factor correlation of Geometries I and II. Apparently, for the cases considered, streamlining y-axis and z-axis filaments leads to and increase in f. This is probably due to the increase surface area of the elliptic cross section filament unit cell coupled with the fact that the jet flow through the cell remains attached over a larger fraction of the unit cell surface (Fig. 3.15). Geometry II, Case a and B have essentially the same friction factor
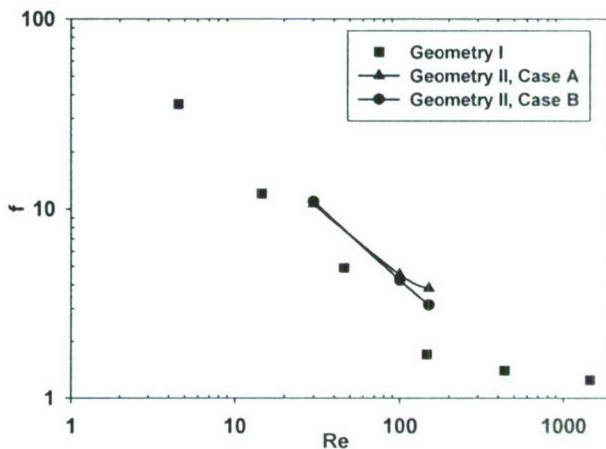
Figure 3.18 Friction factor correlations, box lattices.

correlation when Re ≤ 100. The less streamlined case (Case A) has a higher friction factor correlation when Re > 100.

Figure 3.19 compares the Stanton number correlations of Geometries I and II. Since the flows considered are periodically fully developed, an increase in friction factor should lead to an increase in Stanton number, as shown in the figure. The Geometry II, Case B Stanton number correlation is approximately 2-flod higher than the Geometry I correlation.

Conclusions Numerical simulations are performed to evaluate the effect of filament ellipticity on flow and heat transport in box lattices. Two cases considered have elliptic cross section filaments

which are perpendicular to the flow (y-axis and z-axis) and a circular cross section filament with axis parallel to the flow (x-axis): Case A, $a_y = a_z = 1.5$; Case B, $a_y = a_z = 3$. The flows evaluated are laminar in that all the Reynolds numbers considered (Re = 30, 100, 150) resulted in steady flow fields. The flows through the matrices exhibited jet like behavior. Introduction of filament ellipticity resulted in an increase in surface shear

Figure 3.19 Stanton number correlations, box lattices

stress and heat flux. Consequently, elliptic cross section filament box lattices have higher friction factor and Stanton number correlations. Introduction of filament ellipticity also resulted in an increase in intensity of secondary flows within the matrix.

4. Flow Boiling of FC-72 from a Screen Laminate Extended Surface Matrix

An investigation is conducted to assess the thermal performance of multi-layered screen laminates when used as extended surface matrices (ESM's) in vertical up-flow boiling. A dielectric coolant (FC-72) is used as the working fluid. Four specimens are constructed having different mesh-geometries and/or number of layers. Channel Reynolds numbers are varied from 2700 to 8500 and surface temperatures are varied from 50 °C to 100 °C.

Results indicate that devices equipped with this technology can tolerate steady heat fluxes up to 140 W/cm^2 (based on the base area of the ESM) with corresponding surface temperatures below 100°C. Reyn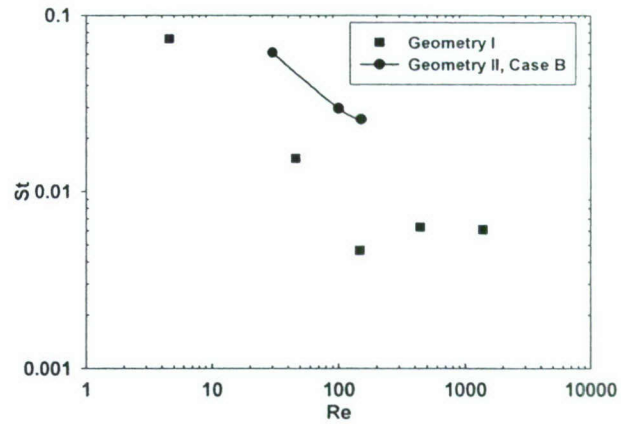olds number has a small effect on performance at low surface temperatures and a moderate effect at higher surface temperatures. Total capacity of the ESM (the product of heat flux and base area) increases approximately linearly with the thickness. A feature of this technology is that it greatly extends the working range over a bare surface.

Dhir [1994] reviews much of the work that relates to boiling in porous media. The presence of a porous media adjacent to a heated surface affects the ebullition process since particles in contact with the surface may introduce nucleation sites. These particles may also increase the effective surface area of the heat transfer surface (fin effect), and stimulate secondary flows due to spatial variations in capillary pressure. Dry-out phenomena (vapor channels) becomes a complicated process, where particle size is the important length scale.

A number of studies [for example Vasil'Yev, 1992; Brautsch and Kew, 2002] investigated boiling on surfaces that have a wire mesh <u>overlaying</u> a heat transfer surface. For some reason, the mesh is pressed against the surface, but not bonded to the surface. Brautsch and Kew [2002] studied pool boiling performance from smooth and roughened aluminum surfaces tested with and without plain weave stainless steel screens clamped to the surface. Distilled water at 1 atm. was used as the working fluid. Mesh numbers of 50, 100, 150, and 200 were tested. The number of layers was varied as one, three, or five. Results showed performance enhancement on the smooth surface increased with Mesh number up to ~12 °C; and, a single layer was always most effective. At superheats greater than this the finer meshes inhibited vapor removal and the

courser meshes performed better. At superheats below ~10 °C the presence of a mesh resulted in an increase of nucleation site density.

Gerlach and Joshi [2005] studied pool boiling performance on single-layer copper and bronze plain weave meshes soldered to a copper substrate. The working fluid was a Fluorinert, PF5060. These meshes were investigated as a cost effective alternative to micro grooved surfaces which are made by etching or machining. Mesh numbers of 20, 50, and 150 in^{-1} were investigated with and without a glass plate placed over the mesh. The results for the confined and unconfined meshes (heat flux vs. superheat) were compared to fabricated samples investigated previously by the authors. The 50-mesh showed the best performance followed by the 150 and 20-meshes. All fell short of the fabricated samples. The confined meshes performed poorer than the unconfined meshes. The 20 and 50-meshes showed an increase in CHF versus the 150-mesh or bare surfaces. No hysteresis was observed in the boiling curves. The thermal resistance of the confined meshes was compared to a solid copper heat spreader. The meshes all showed higher thermal resistance versus an equivalent solid copper spreader.

Li and Peterson [2005] showed, in the context of heat pipe performance, that an Md = 1509 in^{-1} x 0.0022 in. fine-filament plain-weave bonded to a plain horizontal surface resulted in a *5-fold to 20-fold increase in water evaporation rates*. These experiments were with "thin" layers of water over the mesh, so bubble formation was inhibited. Enhanced evaporation rates were presumably due to the highly convoluted nature of the surface coupled with the large specific surface area of the mesh.

We have found no work in the open literature reporting flow boiling performance of porous extended surfaces (fins). However, Nakayama et al. [1984] studied saturated pool boiling at atmospheric pressure in FC-72 from a cylindrical copper stud attached to a heat source. The stud was covered with either microfins or multi-layered porous structures. The highest performance was achieved from a stud having microfins on the side surfaces and porous plates on the tip. Critical heat flux in that case was 33 W/cm^2 (based on the projected area of the stud, $\pi \cdot r^2$). Heat fluxes were 1.9-10 times higher than those of a smooth stud at the same superheat.

Rainey and You [2000] studied saturated pool boiling from a 1 cm x 1 cm simulated chip at atmospheric pressure in FC-72 using "doubly enhanced" surfaces. The enhancement methods investigated were square pin fins (1 mm x 1 mm) with lengths ranging from 0 to 8 mm tested

with and without the microporous coatings studied by Chang and You [1997]. The highest CHF was achieved using 8 mm long fins with a microporous coating. Critical heat flux in that case was 129.4 W/cm^2 (based on the projected area of the simulated chip).

4.1 Experimental Setup and Procedure

For this work, copper filament plain weaves with $M_x = M_y = M$ and $D_x = D_y = D$ are used. Relevant properties for the prototype screen laminates are given in Table 4.1.

Table 4.1: Properties of prototype plain-weave screen laminate ESM's.

Mesh number, M (cm^{-1}/in^{-1})	Wire diameter, d (mm/in)	Number of layers, N	Surface coating	Compression factor, cf	Porosity, ε	Effective conductivity, ke (W/m/K)	Specific surface area, β (m^2/m^3)	Pore hydraulic dia., D_h (mm)
7.9/20	0.41/0.016	5	Nickel plating over solder	0.96	0.72	50	2700	1.05
		10		0.91	0.71	52	2900	0.98
19.7/50	0.23/0.009	5	Nickel plating	1.10	0.63	60	6500	0.39
		10		0.92	0.61	69	7500	0.30

The table shows the two mesh numbers that were investigated (20 in^{-1} and 50 in^{-1}), wire diameters (0.016 in and 0.009 in), number of layers (five and ten), surface coatings (described in the next section), compression factor cf, porosity ε, effective conductivity ke, specific surface area β, and the pore hydraulic diameter D_h. The naming convention that will be used in this chapter to identify the laminates is: mesh number (in^{-1})/wire diameter (in)/number of layers. For example, M20/D016/N5 represents the 20-mesh, 0.016 inch diameter wire, five layer mesh[4].

The compression factor, cf is defined as:

$$D_h = \frac{4 \cdot \varepsilon}{\beta} \tag{4.1}$$

where t is the thickness of the laminate, N is the number of layers, and d is the wire diameter. The compression factor accounts for wire crimping at intersections and interleaving of wire filaments in the lamination. The smaller the value of cf the tighter the laminate is packed together. Values of porosity, specific surface area and in-plane effective thermal conductivity are calculated using the expressions developed by Xu and Wirtz [2002].

---

[4] In the United States, weave dimensions are expressed in British Gravitational Units (inches).

Test Geometry Implementation of the screen laminate ESM is as shown in Fig. 4.1. Fluid approaches the laminate at superficial temperature and velocity, T_{in}, V_{in}, respectively and pressure P_{in} after passing through a flow straightener (not shown). An amount of heat q enters the base of the laminate from a calorimeter that is buried in the channel wall. For this work, $w = 5.08$ cm, $H = 0.95$ cm, and t (the laminate thickness) varies by laminate. The inlet temperature, T_{in} is measured using

Figure 4.1: Implementation of screen laminate ESM.

an exposed-junction T-type thermocouple approximately 4 cm below the laminate. The inlet velocity, V_{in} (really volume flow rate) is measured ahead of the test section using $0.2 - 1$ gpm and $1 - 10$ gpm flow meters. The inlet pressure, P_{in} is measured downstream of the flow straightener, 4 cm below the laminate using a $0 - 15$ psia pressure transducer.

ESM Construction/Implementation The 20-mesh laminates were reflow soldered using 95/5 Tin/Antimony solder paste ($k_s = 67$ W/m/K). Soldering ensures that wire intersections are in good thermal contact and the individual layers are in good thermal contact with each other. The lamination was then reflow soldered to the end of the calorimeter using 95/5 Tin/Antimony solder. The interfacial resistance between the calorimeter and laminate is assumed to be small enough to neglect when calculating superheat. We feel this assumption is valid because care was taken to ensure the bonding surfaces were flat prior to soldering, i.e. the thickness of the solder joint is very thin.

Reflow soldering the 50-mesh laminates is not feasible because liquid solder will clog the much smaller pores. Therefore, the individual layers of the 50-mesh laminates are nickel plated to bond the wire intersections; stacked together using small wires to align the pores; clamped together then reflow soldered to the calorimeter using 95/5 Tin/Antimony solder paste.

All laminates are given a superficial coating of bright nickel after bonding to the calorimeter to ensure similar surface characteristics. A brief outline of the plating process is given in [Holland, 2006]. Finally, all laminates are arranged such that the pores of the individual layers are aligned

(within practical limits). This "inline" arrangement gives the fluid a straight path through the laminate.

Figure 4.2 shows the implementation of the ESM/calorimeter in the flow channel. The screen laminate spans the H x w channel. The unheated (left) wall is a transparent polycarbonate plate to allow the flow to be visually monitored and photographed. The right and lateral walls are of Teflon. A "fin" calorimeter projects through the right wall. Cartridge heaters placed in a copper block at the fin base provide the heat load. The

Figure 4.2: Implementation of calorimeter

temperature gradient along the fin is measured at two axial locations, T_1 and T_2 a distance Δy apart. For this study $L = 2.88$ cm, and $\Delta y = 1$ cm. Each temperature T_1 and T_2 is measured twice: once from the left side of the calorimeter and once from the right side of the calorimeter then averaged. The temperatures are measured using sheathed, ungrounded T-type thermocouples at a depth of 0.64 cm in from the sides. With heat losses from the fin sides, a model shows that the temperature variation along the fin length is parabolic. Heat losses from the calorimeter fin is accounted for in the data reduction algorithm. Given T_1 and T_2, the fin tip temperature (equal to the ESM base temperature) and ESM base heat flux are calculated [Holland, 2006].

In this study the laminates are tested over the mesh Reynolds number, Re range of 103-772. The Reynolds number based on the superficial velocity and hydraulic diameter of the test section is denoted Re_{ch} and ranges from 2750-

Figure 4.3: Schematic of hydraulic loop

8560. A schematic of the hydraulic loop is shown in Fig. 4.3; and, Fig. 4.4 is a photograph of the test rig. The system is filled through the reservoir. A sight tube on the side of the reservoir allows the fluid level to be visually monitored. A magnetically-coupled March® 6 Series pump (PC) pumps the FC-72 through a small inline 40 micron filter (FLT). The fluid then passes through two Omega® flow meters (FM) of unequal capacity connected in parallel. This arrangement (high-flow/low-flow) allows for measurements ranging from 0.2 – 12 gpm. Flow rate is controlled by throttling valves

(1) reservoir	(6) test section
(2) pump	(7) heat exchanger
(3) flow meters	(8) borescope/lighting
(4) electric heaters	(9) digital camera
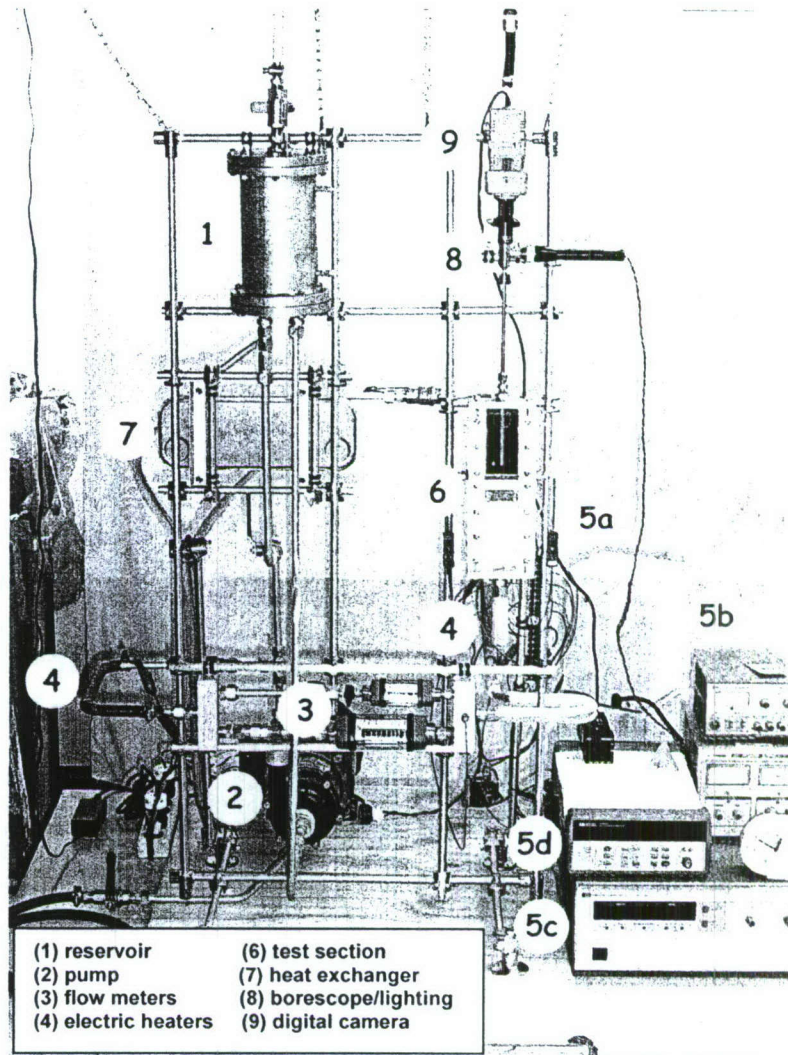
Figure 4.4: Flow boiling test rig

just upstream of the flow meters. After passing through the flow meters the fluid is heated to the desired inlet temperature ($T_{in} = T_{sat} - 10°C$) using Omega®/Minco® electric tape heaters connected to variable AC power supplies (5a in Fig. 4.3). Inlet temperature is controlled by varying the voltage to the tape heaters. The test pressure, P_{in}, is measured at the same location with an Omega® 0 – 15 psia absolute pressure transducer (5b in Fig. 4.4). Pressure is controlled by throttling the valve downstream of the test section. Two 500 W Omega® cartridge heaters, connected to a 1000 W Hewlett-Packard® power supply (5c in Fig. 4.4), are placed in the copper block and provide the heat load. Raw data (temperatures and pressure) is collected with a Hewlett-Packard® data logger and an Omega® process controller (5d in Fig. 4.4). After exiting the test section a two-fluid parallel plate heat exchanger (HE in Fig. 4.3), connected to an

external chiller, is used to remove the heat generated in the test section and keep the total system pressure constant by condensing the vapor generated in the test section. A self-illuminating borescope (8 in Fig. 4.4) is connected to a Kodak® digital video camera (9 in Fig. 4.4) to photograph the boiling from above the laminate. A Nikon D12 digital SLR camera views the process from the side.

Test Procedure - Prior to collecting data the FC-72 is boiled vigorously in the heated length for approximately 90 minutes to degas it. During this time a vent on top of the reservoir is periodically opened to allow the separated gasses to escape. The effect of dissolved gasses on boiling in FC-72 has been documented by Rainey et al. [2003]. These gasses tend to shift the boiling curve and removing them ahead of time allows better repeatability in the experiment. No effort is made to analyze the exact gas content in the FC-72. However, this procedure is consistent with procedures reported by Chang and You [1997] and Mukherjee and Mudawar [2003].

For each experiment, data is collected by varying the heat flux from high to low. This is referred to as the cooling curve [Incropera and DeWitt, 2002] and explains why there is no incipience overshoot evident in results discussed later on. Each data point is collected after the operating conditions stabilize to within a specified tolerance and the time variation of T_l is less than 0.04 °C/min or a repeating oscillation is observed.

4.2 Data Reduction and Error Analysis

The ninety-five percent confidence intervals for all relevant measurements are given in Table 4.2. These confidence intervals are based on the observed fluctuations about the average for measured quantities (temperature, pressure, linear measurments, etc.) or reasonable estimates for values taken from reference handbooks (material properties). FC-72 properties are evaluated at the inlet temperature. This information is used in a Monte Carlo data reduction/error propagation

Table 4.2: 95% Confidence-level error tolerances

Measured Quantity	2-σ Error
wire diameter, d	± 0.001 in.
mesh number, M	± 10%
linear measurments	± 0.005 in.
material properties	± 5%
fluid properties	exact
flowrate	± 0.05 gpm
calorimeter temperatures, T_1 and T_2	spread in left to right readings + 1 °C
inlet temperature, T_{in}	± 0.5 °C
inlet pressure, P_{in}	± 0.15 psi

computer code that calculates the superheat, heat flux (based on base area of the laminate, $w \cdot t$), heat transfer rate (heat flux times base area), mesh Reynolds number, and the ninety-five percent confidence intervals in each result. Error propagation analysis gives the range of absolute errors in calculated results shown in Table 4.3 [Holland, 2006]. Minimum values correspond to the lowest heat fluxes; and, maximum values correspond to the highest heat fluxes.

Table 4.3: Absolute errors in calculated quantities

Calculated Quantity	2-σ Error
ΔT_{sat}	0.6 - 2.5 °C
q"	1.5 - 11 W/cm^2
q	2.4 - 30 W
Re	10 - 33
Re$_{ch}$	289 - 360
q"loss/q"·100	0 - 3%

4.3 Results
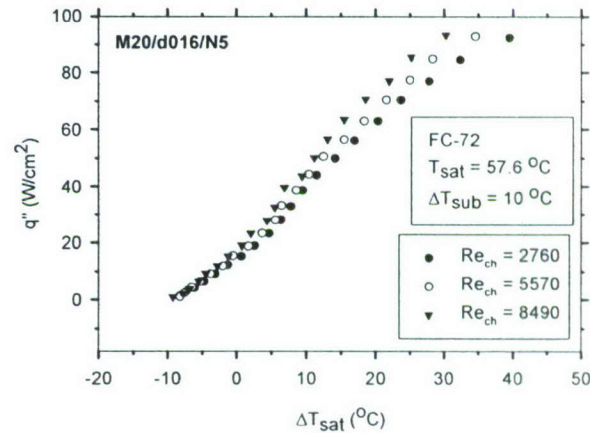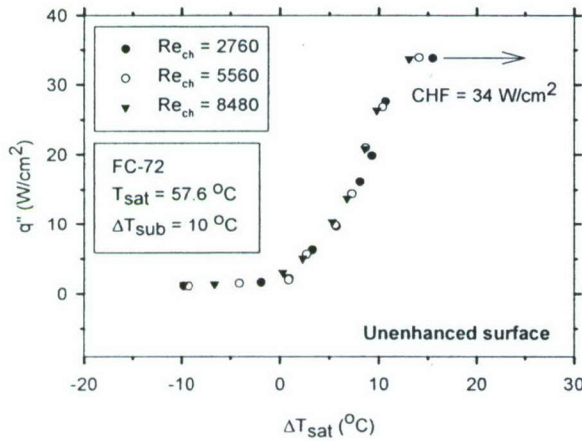
Fig. 4.5: Surface Heat Flux vs. superheat, un-enhanced surface.

Fig. 4.6: ESM base heat flux vs. superheat, M20/d016/N5 laminate.

Figure 4.5 plots the cooling curve of a 50.8 mm wide x 2.0 mm tall (1 cm^2) un-enhanced Ni-plated copper surface (no ESM) for three channel Reynolds numbers. The surface is the tip of the calorimeter, and its' length in the stream wise direction is approximately the thickness of ESM prototypes. The Figure shows no Reynolds number effect for this very short surface. The critical heat flux (CHF) for the reference surface is approximately 34 W/cm^2 at a superheat of approximately 14 °C. Experimentally, the CHF is taken as the highest heat flux achieved prior to observing a large increase in surface temperature for a modest increase in heat flux.

Fig. 4.6 plots the ESM base heat flux vs. superheat (cooling curve) of ESM M20/D016/N5 for the same three channel Reynolds numbers as Fig. 4.5. The Figure is typical of what is observed with the three other ESM prototypes. Cooling curves for the other three prototypes are found in

[Holland, 2006]. The effect of increasing Reynolds number is an upward shift in the curves. This effect is negligible in the single phase regime (negative superheats) and becomes more pronounced as superheat increases. The heat flux increases with increasing superheat throughout the entire range of testing, i.e. no evidence of burnout conditions observed for superheats in excess of 35 °C, where an ESM base heat flux of 95 W/cm^2 is achieved. This is in marked contrast to the un-enhanced surface which showed burnout at superheat temperatures of approximately 14 °C. The effect of increasing Reynolds number is an upward shift in the curves. This effect is negligible in the single phase regime (negative superheats) and becomes more pronounced as superheat increases.

The mechanism for this tolerance to superheats beyond 13-15 °C is likely due to the high effective thermal conductivity of the laminate. It is proposed that when unstable nucleate boiling (transitional) or film boiling occurs at the base of the laminate, the copper filaments are still capable of pumping heat to areas of the laminate further from the heated wall and boiling simply occurs from a larger fraction of the exposed area of the laminate. The burnout condition would presumably be reached when boiling occurs from the entire surface exposed to the flow.

Figure 4.7 shows schematically what is being proposed. When ΔT_{sat} exceeds 13-15 °C transitional/film boiling occurs near the base of the screen laminate. As one moves away from the heated wall the local temperature in the laminate decreases. At some location the temperature will fall below 13-15 °C and nucleate boiling will occur instead. As one moves further from the heated wall the local temperature will fall below T_{sat} and single phase heat transfer will then occur.

Figure 4.8 shows the M50/d009/N10 screen laminate at three key superheats. The left-hand images were taken by photographing the

Fig. 4.7: Proposed modes of boiling heat transfer.

laminate from the side through the polycarbonate cover. The y = H edge of the lamination is visible across the lower portion of the edge views. The white band immediately above the ESM edge is a sealant (about 2 mm thick) located on the far wall (y = 0), and the black background above this is the black Teflon y = 0 wall. The right-hand images are plan views that were taken by photographing the laminate from above using the bore-scope camera. The solid black line represents the channel floor.

Figure 4.8 (a) shows the laminate at a superheat of 3.3 °C. Isolated bubbles characteristic of partial nucleate boiling are visible in the right view; and, the vapor cloud above the ESM is seen to cover roughly $1/8^{th}$ of the ESM plan-area. The ESM base heat flux is 33.3 W/cm^2.

Fig. 4.8 Flow visualizations of ESM M50/d009/N10. ΔT_{sub} = 10°C, Re = 205

Figure 4.8 (b) shows the laminate at a superheat of 13.9 °C (near CHF for the reference surface). Now the bubbles are coalescing to form larger ones and some vapor columns are observed. Boiling coverage increases to approximately $3/8^{ths}$ of the exposed area. The ESM base heat flux is 33.3 W/cm^2.
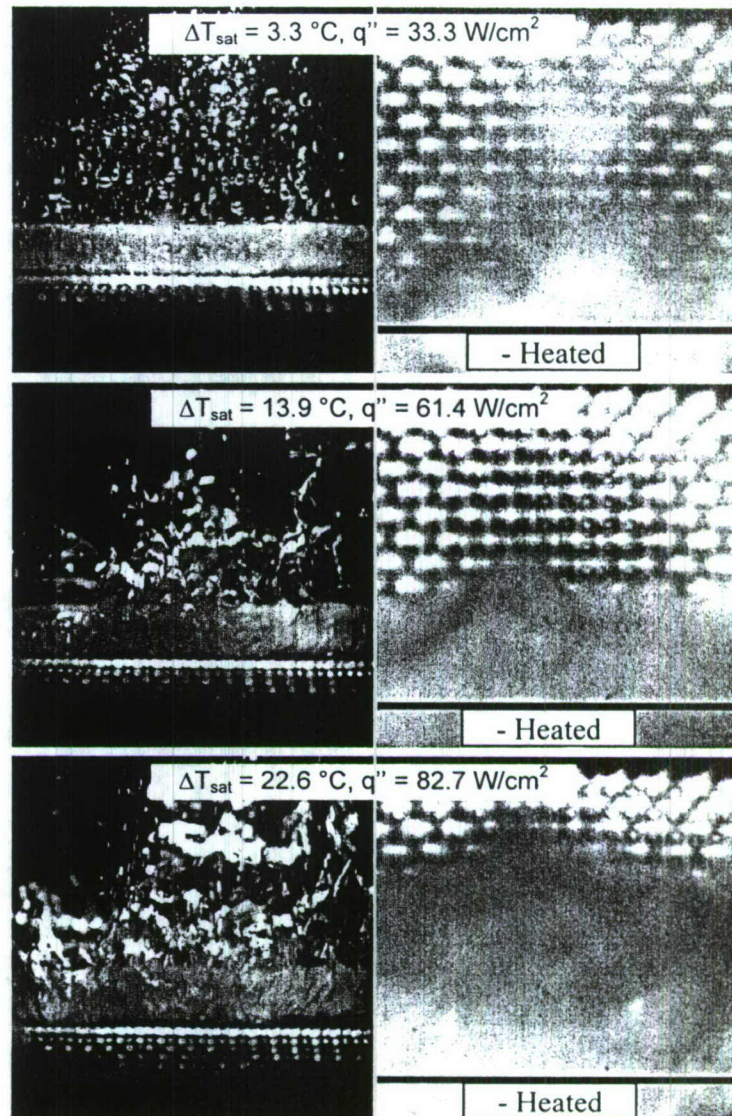
Part (c) shows the laminate at a superheat of 22.6 °C. Now the characteristics of transitional boiling are observed, with some evidence of vapor sheets evident. Boiling coverage increases to roughly 5/8^{ths} of the exposed area.

Additional flow visualizations for the four laminates can be found in Holland [2006].

Figure 4.9 shows the approximate fraction of boiling coverage (the fraction of the channel height, H used in boiling) versus heat flux for the 50-mesh laminates and three Reynolds numbers. The 20-mesh laminates were not well documented in this regard and thus are not shown. Coverage as high as 80% was achieved at the highest heat fluxes, but occurred at a lower heat flux for the 10-layer laminate. In other words, at any given heat flux the 10-layer laminate has higher coverage
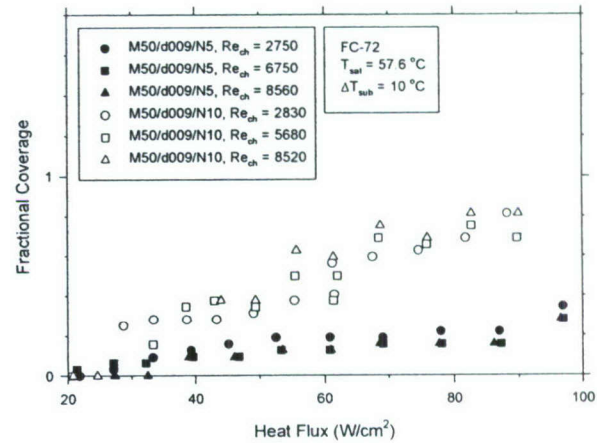

Fig. 4.9 ESM boiling coverage versus base heat flux.

compared to the 5-layer laminate implying that the thicker laminates may experience dry-out sooner than the thinner laminates. This is probably due to the fact that, for the thicker laminates, the quality of the two-phase mixture increases to the point that insufficient liquid is available to cool the downstream portions of the laminate and they are somewhat hotter than the upstream portions. This would cause boiling to extend further into the channel for any given ΔT_{sat}.

Figure 4.10 shows the ESM base heat flux versus superheat for the four laminates at a constant mesh Reynolds number. Values for the M50/d009/N10 laminate are doubly interpolated to a mesh Reynolds number of 250 (Re_{ch} = 6830). Also shown in the figure are select results from two previous investigations: those of Nakayama et al. [1984] and Rainey and You [2000]. The purpose of including these two previous
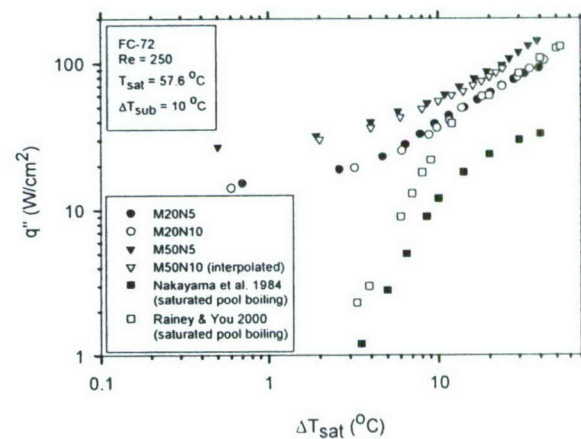

Fig. 4.10 ESM base heat flux comparison at Re = 250

works is not to facilitate any direct comparisons with the present study because test conditions in those studies were not identical to the present work (flow boiling vs. pool boiling, and subcooled vs. saturated fluid). Rather, they are included to show that the results of the present study are reasonable.

Figure 4.10 shows that the highest performance was achieved with the M50/d009/N5 laminate followed closely by the M50/d009/N10 laminate. The two 20 mesh laminates showed nearly the same performance and overlap the results of Rainey and You for superheats greater than 10 °C. All four laminates have similar slopes for superheats greater than 10 °C. This implies that the ESM base heat flux is proportional to $\Delta T_{sat}^{4.3}$.

Figure 4.11 shows the boiling heat transfer coefficient (HTC) versus heat flux for the screen laminates at a fixed mesh Reynolds number. HTC is calculated as $q''/\Delta T_{sat}$. Again, values for the M50/d009/N10 laminate are doubly interpolated to a mesh Reynolds number of 250 (Re_{ch} = 6830). The graph shows that the M50 laminates perform roughly 2X better than the M20 laminates.
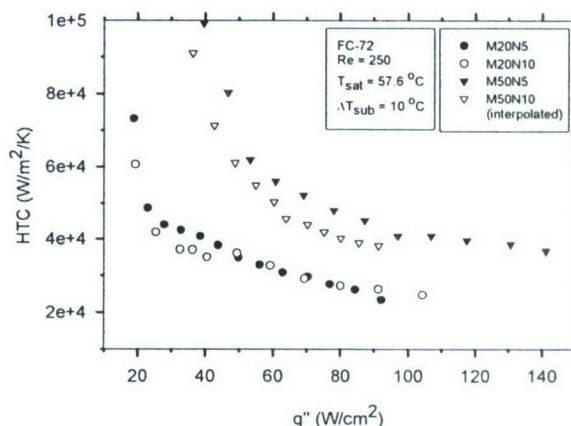

Fig. 4.11 ESM effective heat transfer coefficient (HTC), Re = 250

Figure 4.12 shows the effect of thickness on the heat transfer rate per unit channel width w, at a fixed superheat and constant channel Reynolds number. Values were linearly interpolated and marked with 2-sigma confidence intervals. Also shown is a least squares linear fit. As the graph shows there is an approximately linear relationship between heat transfer rate and thickness. (Pearson's r correlation coefficient = 0.984.) This relationship persists (approximately) at other
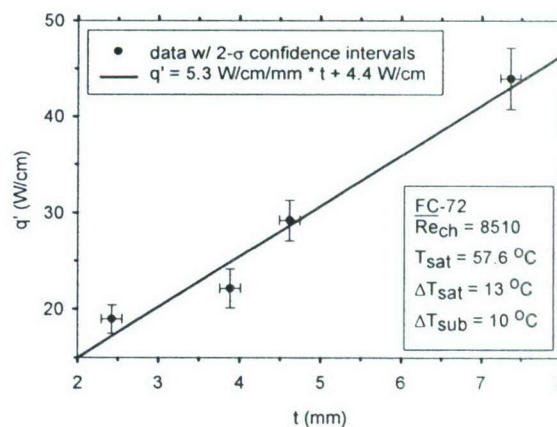

Fig. 4.12 Effect of ESM thickness at constant superheat.

superheats suggesting that a "ballpark" estimate of performance requires knowing only the thickness of the laminate.

Conclusions In conclusion we observe that multi-layered screen laminate ESM's such as those studied in this work can effectively enhance heat transfer over an un-enhanced surface in terms of both surface temperature and heat flux. Of the laminates tested the M50/d009/N5 had the highest performance. Results indicate that devices equipped with this technology can tolerate steady ESM base heat fluxes up to 140 W/cm^2 (based on the base area of the heat sink) with corresponding surface temperatures below 100°C and no evidence of device burnout. Reynolds number has a small effect on performance at lower surface temperatures and a moderate effect at higher temperatures. At superheats greater than 10 °C the ESM base heat flux is proportional to $\Delta T_{sat}^{4.3}$ for the screen laminates tested. HTC for the 50-mesh samples is roughly 2X higher than HTC for the 20-mesh samples. Total capacity (the product of heat flux and base area) of the devices increases approximately linearly with thickness. Boiling coverage for the ten-layer prototypes were higher compared to the five-layer prototypes suggesting that thicker laminates may experience burnout conditions sooner compared to thinner laminates.

5   Mechanical Characterization and Structural Response Modeling

The goal of this part of research was to develop models to characterize the mechanical performance of the heat exchanger structures. After the validation with benchmark experiments, the models developed can be applied to optimize the mechanical behavior in the design of the AORS with an integrated consideration of the thermal performance.

5.1   Material and Specimen Design

Aluminum alloys are light-weight with high thermal conductivity, attractive strength and great manufacturability. Since most aluminum alloys have similar thermal conductivity, a high strength aluminum alloy was selected for the project. 7075-T6 met the high strength requirement with a desirable ductility, and it was selected for the current research.

As shown in Fig. 5-1, four types of testing specimens were used in the experiments. They were uniaxial dog-bone plate specimens (Fig. 5-1(a)), uniaxial solid cylindrical specimens (Fig. 5-1(b)), cylindrical specimen for torsion (Fig. 5-1(c)), and tubular specimens for axial-torsion loading (Fig. 5- 1(d)). The dog-bone plate specimens were machined from a large plate. Both the uniaxial cylindrical solid specimen and the specimens for torsion were fabricated from a cylindrical bar with a diameter of 25.4 mm. A solid bar with a diameter of 38mm was used to fabricate the tubular specimens. The plate specimens were made in two directions with respect to the rolling direction of the plate.

Since the materials were acquired commercially and the materials were cold-rolled, an inspection of the microstructure may help identify whether or not the materials were practically identical. Figure 5-2 shows the optical stereographic microstructures of materials taken from the plate, rod-shaped, and tubular specimens of 7075-T6.
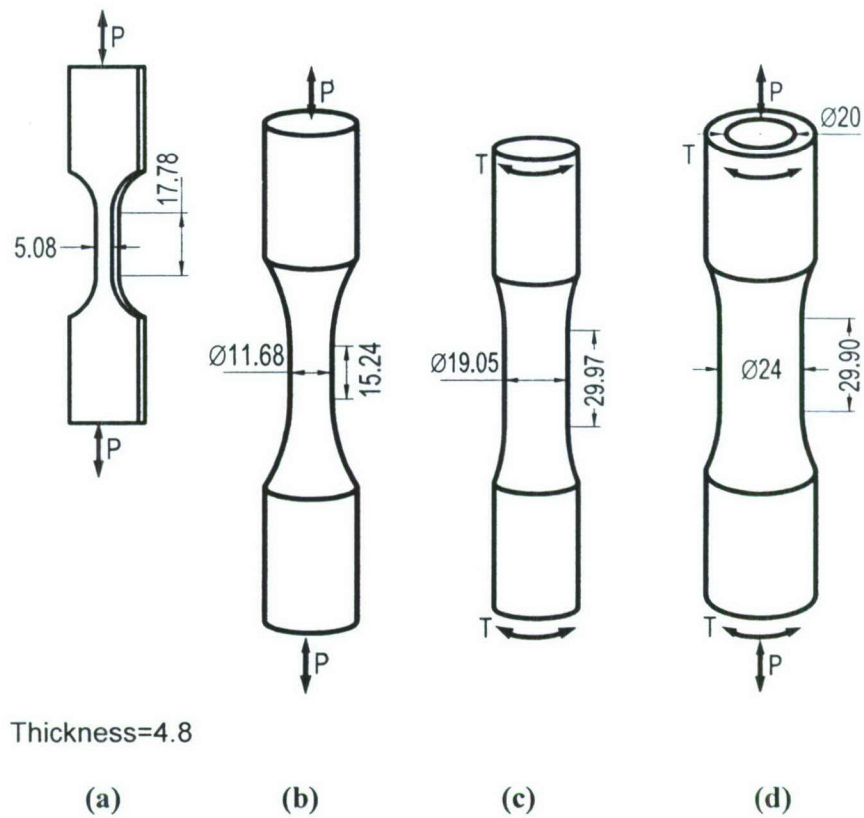
Fig. 5-1 Specimens and loading conditions (all dimensions in mm)

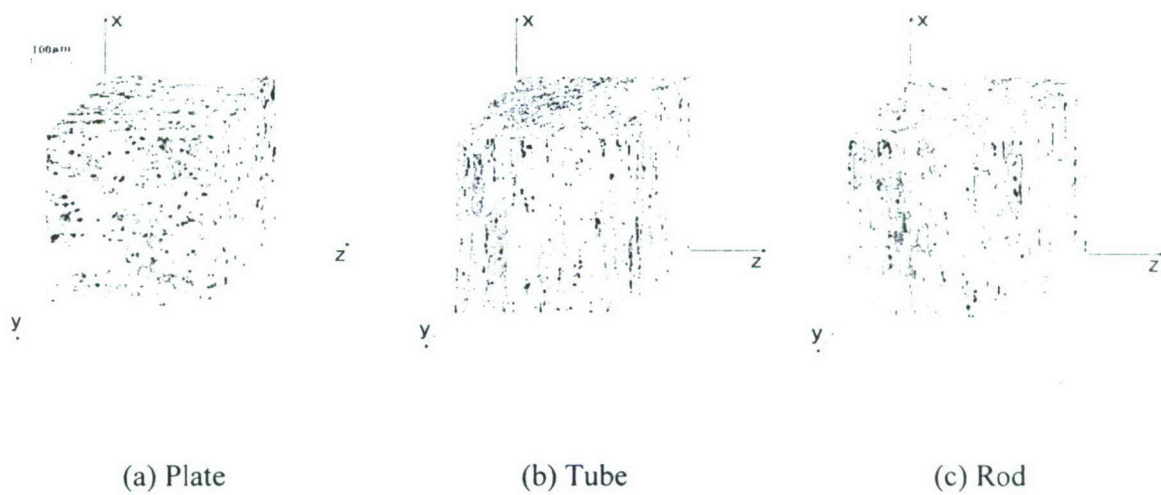

(a) Plate　　　　　　(b) Tube　　　　　　(c) Rod

Fig. 5-2 Stereographic microstructure of the material

Each stereography was synthesized from three microstructures taken on the sections perpendicular to the rolling (x) direction, the normal (y) direction, and the transversal (z) direction. The etchant for use in microscopic examination was Keller's reagent (2ml HF (48%), 3ml HCl, 5ml HNO_3, 190 ml H_2O). Dark particle-like precipitates in the microstructures are $Cr_2Mg_3Al_{18}$ and $(Fe,Mn)Al_6$.

For the plate specimen, equiaxial grains were observed on the rolling plane (section perpendicular to the normal direction). The grain size varies from 10 microns to 100 microns. The average grain size is approximately 50 microns. On the sections perpendicular to the rolling direction and the transverse direction, fibrous grains were observed. The average thickness of grains is approximately 7 microns. It is a typical microstructure after cold rolling (disk-like grains).

For the rod-shaped specimens, the grains appear equiaxial on the section perpendicular to the axis. The grain size ranges from 10 microns to 40 microns. On the section parallel to the axis, fibrous grains are observed. The average length of grains along axial direction is about 70 microns. It is a typical microstructure after cold-drawn or cold extrusion (fibrous grains).

Tubular specimens were machined from rod-shaped specimens. There is no essential difference between their microstructures.

5.2   Testing Equipment

An Instron Servohydraulic tension-torsion load frame was used for the fatigue experiments of cylindrical specimens and tubular specimens shown in Fig. 5-1. The testing system, which has a capacity of ±2800 N.m in torque and ±222 kN in axial load, is equipped with the Instron 8800 electronic control, computer control and data acquisition. A 12.7mm gage length uniaxial extensometer was used for the measurement of the strain in the gage section of the uniaxial specimen. The extensometer had a range of ±5% strain. For the tubular specimens and the specimens for torsion, a modified MTS extensometer was attached to the gage section of the specimen to measure the axial, shear, and diametral strains. The extensometer had a range of ± 5% in the axial strain, a range of ± 3 degree in the torsion deformation, and 0.25 mm range in the diametral direction. An Instron 8870 load frame with 8800 electronics and computer control was used for monotonic experiments and some of the uniaxial fatigue experiments using the plate specimens. The load cell has a capability of ±25kN axial load. All the experiments were

conducted in ambient air. When the temperature is lower than 150 °C, the mechanical properties of the aluminum alloy are not influenced by the temperature [Cavaliere and Squillace, 2005].

5.3   Monotonic Experiments and Results

Monotonic tension experiments were conducted using the dog-bone plate specimens. The stress-strain curve obtained the monotonic tension experiments are shown in Fig.5-3. The true fracture stress of the material, σ_f, was obtained by conducting a monotonic torsion experiment. Figure 5-4 displays the shear stress-shear strain curve obtained from testing a round solid specimen (Fig.5-1(c)) subjected to monotonic torsion. The surface strain was measured by using an extensometer and the surface stress was determined following the Nadai's formula [Nadai, 1950]. From Fig. 5-4, the fracture shear stress under pure shear, τ_f, was 378.9 MPa. By using the relationship, $\sigma_f = \sqrt{3}\tau_f$, the fracture stress, σ_f, was 656.3 MPa. A monotonic torsion experiment can also experimentally determine the true fracture strain. All the static material properties of 7075T6 are summarized in Table 5-1.
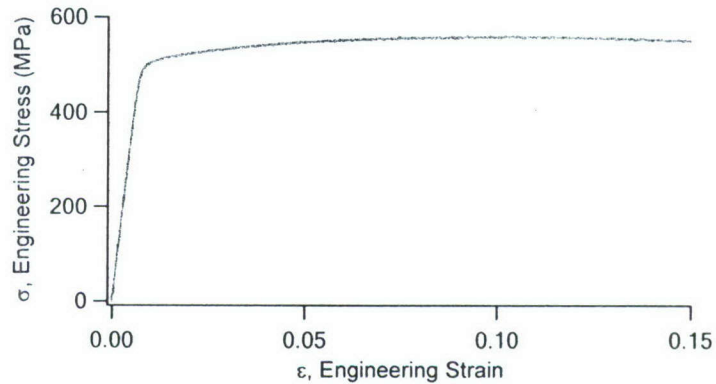

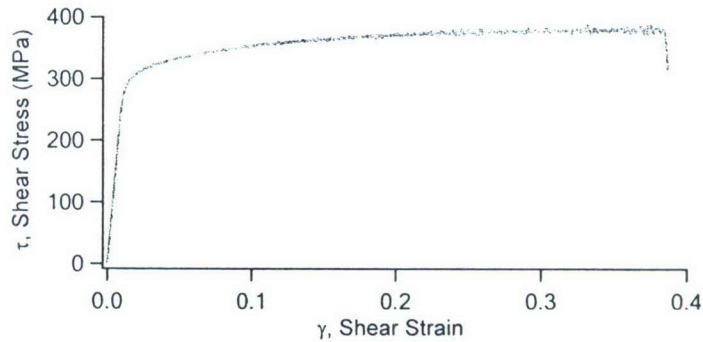**Fig.5-3** Stress-strain curve obtained from monotonic tension

Fig. 5-4 Shear stress-shear strain curve of 7075T6 under monotonic torsion

Table 5-1. Static material properties of 7075T6

Elasticity Modulus, E	71.7GPa
Shear Modulus, G	27.5GPa
Poisson's Ratio, μ	0.306
Yield Stress, $\sigma_{0.2}$	501.1 MPa
Ultimate Strength, S_u	560.85MPa
Elongation, e_f	9.7%
Reduction in Area, RA	29.1 %
True Shear Fracture Stress, τ_f	378.9MPa
True Fracture Strain, γ_f	0.384

5.4   Fatigue Experiments and Results

Fatigue experiments were conducted using the specimens shown in Fig.5-1. A great number of uniaxial fatigue experiments were carried out to establish the fatigue and deformation baselines of the material. Tubular specimens were used to generate the fatigue properties under complex stress state and the results can be used to evaluate the fatigue models.

Figure 5-5 shows the loading paths used in the axial-torsion experiments for the tubular specimens. Six load paths were applied. Figure 5-5(a) is pure shear loading, and Fig.5-5(b) is a loading case with fully reversed shear and a static axial stress. Figure 5-5(c) is the proportional loading path. Figure 5-5 (d) is a circular shaped axial-torsion nonproportional loading path. Loading paths shown in Fig. 5-5(e) and Fig. 5-5(f) are nonproportional loading paths with the ratios of the torsion loading frequency over the axial loading frequency being two and four, respectively.
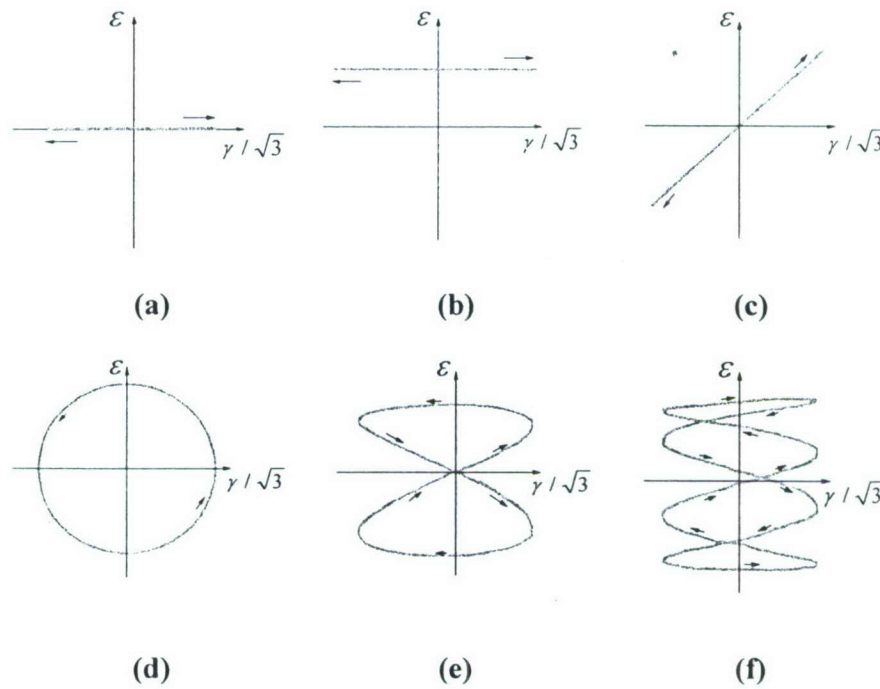
Fig. 5-5 Loading paths for axial-torsion loading using tubular specimens

The detailed experimental results are summarized in Table 5-2 ~ Table 5-6. Table 5-2 lists most of the results obtained from testing the plate or dog-bone shaped cylindrical uniaxial specimens. Table 5-3 is dedicated to the uniaxial specimens loaded with a compressive mean stress. Table 5-4 lists the pure torsion results obtained from testing the solid shaft specimen (Fig. 5-1(c)). The torsion fatigue results obtained from testing the tubular specimens are summarized in Table 5-5 together with these results from cyclic torsion with a static axial load. The results obtained from testing the tubular specimen under proportional and nonproportional loading are listed in Table 5-6.

Table 5-2 Results from plate and dog-bone cylindrical uniaxial specimens

a) Dog-bone cylindrical uniaxial specimens

Spec No.	$\dfrac{\Delta\varepsilon}{2}$ %	$\dfrac{\Delta\sigma}{2}$ MPa	σ_m MPa	N_f cycles	Spec No.	$\dfrac{\Delta\varepsilon}{2}$ %	$\dfrac{\Delta\sigma}{2}$ MPa	σ_m MPa	N_f cycles
TorS43	3.09	630.8	-0.2	25	TorS37	0.51	361.6	-3.6	9,112
TorS45_2	2.55	614.0	-2.3	58	TorS32	0.42	299.6	1.5	27,011
TorS41	2.02	592.9	-3.3	73	TorS33	0.34	240.0	1.1	99,287
TorS44	1.53	567.5	-5.2	125	TorS38	0.28	200.2	0.6	919,687
TorS39_2	1.23	555.2	-7.8	194	TorS34_1	0.21	150.0	0.4	1,063,477
TorS40	1.02	533.8	-7.2	390	TorS45_1	0.30	214.9	1.0	1,090,639
TorS34_2	0.81	512.2	-7.3	794	TorS39_1	0.29	210.1	1.4	1,108,763
TorS36	0.72	485.5	8.9	917					
TorS35	0.56	400.1	2.8	3,073					
TorS42	0.49	349.7	2.1	7,144					

$\Delta\varepsilon/2$ = axial strain amplitude, $\Delta\sigma/2$ = axial stress amplitude, σ_m = mean stress, N_f = fatigue life

b) 0° plate specimen

Spec No.	$\frac{\Delta\varepsilon}{2}$ %	$\frac{\Delta\sigma}{2}$ MPa	σ_m MPa	N_f cycles	Spec No.	$\frac{\Delta\varepsilon}{2}$ %	$\frac{\Delta\sigma}{2}$ MPa	σ_m MPa	N_f cycles
0-56	4.00	627.5	3.5	5	0-17	0.29	210.2	15.5	109,557
0-55	3.92	625.2	5.7	7	0-12	0.27	191.4	0.7	116,333
0-53	2.92	600.1	-1.3	14	0-41	0.22	157.0	0.7	182,900
0-52	2.43	584.5	-2.9	15	0-28	0.24	167.4	0.6	624,994
0-51	2.44	583.8	-1.8	34	0-29	0.21	154.1	-0.1	1,079,668
0-34	1.53	537.9	-4.3	45	0_25	0.40	268.1	268.2	5,275
0-39	1.23	528.4	-8.7	112	0_19	0.41	284.7	221.3	6,144
0-32	1.02	511.5	-9.3	200	0_23	0.40	280.1	159.9	12,288
0-57	0.91	509.5	-13.2	415	0_22	0.32	220.1	220.0	17,885
0-33	0.82	493.2	-7.4	512	0_21	0.29	200.5	200.5	34,956
0-10	0.71	489.3	0.2	945	0_24	0.25	177.6	177.7	54,680
0-18	0.65	488.4	-39.0	713	0_20	0.21	146.6	146.6	209,237
0-03	0.60	434.5	-36.0	3,357	0_27	0.19	133.0	133.1	1,075,867
0-16	0.61	435.7	73.0	2,055	0_26	0.17	118.7	118.7	1,283,726
0-36	0.64	455.5	-5.8	2,635	0_67	0.19	143.9	240.4	79,324
0-05	0.46	333.2	-22.2	9,010	0_69	0.67	455.5	54.2	871
0-01	0.51	368.8	-54.4	11,504	0_68	0.58	404.0	103.8	1,045
0-15	0.41	301.8	39.1	22,121	0_70	0.50	353.7	152.5	2,862
0-38	0.42	299.3	1.3	27,788	0_71	0.29	203.2	303.5	7,315
0-04	0.42	299.3	-34.4	40,930	0_73	0.22	153.0	354.8	14,782
0-31	0.37	262.4	1.2	47,740	0_72	0.17	121.7	384.6	24,979
0-06	0.36	258.1	1.2	55,470	0_54	0.16	108.4	497.5	11,639
0-07	0.31	222.1	1.0	51,717	0_59	0.11	75.7	432.1	245,801
0-35	0.31	222.0	1.1	58,666	0_55	0.10	70.7	435.8	1,608,028

$\Delta\varepsilon/2$ =axial strain amplitude, $\Delta\sigma/2$ = axial stress amplitude, σ_m =mean stress, N_f = fatigue life

c) 90° plate specimen

Spec No.	$\frac{\Delta\varepsilon}{2}$ %	$\frac{\Delta\sigma}{2}$ MPa	σ_m MPa	N_f cycles	Spec No.	$\frac{\Delta\varepsilon}{2}$ %	$\frac{\Delta\sigma}{2}$ MPa	σ_m MPa	N_f cycles
90-69	3.51	633.7	-5.3	4	90-31	0.23	161.9	0.5	1,450,963
90-41	0.97	515.9	-15.2	175	90-30	0.22	155.3	0.4	1,117,723
90-37	1.07	522.1	-14.3	232	90_24	0.40	268.1	268.0	4,012
90-39	0.72	478.8	-14.6	759	90_19	0.42	293.1	92.4	20,691
90-09	0.77	497.2	-21.7	788	90_21	0.32	222.2	221.9	20,306
90-13	0.70	486.0	-7.4	884	90_22	0.29	200.5	200.4	25,645
90-17	0.73	492.7	11.5	1,212	90_23	0.25	175.9	175.9	45,294
90-40	0.62	439.9	3.2	1,265	90_25	0.25	175.7	175.8	45,967
90-06	0.62	444.0	-9.9	1,880	90_26	0.19	133.0	133.0	196,177
90-15	0.67	473.7	-17.6	2,268	90_28	0.18	127.2	127.3	210,014
90-18	0.47	395.9	-44.7	2,299	90_20	0.21	147.7	147.6	227,619
90-02	0.53	378.3	-31.3	4,429	90_34	0.18	122.8	122.8	716,425
90-42	0.52	370.2	2.7	9,035	90_29	0.18	124.8	124.8	932,194
90-07	0.42	300.1	-19.6	18,120	90_27	0.17	120.1	120.1	1,271,590
90-14	0.48	349.3	-16.9	21,053	90_35	0.17	121.2	121.3	1,415,524
90-08	0.36	259.9	1.3	40,443	90_58	1.12	557.7	69.0	17
90-03	0.35	250.0	1.2	42,650	90_59	0.96	549.2	95.5	22
90-10	0.32	222.6	1.0	104,240	90_60	0.72	507.3	129.4	405
90-16	0.32	228.3	-12.5	164,041	90_61	0.46	323.5	282.9	1,674
90-12	0.28	190.6	0.7	131,072	90_62	0.31	218.1	390.0	3,649
90-38	0.22	161.6	0.1	394,116	90_53	0.15	101.8	405.8	28,813
90-32	0.24	173.7	0.4	625,893	90_52	0.12	82.0	425.5	141,596
90-66	0.21	144.8	-0.8	865,205	90_55	0.13	91.9	413.7	233,252
90-33	0.23	168.4	0.6	1,091,584					

$\Delta\varepsilon/2$ = axial strain amplitude, $\Delta\sigma/2$ = axial stress amplitude, σ_m = mean stress, N_f = fatigue life

Table 5-3 Uniaxial loading with compressive mean stress

a) One step loading

Spec No.	$\frac{\Delta\varepsilon}{2}$ %	$\frac{\Delta\sigma}{2}$ MPa	σ_m MPa	N_f cycles	Spec No.	$\frac{\Delta\varepsilon}{2}$ %	$\frac{\Delta\sigma}{2}$ MPa	σ_m MPa	N_f cycles
0_74	0.55	397.0	-96.9	6,513	0_66	0.35	313.1	-278.8	464,808
0_76	0.48	347.4	-147.0	18,217	90_51	0.27	198.7	-99.9	368,183
0_75	0.41	297.1	-197.0	115,601	90_56	0.40	295.5	-246.4	405,747
0_58	0.40	310.2	-262.6	212,001	90_63	0.38	316.3	-285.6	429,914
0_77	0.34	249.2	-148.2	222,563	90_64	0.40	315.0	-292.1	565,104
0_60	0.38	278.6	-215.0	226,682	90_57	0.37	273.3	-223.5	603,299
0_61	0.32	237.5	-161.6	288,283	90_65	0.38	315.3	-297.6	696,820
0_64	0.31	228.3	-169.1	291,220	90_72	0.39	300.9	-302.1	750,172
0_65	0.41	305.0	-268.1	383,667	90_68	0.39	307.0	-298.2	1,098,940
0_63	0.37	274.0	-221.5	406,747					

$\Delta\varepsilon/2$ = axial strain amplitude, $\Delta\sigma/2$ = axial stress amplitude, σ_m = mean stress, N_f = fatigue life

b) plate and cylindrical specimens, two step loading

Spec No.	$\frac{\Delta\varepsilon}{2}$ %	$\frac{\Delta\sigma}{2}$ MPa	σ_m MPa	N_f cycles	Spec No.	$\frac{\Delta\varepsilon}{2}$ %	$\frac{\Delta\sigma}{2}$ MPa	σ_m MPa	N_f cycles
90_67	0.41	305.3	-291.1	498,374	90_78	0.36	274.4	-322.1	982,635
		100.0	100.0	62			100.0	100.0	19,335
90_71	0.42	301.4	-292.6	472,623	TorS21	0.41	308.1	-318.4	1,000,000
		100.0	100.0	52			100.0	100.0	29,831
90_73	0.38	300.8	-310.3	802,796	TorS22	0.42	307.4	-317.2	2,000,000
		100.0	100.0	419			100.0	100.0	23,867
90_74	0.38	292.2	-311.8	880,885	TorS23	1.67	271.1	-274.5	1,371,663
		100.0	100.0	1,926			100.0	100.0	15,353
90_75	0.44	289.3	-300.3	397,716	TorS24	1.70	271.3	-266.7	2,781,162
		100.0	100.0	15,473			100.0	100.0	49,221
90_77	0.40	298.3	-299.2	375,132					
		100.0	100.0	3,198					

$\Delta\varepsilon/2$=axial strain amplitude, $\Delta\sigma/2$=axial stress amplitude, σ_m=mean stress, N_f=fatigue life.

Table 5-4 Pure torsion for the solid shaft specimens

Spec No.	$\frac{\Delta\gamma}{2}$, %	$\frac{\Delta\tau}{2}$, MPa	$\frac{\Delta T}{2}$, Nm	N_f cycles
Tor17	2.10	327.6	829.4	142
Tor02	2.43	332.9	850.7	146
Tor03	1.51	312.2	743.3	509
Tor15	1.17	290.5	660.5	1,664
Tor06	1.15	288.6	634.1	5,525
Tor05	0.89	238.1	507.8	19,067
Tor16	0.72	194.7	420.2	33,710
Tor04	0.62	319.6	360.3	331,247
Tor14	0.55	151.0	322.7	371,959

$\Delta\gamma/2$=shear strain amplitude, $\Delta\tau/2$=shear stress amplitude, $\Delta T/2$=torque amplitude,

N_f= fatigue life.

Table 5-5 Pure torsion and cyclic torsion with static axial load for tubular specimens

Load path	Spec No.	σ_m MPa	$\frac{\Delta\gamma}{2}$ %	$\frac{\Delta\tau}{2}$, MPa	N_f cycles	Observed Cracking Direction
	Tu31	0	1.97	335.2	152	90
	Tu18	0	1.73	340.0	209	90
	Tu17	0	1.21	315.7	670	5
	Tu16	0	0.93	254.2	4,291	90
	Tu30	0	0.80	219.0	20,271	90
(a)	Tu15	0	0.69	190.3	178,065	0
	Tu27	0	0.60	167.8	308,144	-45
	Tu24	0	0.69	192.0	328,816	0
	Tu10	0	0.50	136.5	403,731	0
	Tu28	0	0.40	110.8	805,783	45
	Tu31_1	0	0.45	125.8	1,005,181	-
	Tu22	200	0.69	188.5	12,739	0
(b)	Tu23	-200	0.69	192.0	52,986	90
	Tu25	293.1	0.69	189.8	4,394	90
	Tu26	-293.1	0.69	196.7	84,946	90

σ_m=static axial stress, $\Delta\gamma/2$=shear strain amplitude, $\Delta\tau/2$= shear stress amplitude, N_f=fatigue life.

Table 5-6 Fatigue experiments conducted using tubular specimens

Load path	Spec No.	$\frac{\Delta\varepsilon}{2}$, %	$\frac{\Delta\gamma}{2}$, %	$\frac{\Delta\sigma}{2}$, MPa	$\frac{\Delta\tau}{2}$, MPa	N_f cycles	Observed Cracking Direction
	Tu06	0.64	1.1	370.0	222.9	147	60
	Tu04	0.50	0.86	351.3	222.0	1,967	20
	Tu19	0.22	0.78	165.6	216.2	9,174	90
	Tu20	0.17	0.6	127.2	170.5	59,194	-5
(c)	Tu33	0.23	0.4	166.1	110.4	136,646	90
	Tu05	0.28	0.49	201.3	130.0	45,500	-49
	Tu32	0.21	0.37	153.5	100.3	662,627	-50
	Tu06_1	0.19	0.29	137.4	79.7	1,018,000	-
	Tu29_1	0.18	0.36	132.4	96.8	1,031,190	-
	Tu29	0.85	1.45	543.7	329.4	146	5
	Tu02	0.75	1.30	497.7	319.1	424	-5
	Tu01	0.51	0.87	377.6	241.8	2,487	-5
(d)	Tu21	0.38	0.66	280.4	181.8	10,191	0
	Tu11	0.28	0.49	200.9	131.6	29,439	-30
	Tu03	0.27	0.41	200.6	115.8	41,747	0
	Tu02_1	0.19	0.27	143.1	76.4	632,258	-
	Tu09	0.49	0.86	352.0	232.0	755	15
(e)	Tu07	0.28	0.49	205.8	137.5	35,804	20
	Tu08	0.20	0.32	147.5	86.9	225,000	-21
	Tu13	0.36	0.63	258.2	175.6	1,145	-30
(f)	Tu14	0.40	0.70	295.0	197.2	2,301	-19
	Tu12	0.28	0.49	203.8	136.3	12,708	-20

$\Delta\varepsilon/2$ =axial strain amplitude, $\Delta\gamma/2$ =shear strain amplitude, $\Delta\sigma/2$ =axial stress amplitude, $\Delta\tau/2$ =shear stress amplitude, N_f =fatigue life.

The average shear stress and shear strain in the gage section of the tubular specimen were used to report the experimental results. The average shear stress was obtained by assuming uniform shear stress distributions over the wall thickness of the specimen. A linear shear strain distribution over the wall thickness of the specimen was assumed and the midsection shear strain was used as the average shear strain.

Figure 5-6 shows the typical stabilized stress-plastic strain hysteresis loops obtained from the fully reversed tension-compression experiments. The plastic strain is the result of the total strain subtracting the elastic strain. The deformation behavior shown in Fig. 5-6 will be used in the elastic-plastic stress analysis of the component subjected to fatigue loading.
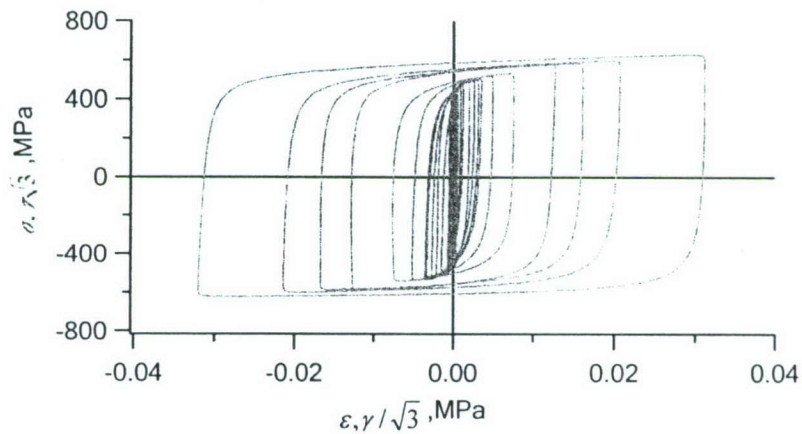
Fig. 5-6 Cyclic stress-plastic strain hysteresis loops

Figures 5-7 and 5-8 show the basic fatigue data obtained from the fully reversed uniaxial loading. A data point followed by a horizontal arrow denotes a run-out fatigue experiment. It is evident that the plate specimens with two different orientations and the solid dog-bone cylindrical specimens yielded very similar fatigue results.
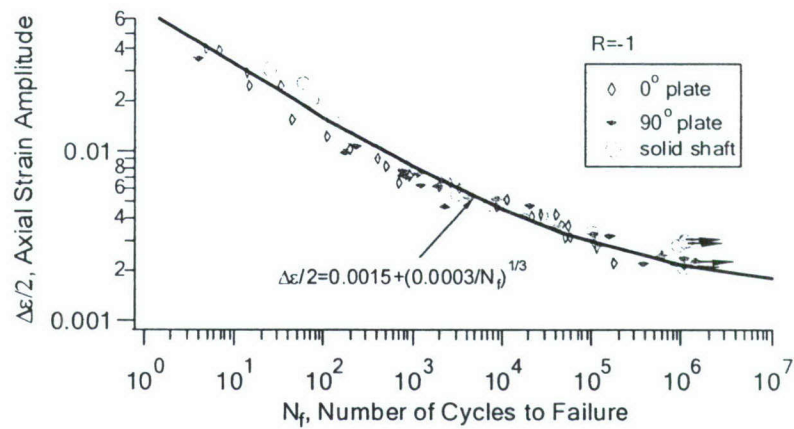
Fig. 5-7 Strain-life under fully reversed uniaxial loading

The strain-life curve is described by:

$$\Delta\varepsilon/2 = 0.0015 + (0.0003/N_f)^{1/3}$$
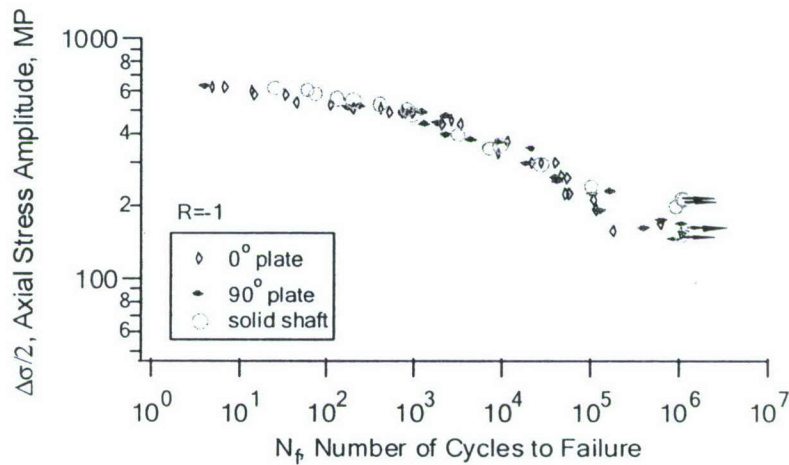
Fig. 5-8 Stress-Life under fully reversed uniaxial loading

Uniaxial fatigue experiments were conducted with R-ratios ranging from $-\infty$ to 0.5, where R is the ratio of the minimum stress over the maximum stress in a loading cycle. The fatigue results are shown in Figs. 5-9 and 5-10. Figure 5-9 is the strain-life plot and Fig. 5-10 is the stress-life plot. Clearly, the mean stress has a significant influence on the fatigue life. With identical strain amplitude, a positive mean stress reduced the fatigue life dramatically. A compressive mean stress enhanced the fatigue life.

75
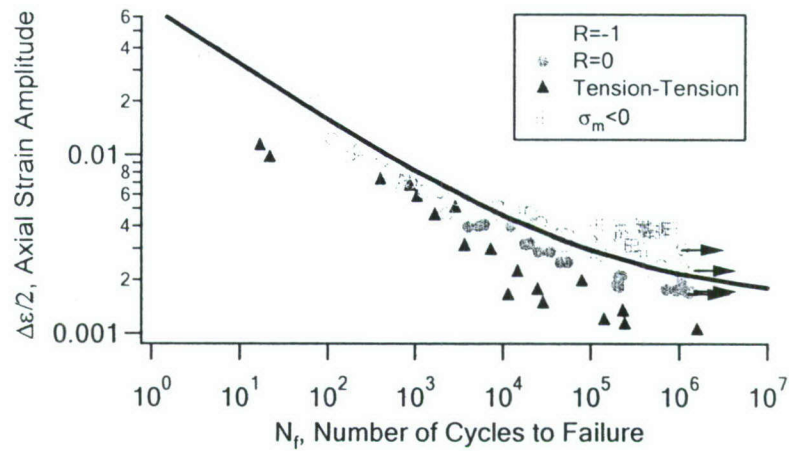
Fig. 5-9 Strain-life of all the uniaxial fatigue experiments
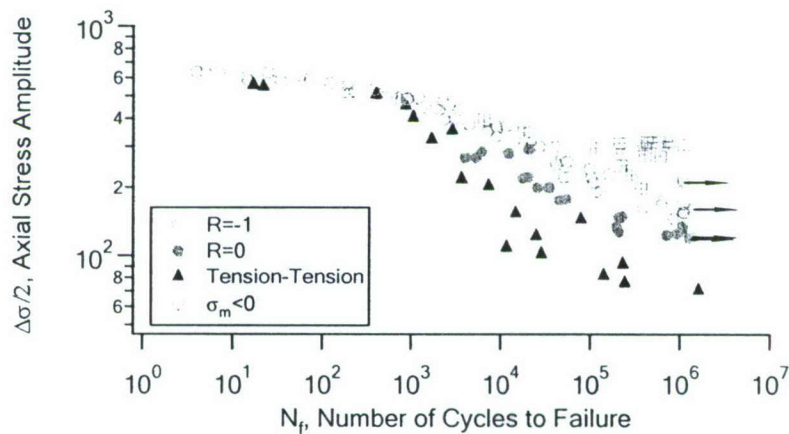
Fig. 5-10 Stress-life of all the uniaxial fatigue experiments

A number of uniaxial specimens were tested under the compression-compression condition with zero or negative maximum stress in the loading cycle. In order to assess fatigue damage under compression-compression loading, a specimen was subjected to a designated compression-compression loading for 10^6 loading cycles. This was followed by a stress-controlled loading with $R = 0$ and with the stress amplitude being 100 MPa. According to the results shown in Fig. 5-5, a stress amplitude of 100 MPa with $R = 0$ would result in a fatigue life longer than 10^7 loading cycles. Since fatigue cracks were often initiated on the material plane having its normal along the loading axis (the crack plane was perpendicular to the loading direction), failure of the specimen was difficult to identify under compression-compression loading. The two-step

loading can help identify whether or not the compression-compression generated fatigue damage. If the number of loading cycles in the second loading step is significantly long, this may indicate that the fatigue damage created under the first step compression-compression may not have contributed to the fatigue damage. If the specimen fails in the second loading step within a number of loading cycles that is much less than 10^7, the first loading step must have generated significant fatigue damage.

All the 11 uniaxial specimens tested under the compression-compression loading conditions failed in the second step loading with a stress amplitude of 100MPa and $R = 0$ within very limited number loading cycles. The results suggest that fatigue damage was developed under compression-compression loading. In fact, the results show that fatigue damage has reached a failing point already before the application of the second loading step.
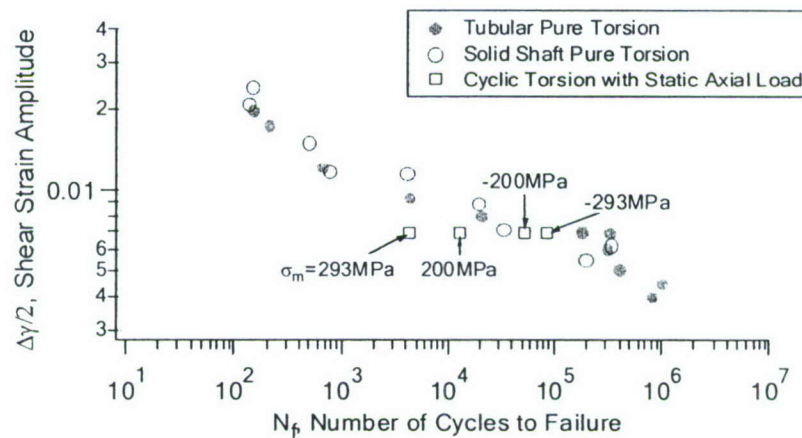
Fig. 5-11 Shear strain amplitude versus fatigue life for torsion and torsion with a static axial stress
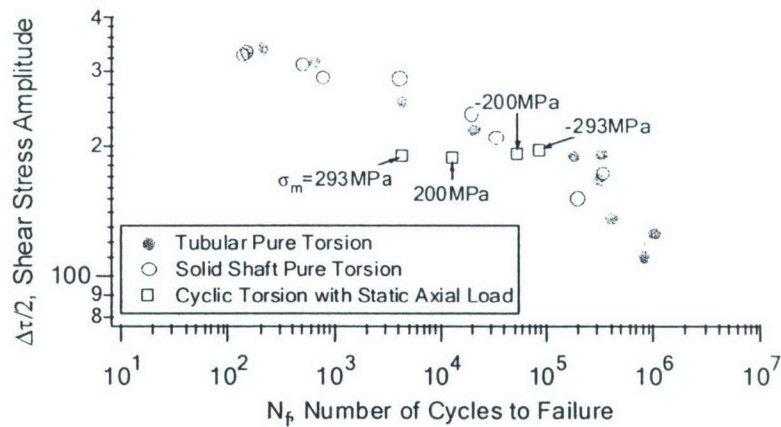
Fig. 5-12 Shear stress amplitude versus fatigue life for torsion and torsion with a static axial

Figures 5-11 and 5-12 show the fatigue results obtained from the pure shear experiments and the fatigue experiments conducted with cyclic shear combined with a static axial stress. The results obtained from testing the solid shaft under cyclic torsion are also included in Figs. 5-11 and 5-12. The shear stress amplitude for the solid shaft under torsion was obtained using the stress-strain relationship shown in Fig. 5-6. The results shown in these two figures indicate that the torsion fatigue using a solid shaft is suitable. A solid shaft is much easier to fabricate than a tubular specimen. A positive static axial static stress significantly reduces fatigue life. On the other hand, a compressive static axial stress enhances the fatigue life slightly.

It is noted in Fig. 5-11 that when the fatigue lives are long, the shape of the S-N curve is different. An examination of the cracking behavior (Table 5-5) suggests that when the fatigue life is lower than 4000 cycles, the material displays shear cracking. When the fatigue life is longer than 300,000 cycles, the material displays tensile cracking.

Materials subjected to fatigue loading can be classified into three types according to the cracking behavior. Some materials display shear cracking where fatigue cracks are observed on the material plane of maximum shear amplitude and some materials exhibit tensile cracking where cracks are initiated on the plane of maximum normal stress. Other materials display a mixed cracking behavior where cracks are initiated on the maximum normal planes for tension-compression loading but on the maximum shear plane under pure shear loading. The experimental results obtained from tension-compression and torsion suggest that the material under investigation displays, shear, mixed, and tensile cracking behavior dependent on the

loading magnitude. When the loading magnitude is high, the material displays shear cracking. When the loading magnitude is low, the material exhibits tensile cracking.

Figures 5-13 and 5-14 summarize the results obtained from testing the tubular specimens under combined axial-torsion loading. Equivalent stress and strain are used to represent the loading magnitude under cyclic loading. The equivalent stress and the equivalent strain are defined as follows,

$$\left(\frac{\Delta\sigma}{2}\right)_{eq} = \sqrt{\left(\frac{\Delta\sigma}{2}\right)^2 + 3\left(\frac{\Delta\tau}{2}\right)^2} \qquad (5\text{-}1)$$

$$\left(\frac{\Delta\varepsilon}{2}\right)_{eq} = \sqrt{\left(\frac{\Delta\varepsilon}{2}\right)^2 + \frac{1}{3}\left(\frac{\Delta\gamma}{2}\right)^2} \qquad (5\text{-}2)$$

where $\left(\Delta\sigma/2\right)_{eq}$ is the equivalent stress and $\left(\Delta\varepsilon/2\right)_{eq}$ is the equivalent strain. $\Delta\sigma/2$ and $\Delta\varepsilon/2$ are the axial stress amplitude and the axial strain amplitude, respectively. $\Delta\tau/2$ is the shear stress amplitude and $\Delta\gamma/2$ is the shear stress amplitude.
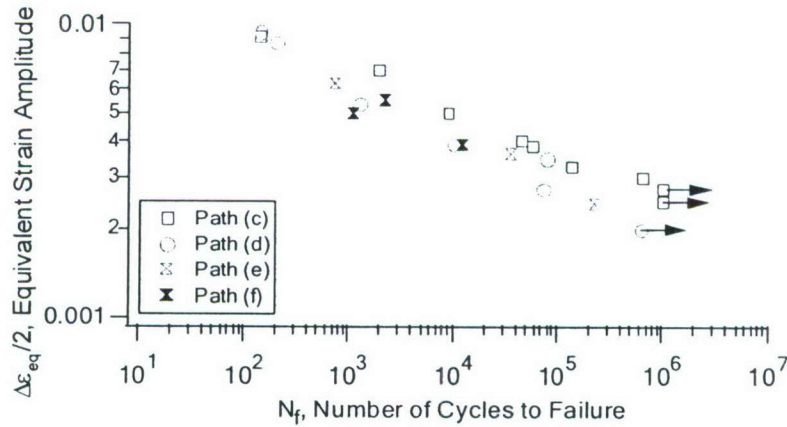
Fig. 5-13 Fatigue under combined axial-torsion loading
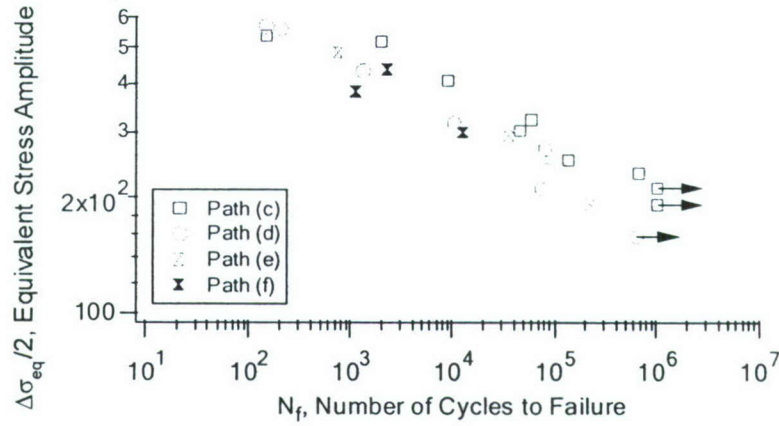
Fig. 5-14 Equivalent stress versus fatigue life under combined axial-torsion loading

The fatigue experimental results obtained from testing the tubular specimens will be used to evaluate the fatigue models.

5.5 Smith, Watson, and Topper (SWT) Criterion

Smith, Watson, and Topper (SWT) [Smith, R.N et. al, 1970] developed a fatigue model to consider the mean stress effect for uniaxial loading by using the product of the cyclic strain range and the maximum stress,

$$FP = \Delta \varepsilon \sigma_{max} \qquad (5\text{-}3)$$

where $\Delta \varepsilon$ is the strain range and σ_{max} is the maximum stress in a loading cycle. *FP* denotes "fatigue parameter." A major development in fatigue life predictions is the confirmation of the critical plane approaches. A critical plane approach concerns a critical plane in a given material for a known stress state on which cracks nucleate. The notion is that cracking behavior is material and loading magnitude dependent. Socie [Socie, 1987] extended the SWT parameter to multiaxial fatigue with a critical plane interpretation. The critical plane was defined as the material plane where the normal strain range was a maximum. The normal strain range, $\Delta \varepsilon$, and the maximum normal stress, σ_{max}, in Eq. (5-3) are taken on the critical plane. The criterion predicts tensile cracking.

The SWT parameter has been known to correlate well with the fatigue experiments of aluminum alloys. Figure 5-15 shows the SWT parameter versus fatigue life for the uniaxial specimens experimentally tested in the current investigation. It is clear that the parameter correlates the experiment well for most of the uniaxial loading cases. Exceptions are the loading conditions with large compressive mean stresses. Several specimens were tested with a positive maximum stress being close to zero. As a result, the SWT fatigue parameter was very small according to Eq. (5-3). These are the data points shown in Fig. 5-15 that deviate significantly from the general tendency line. As has been well recognized, the SWT parameter assumes zero fatigue damage when the maximum stress is negative. The parameter fails to correlate the compression-compression experiments.
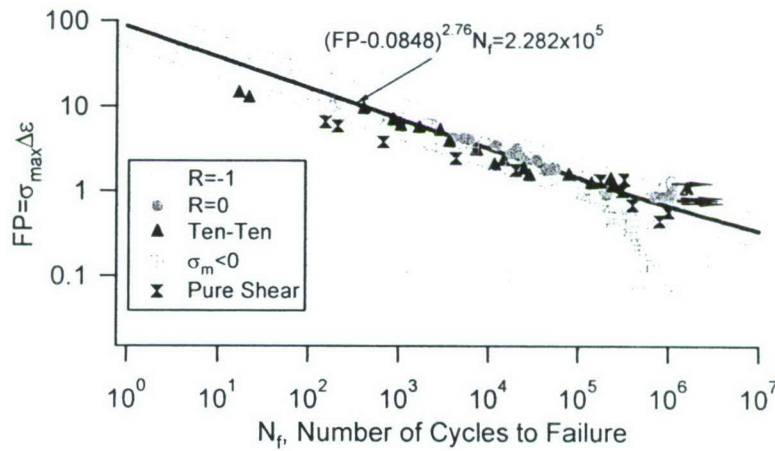
Fig. 5-15 SWT parameter versus fatigue life for uniaxial loading

The general curve in Fig. 5-15 can be best described by the following three-parameter equation,

$$\left(FP_{max} - FP_0\right)^m N_f = C \tag{5-4}$$

where FP_{max} is the SWT parameter as expressed in Eq.(5-3) on the critical plane. For the aluminum alloy under investigation, $m = 2.76$, $C = 2.282x10^5$, and $FP_0 = 0.0848$. These

material constants were obtained by best fitting the general tendency of the experimental data shown in Fig. 5-15.

Once the relationship between the *FP* and the fatigue life is established, fatigue life can be predicted for any given loading condition. Figure 5-16 shows the comparison of the predicted fatigue lives and the observed lives for all the tubular specimens tested in the current investigation. The stress and strain responses were obtained experimentally. Through a coordinates rotation, the *FP* for any given material plane can be determined using the SWT parameter, Eq.(5-3). The maximum *FP* can be determined and the fatigue life can be obtained by using Eq.(5-4). At the same time, the orientation of the critical plane can be determined.
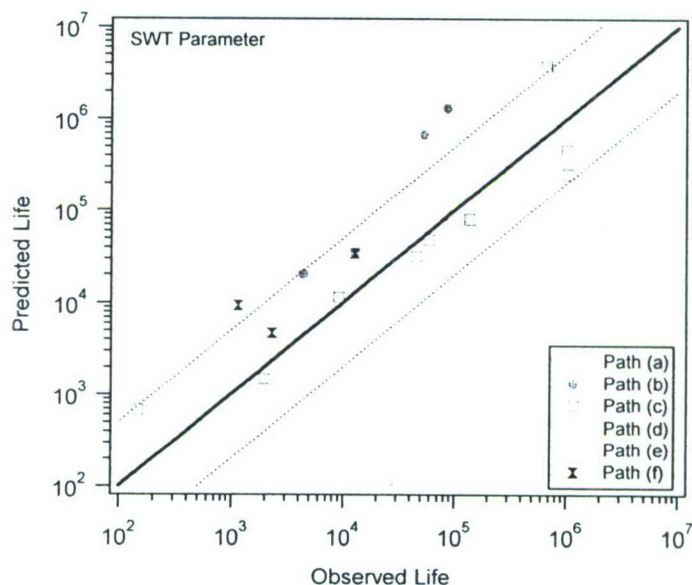
Fig. 5-16 SWT parameter correlation with experiments under combined axial-torsion loading

The solid diagonal line in Fig. 5-16 denotes a perfect prediction. The two dotted lines are the factor-of-five boundary. A glance at Fig. 5-16 reveals that the SWT parameter can correlate the fatigue experiments under combined axial-torsion loading reasonably well. Among a total of 33 tubular specimens, the predicted fatigue lives of eight specimens (24%) are out of the factor-of-five lines.
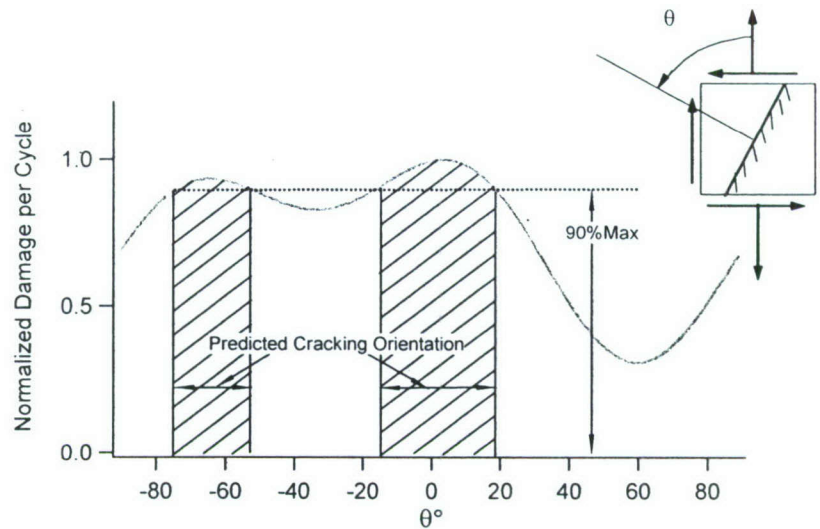
Fig. 5-17 Dependence of fatigue damage on material plane orientation

A critical plane approach can predict both the fatigue life and the critical planes where cracks are predicted to initiate. For an axial-torsion tubular specimen or a uniaxial tension-compression specimen, the material plane can be represented by its normal direction using one angle, θ, measured counter-clockwise from the axial direction (refer to the upper-right insert in Fig. 5-17). For a given loading condition, it is often found that several material planes or a range of material planes may experience identical or very similar fatigue damage according to a given fatigue criterion. Due to the inherent data scatter in fatigue experiments, it would be preferable to identify the material planes with similar fatigue damage by using a given fatigue criterion. In the current investigation, a range of 10% from the maximum fatigue damage is used for the discussion of possible cracking material plane predicted by a fatigue criterion. As shown in Fig. 5-17, the distribution of the fatigue damage per loading cycle over the material plane orientation can be determined according to a criterion for a given loading condition. The fatigue damage per loading cycle is the reciprocal of the predicted fatigue life under constant amplitude loading. The fatigue damage shown in Fig. 5-17 is normalized so that the maximum fatigue damage with respect to all the possible material planes is unit. Theoretically, the maximum peak points are predicted to be the critical planes and cracks are predicted to form on these particular material planes. By considering a range of 10% from the maximum fatigue damage, a range of the cracking directions can be obtained.

Figure 5-18 summarizes the comparison of the observed cracking behavior and the predicted cracking orientations by the fatigue criterion. The solid dark dots represent the observed crack orientations in the figure. The range bars in the figure are the predicted ranges of the cracking directions. Observations on the experimental cracking behavior were made in the millimeter scale of the crack length. Such a treatment is consistent with the macroscopic continuum assumption adopted in the current investigation for the stress and strain.
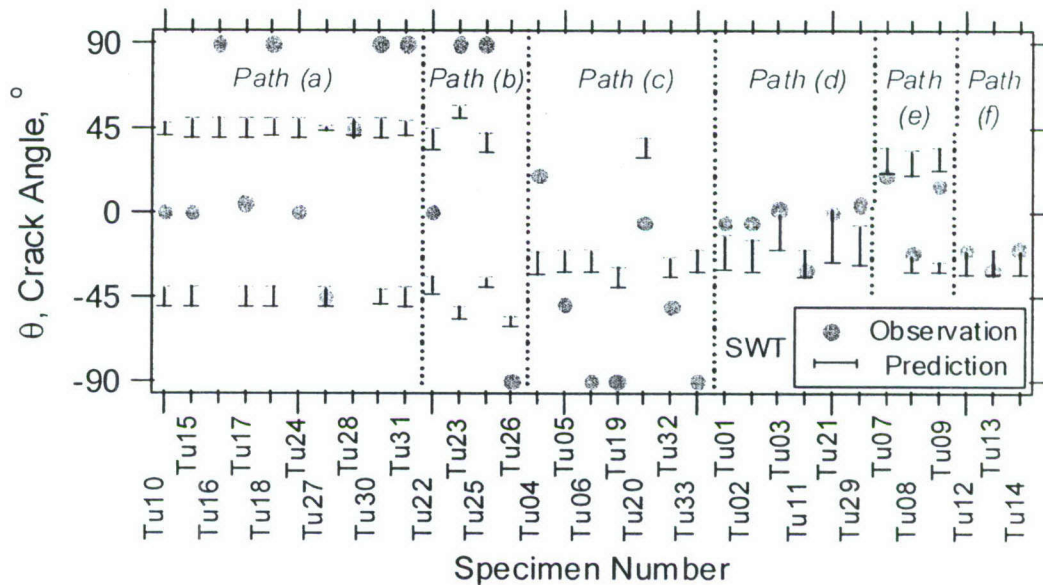
Fig. 5-18 Comparison of the experimentally observed cracking directions with the predictions by the SWT parameter

In theory, a critical plane approach should also predict the cracking behavior of the material subjected to different stress states and loading paths. The SWT parameter predicts tensile cracking behavior. For the material subjected to uniaxial loading, the parameter predicts a cracking plane that is perpendicular to the loading axis in the uniaxial specimen. For a specimen under cyclic torsion, the parameter predicts a crack plane with its normal making 45° angle from the loading specimen axis. Most of the uniaxial specimens under tension-compression were observed to display tensile cracking behavior. For these specimens, the SWT model can predict the cracking behavior well. For the specimens under pure shear, shear cracking was often observed. The SWT model cannot correctly predict the cracking behavior of the material under pure shear loading. The results in Fig. 5-18 show that among the 33 tubular specimens tested

under axial-torsion loading (Fig. 5-18), the SWT model can only predict correctly the cracking behavior of ten specimens (30%).

5.6 Multiaxial Fatigue Criterion

Jiang and Sehitoglu [Jiang and Sehitoglu, 1992] extended the SWT parameter to consider the general stress state and cracking behavior. This fatigue criterion can be modified further to take the following mathematic form,

$$FP = 2b\Delta\varepsilon\sigma_{max} + \frac{1-b}{2}\Delta\tau\Delta\gamma \tag{5-5}$$

where σ and τ are the normal stress and shear stress, respectively, on a material plane. ε and γ are the normal strain and shear strain corresponding to the normal stress, σ, and shear stress, τ, respectively. The symbol Δ denotes range in a loading cycle and the subscript "max" represents maximum in a loading cycle. FP denotes "fatigue parameter". The symbol b in Eq. (5-5) is a material constant and it ranges from 0 to 1.0. The critical plane is defined as the material plane which experiences the maximum fatigue damage. Accordingly, the critical plane is the material plane, which has a maximum FP.

For fully reversed uniaxial loading, the following equation can be derived with coordinates rotation,

$$FP = \frac{1}{4}\left[b\left|1 - \xi + (1 + \xi)\cos 2\theta\right|(1 + \cos 2\theta) + (1 - b)(1 + \xi)\sin^2 2\theta\right]\Delta\sigma_x\Delta\varepsilon_x \tag{5-6}$$

where θ is the angle made by the normal of the material plane and the axial stress direction. $\Delta\sigma_x$ is the axial stress range and $\Delta\varepsilon_x$ is the axial strain range in a loading cycle. The symbol ξ is the contraction ratio of the material under uniaxial loading. This contraction ratio can be obtained using the following equation,

$$\xi = \frac{\Delta\varepsilon_y}{\Delta\varepsilon_x} = 0.5\left(1 - \frac{\Delta\sigma_x}{E\Delta\varepsilon_x}\right) + \mu\frac{\Delta\sigma_x}{E\Delta\varepsilon_x} \tag{5-7}$$

where μ is the Poisson's ratio of the material. In deriving Eq. (5-6), the plasticity incompressibility condition of the material was used.
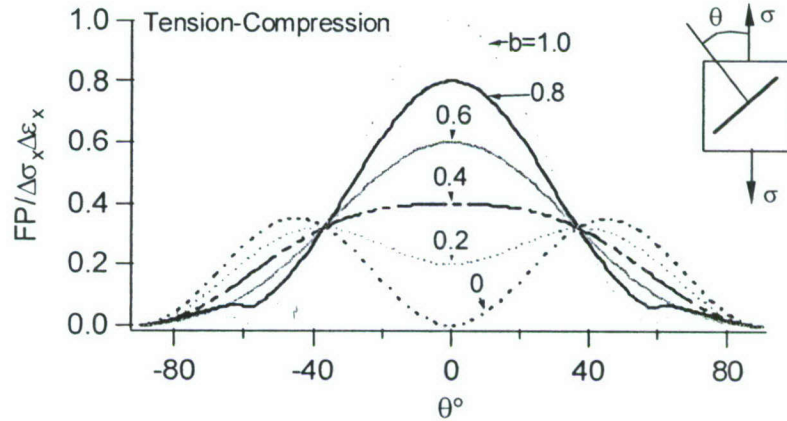

Fig. 5-19 Relationship between FP and the material plane orientation with different b values for fully reversed uniaxial loading
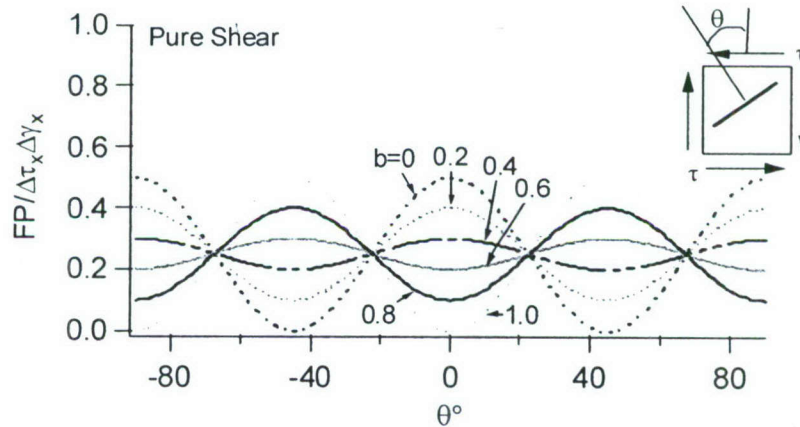

Fig. 5- 20 Relationship between FP and the material plane orientation with different b values for fully reversed shear

For fully reversed pure shear loading, the following relationship is valid,

$$FP = \frac{1}{2}\left[b\sin^2 2\theta + (1-b)\cos^2 2\theta\right]\Delta\tau_{xy}\Delta\gamma_{xy} \tag{5-8}$$

where $\Delta\tau_{xy}$ is the shear stress range and $\Delta\gamma_{xy}$ is the shear strain range in a loading cycle. θ denotes the angle made by the normal of the material plane and the axial direction. The graphic illustrations of Eq. (5-6) and Eq. (5-8) are shown in Fig. 5-19 and Fig. 5-20 for fully reversed uniaxial loading and fully reversed pure shear loading, respectively. Figures 5-19 and 5-20 show the variations of $FP/\Delta\sigma_x\Delta\varepsilon_x$ and $FP/\Delta\tau_{xy}\Delta\gamma_{xy}$ with the orientation of the material plane and the dependence of the critical plane on the material constant b.

With Eq. (5-6) and Eq. (5-8), the critical plane orientation can be determined by taking the derivative of FP with respect to the angle θ and letting the derivative be zero. Clearly, the maximum FP and the critical plane orientation are dependent on the material constant, b. To have a clear picture, Fig. 5-21 shows the dependence of the maximum FP on b for fully reversed tension-compression and pure shear. Figure 5-22 shows the orientation of the critical plane under the two typical loading conditions and the dependence of the critical plane on the material constant b.

Figure 5-21 suggests that the maximum FP under uniaxial loading decreases slightly and then increases with increasing b. For pure shear loading, the maximum FP decreases linearly with increasing b when $b < 0.5$, and increases linearly with increasing b when $b > 0.5$. This ratio of the maximum FP under fully reversed uniaxial loading and that under fully reversed pure shear can help determine the material constant b.
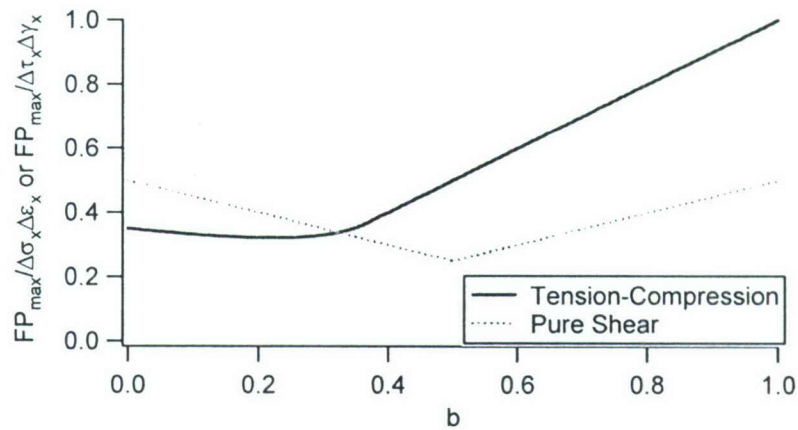
Fig. 5-21 Maximum *FP* as a function of *b* under fully reversed uniaxial and shear loading
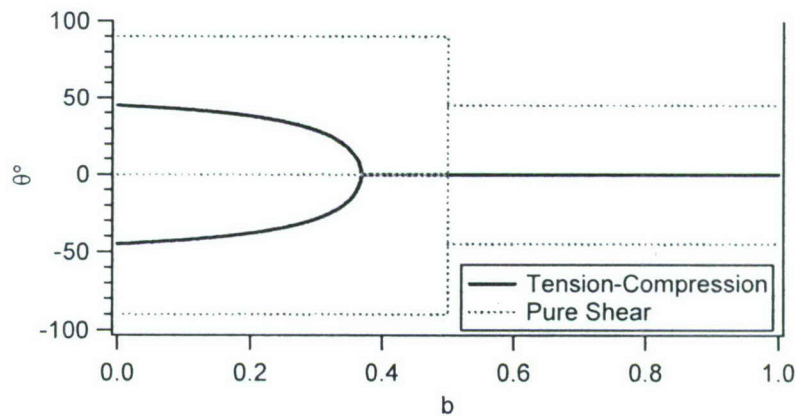

Fig. 5-22 Dependence of critical plane orientation on *b* for fully reversed uniaxial and pure torsion loading

It can be found in Fig. 5-22 that the criterion can deal with materials displaying different cracking behavior. When $b = 0$ the criterion predicts shear cracking behavior. When $b \geq 0.5$, tensile cracking behavior is predicted. Most materials display mixed cracking behavior which can be accounted for with a *b* value between 0.365 and 0.5 according to Fig. 5-22.

5.7   Application of fatigue criterion to 7075T651 aluminum alloy

The material constant b in the fatigue criterion, Eq. (5-5), is determined by comparing the fully uniaxial fatigue and pure torsion fatigue of tubular specimens. Theoretically speaking, the FP_{max} versus the number of loading cycles to failure curves should coincide for the right choice of the material constant b. In addition, the selection of b should reflect the observed cracking behavior from the uniaxial loading and torsion loading.

Clearly, 7075T651 displays cracking behavior that is dependent on the loading magnitude. Since the material constant b in the criterion describe the cracking behavior, an easy relationship between the material constant b and the equivalent stress magnitude can be,

$$b = \langle a_1 - a_2 \sigma_{eq} \rangle \tag{5-9}$$

where a_1 and a_2 are two constants that can be determined by the observed cracking behavior. The symbol $\langle\ \rangle$ in Eq. (5-9) represents the MacCauley bracket (i.e., $\langle x \rangle = 0.5(x + |x|)$). The use of the MacCauley bracket is to ensure a non-negative b value. σ_{eq} is the equivalent stress magnitude following the definition by Jiang and Kurath [Jiang and Kurath, 1997]. The mathematic expression for the equivalent stress magnitude is,

$$\sigma_{eq} = Min\left\{ Max\sqrt{\frac{3}{2}\left(S_{ij} - S_{ij}^0\right)\left(S_{ij} - S_{ij}^0\right)} \right\} \tag{5-10}$$

where S_{ij} denotes the components of the deviatoric stress tensor and S_{ij}^0 represents a point in the deviatoric stress space. The maximum inside the braces is taken with respect to the time within a loading cycle. The minimum is taken in terms of any possible point S_{ij}^0 in the deviatoric stress space. Under tension-compression, the equivalent stress magnitude is equal to the stress

amplitude. For pure shear loading, the equivalent stress magnitude is equal to the shear stress amplitude multiplied by $\sqrt{3}$.

For 7075T651 aluminum alloy, $a_1 = 0.8625$ and $a_2 = 1.25$. Two points can be approximately identified from the cracking behavior of the material under fully reversed tension-compression and pure torsion. When the fatigue life is 3×10^5 cycle under fully reversed loading, the material transits from shear cracking to mixed cracking (Fig. 5-11). The corresponding equivalent stress is 398 MPa. From the pure torsion experiments, it can be identify that the material switch from mixed cracking to tensile cracking when the fatigue life is in the region of 4000 cycles (Fig. 5-11). Since the corresponding equivalent stress magnitude is 290 MPa, it can be identified that $b = 0.5$ when $\sigma_{eq} = 290 MPa$.

Figure 5-23 shows the FP_{max} versus N_f relationship for the uniaxial loading and torsion of cylindrical specimens. The three-parameter equation, Eq.(5-4), can be used again to describe the relationship between P_{max} and N_f. For 7075T6 when the new fatigue model (Eq.(5-4)) is used, $m = 3$, $FP_0 = 0.2$, and $C = 2 \times 10^5$ from best fitting the data in Fig. 5-23 for the experiments under fully reversed uniaxial loading.
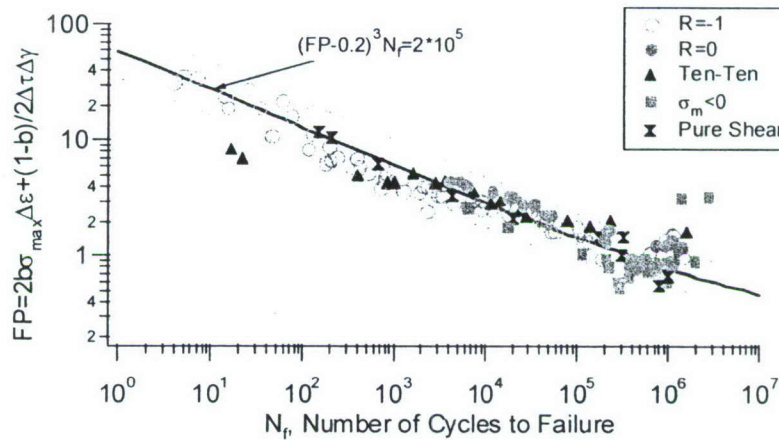

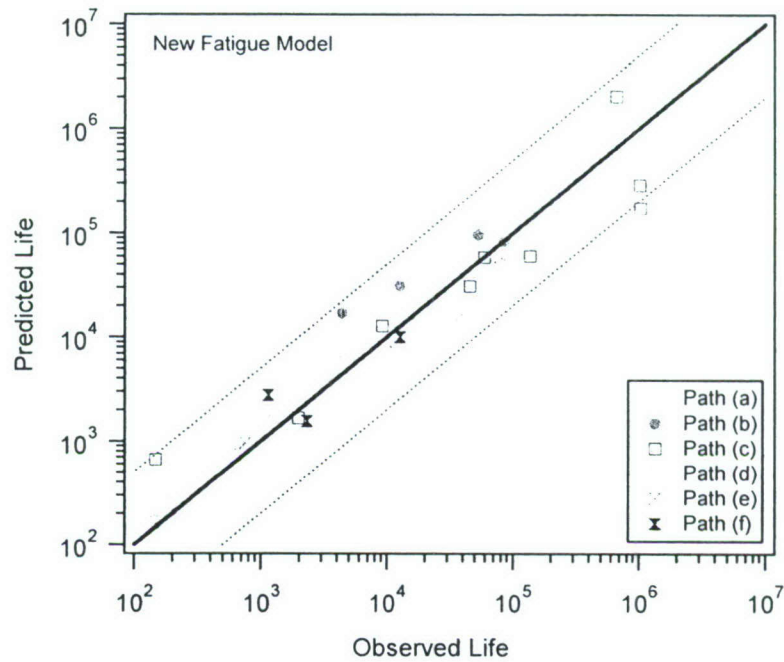**Fig. 5-23** FP_{max} versus N_f for fully reversed uniaxial and torsion loading

Fig. 5-24 Experimental observations and predicted life obtained by using the criterion Eq.(5-5)

Once the material constant b is selected, the critical plane and FP_{max} for each specimen conducted can be determined. Figure 5-24 shows the comparison of the predicted fatigue lives and the experimentally observed fatigue lives of the tubular specimens subjected to combined axial-torsion loading. The solid line in Fig. 5-24 signifies a perfect prediction and the two dotted lines are the factor-of-five boundary. Among the 33 tubular specimens tested with different axial-torsion loading paths, only one data point is slightly out of the factor-of-five lines.
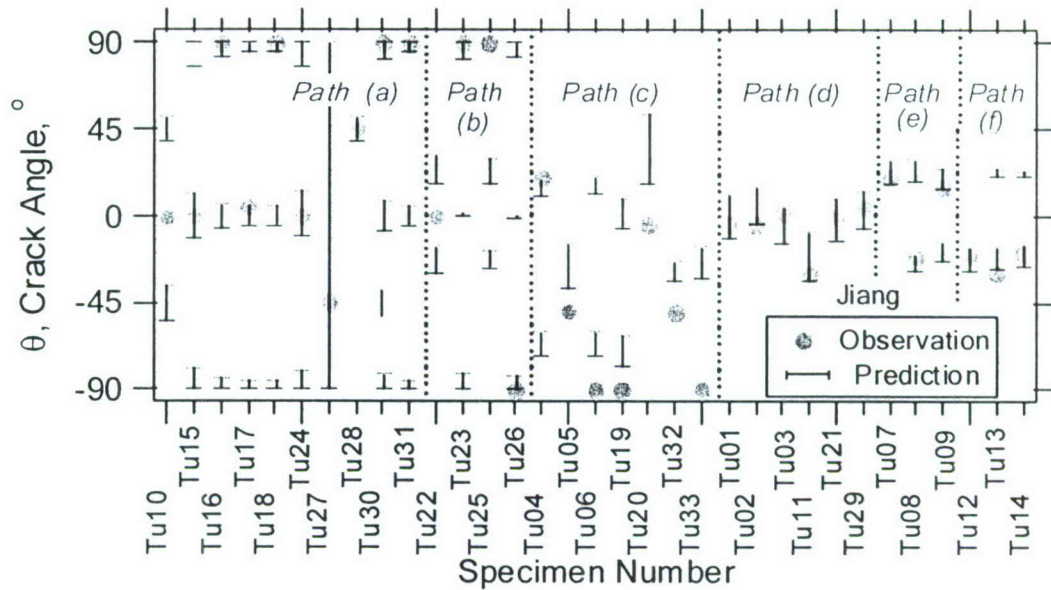
Fig. 5-25 Comparison of the experimentally observed cracking directions with the predictions made by using the criterion Eq.(5-5)

Figure 5-25 summarizes the comparison of the observed cracking behavior and the predicted cracking orientations by the fatigue criterion. The solid dark dots represent the observed crack orientations in the figure. The range bars in the figure are the predicted ranges of the cracking directions. Observations on the experimental cracking behavior were made in the millimeter scale of the crack length. Such a treatment is consistent with the macroscopic continuum assumption adopted in the current investigation for the stress and strain.

The results shown in Fig. 5-25 reveal that the predictions for the cracking directions are satisfactory. Most of the cracking directions are predicted correctly. It should be noted that a number of material planes may experience similar fatigue damage under a given loading condition.

The evaluations of the two fatigue models based upon the extensive fatigue experiments reveal that the SWT fatigue model can work reasonably well for the material in terms of fatigue life predictions. However, the SWT model cannot properly predict the fatigue cracking behavior. The new fatigue model can properly predict both the fatigue life and the cracking behavior.

Therefore, the new fatigue model will be further evaluated and confirmed with the specimens mimicking the real structures.

5.8   Application to Notched Members and Box Lattice Structure

One major difference between a real structure and the tubular specimen is that the specimen surface is smooth while a real structure can contain a notch. Notches refer to the geometric discontinuities that exist in structural members. A notch introduces stress concentration. In order to validate the fatigue model developed in the current research, notched shafts were subjected to combined axial-torsion loading. In addition, box lattice structures were experimentally studied for the fatigue behavior subjected to repeated bending loading. The experimental results obtained from testing the notched members and the box lattice structures are used to further evaluate the model developed.

Notched Specimen and Box Lattice Structure: The notched specimen under investigation was cylindrical and it was subjected to combined axial-torsion fatigue loading (Fig. 5-26). Three different notch sizes were used to generate different degrees of stress concentration. The experiments were conducted using the tension-torsion fatigue machine. The axial load, P, and the torque, T, were controlled in the experiment. Two loading paths were used: one was fully reversed shear combined with a static axial load and the other was 90-degree-out-of-phase combined axial-torsion loading (Fig. 5-27). Together with different notch sizes, the experiments created the conditions that can be used to critically evaluate a fatigue model.

The fatigue results obtained from testing the notched shafts are listed in Table 5-7 and shown in Fig. 5-28. In Fig. 5-28, only the torque amplitude was used to represent the loading magnitude. The axial load can be determined for a given torque value.

Table 5-7 Fatigue results of notched shafts

Loading Path	Spec#	Notch Size mm	$\frac{\Delta P}{2}$ or P kN	$\frac{\Delta T}{2}$ Nm	N_f cycles
I	TORN09	6.35	70.5	126.8	27,208
	TORN08	6.35	35.2	126.6	104,357
	TORN19	3.18	56.7	113.6	24,785
	TORN18	3.18	28.4	114.1	163,689
	TORN29	1.11	38.5	92.0	30,371
	TORN28	1.11	19.3	92.0	203,127
II	TORN04	6.35	70.7	254.4	769
	TORN07_2	6.35	61.8	222.6	1,032
	TORN02	6.35	52.9	190.5	2,986
	TORN03	6.35	44.3	159.5	5,816
	TORN06	6.35	38.8	139.7	35,950
	TORN01	6.35	35.1	126.0	94,750
	TORN07_1	6.35	28.3	101.8	1,462,100
	TORN12	3.18	70.2	279.9	501
	TORN13	3.18	56.5	226.1	1,285
	TORN17_2	3.18	49.8	199.7	2,012
	TORN11	3.18	42.5	170.4	5,896
	TORN14	3.18	35.3	141.1	15,940
	TORN16	3.18	31.1	124.4	47,815
	TORN15	3.18	28.3	113.2	175,713
	TORN17_1	3.18	25.6	102.7	1,014,530
	TORN23	1.11	57.8	275.9	290
	TORN21	1.11	48.1	229.9	708
	TORN22	1.11	38.5	183.9	1,990
	TORN25	1.11	28.9	138.0	7,636
	TORN24	1.11	24.1	115.3	17,819
	TORN26	1.11	21.3	101.8	36,807
	TORN27	1.11	19.3	92.5	362,070

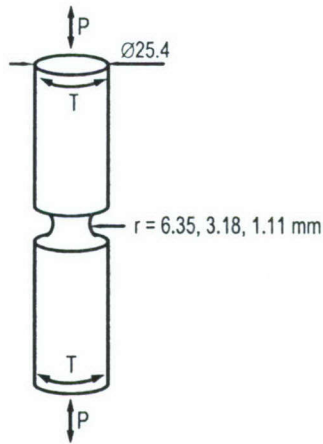$\Delta P/2$ =load amplitude, = static axial load, $\Delta T/2$ = torque amplitude, N_f =fatigue life

Fig. 5-26 Notched shaft specimen
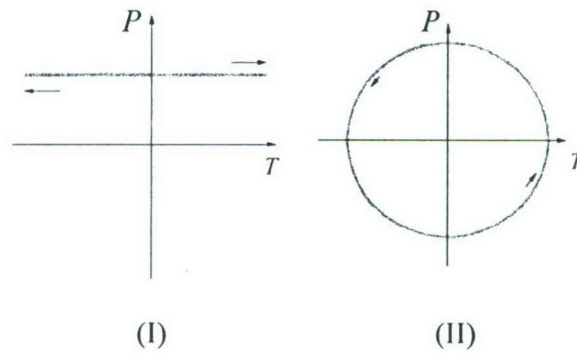

(I)   (II)

Fig. 5-27 Axial-torsion loading paths used for notched shaft specimen
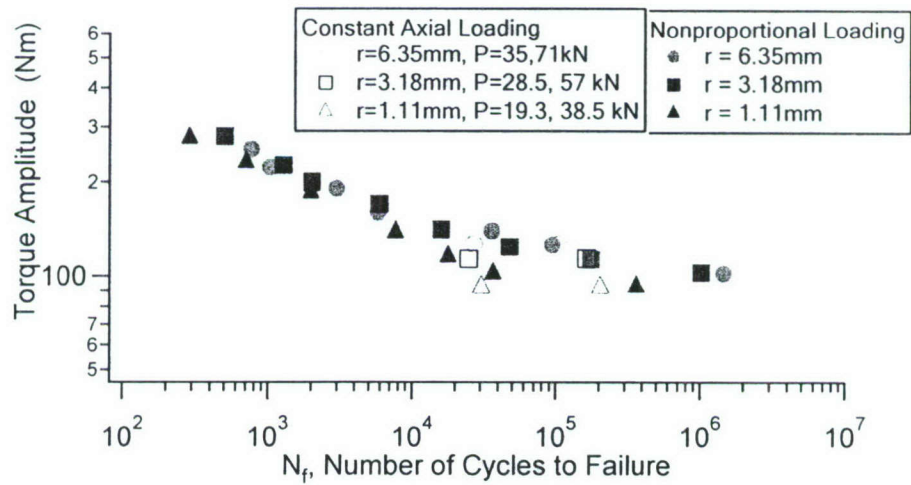

Fig. 5-28 Fatigue results obtained from testing the notched specimens

The box lattice specimen was fabricated using the Electro-Discharge Machining (EDM). EDM is one of the most accurate manufacturing processes for creating complex shapes or geometries in parts. EDM works by eroding material in the path of electronic discharges that forms an arc between a mating electrode and a work piece. A mating electrode was manufactured by a vendor. A typical electrode shown in Fig. 5-29 is made of copper. To create a potential difference between the electrode and the work piece, the work piece is immersed in the dielectric fluid which is circulated to flush away debris. To make the box lattice shape, one side of the work piece is shaped first. Then the work piece is flipped over to make the lattice shape of the other side of the work piece.
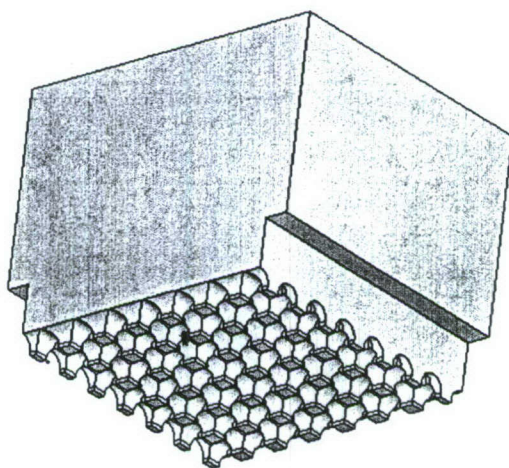

**Fig. 5-29** Typical electrode used in EDM to fabricate the box lattice structure

Aluminum box lattice specimens (Fig.5-30(a)) with circular cross sections were fabricated for mechanical three-point bending testing. The filament cross section has a diameter of 2mm (Fig. 5-30) and a pitch of 3.1 mm in all the three directions. Two pure copper box lattice samples were manufactured for heat transfer experiments. One sample had a circular cross section. The diameter was 1.0 mm and the pitch was 1.55 in all the three directions. The other pure copper box lattice sample had an elliptical cross section. The pitch was 1.5 mm in all the three directions. The major diameter of the filament was 1.0 mm and the minor diameter was 0.5 mm.

The three-point bending fatigue was carried out using a fixture specially designed for the experiment (Fig. 5-31). The span between the two lower supports was 46.5 mm and the load was applied at the middle point of the specimen. The testing frequency ranged from 0.5 Hz to 2 Hz

dependent on the loading magnitude. A higher testing frequency was used for longer fatigue life. The fatigue results of the lattice box structure are summarized in Table 5-8 and shown in Fig. 5-32. All the failures were found at the middle section of the specimen where the load was applied (Fig. 5-33).
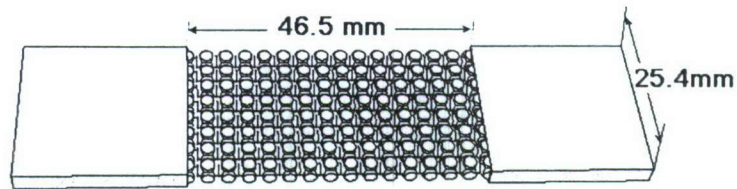
(a) Aluminum circular cross section filament specimen for mechanical testing
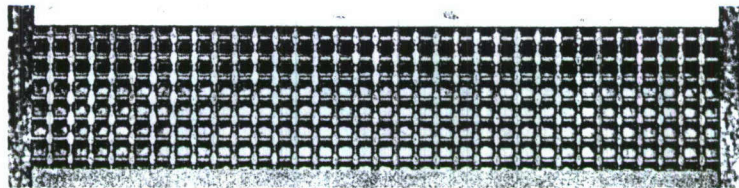
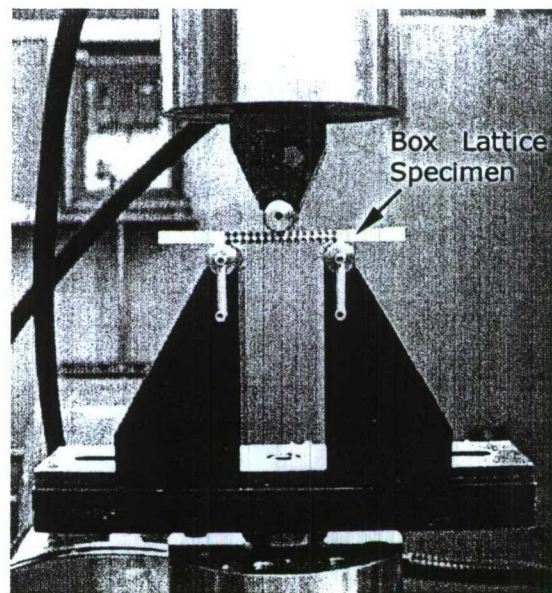(b)Pure copper ellipse cross section filament specimen for heat transfer experiment

Fig. 5- 30 Box lattice specimens

Fig. 5-31 Experimental set-up for three-point bending fatigue

Table 5-8 Fatigue results of lattice box specimens subjected to three bending

Spec No.	P_{max} (N)	P_{min} (N)	$\frac{\Delta P}{2}$ (N)	N_f cycles
AORS04	500	52	224	1,152
AORS01	400	43	178	3,152
AORS03	294	29	133	7,385
AORS05	269	28	120	11,704
AORS07	243	25	109	13,817
AORS02	224	26	99	121,732

P_{max} =maximum load, P_{min} = minimum load, $\Delta P/2$ =load amplitude and N_f =fatigue life
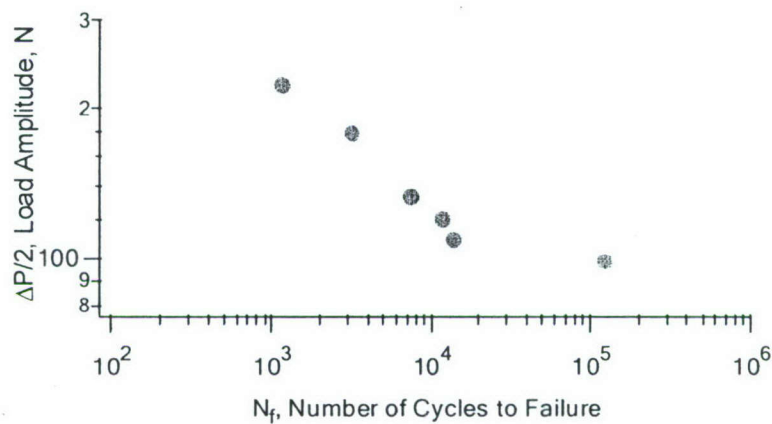

Fig. 5-32 Loading amplitude versus fatigue life for the box lattice specimens
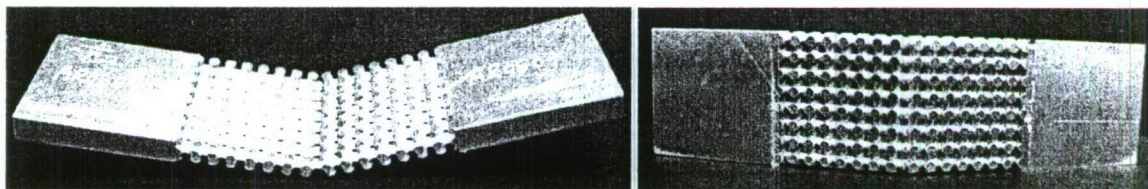

Fig. 5-33 Failure mode of the aluminum box lattice specimen under repeated bending

5.9. Fatigue Life Predictions

Prediction of the fatigue life of a real structure takes two steps. The first step is the stress analysis so that the detailed stress-strain response of every material point in the structure is obtained. The second step is to use a fatigue criterion to assess the fatigue life based on the detailed stress-strain response obtained from the first step. Finite element method is used for the stress analysis and the fatigue criterion discussed in a previous section is used to make the fatigue prediction.

Finite element simulations: The mesh model used in the finite element analysis is shown in Fig. 5-34. The mesh model was built in ABAQUS CAE. Element C3D4, a three-dimensional four-node element, was used to construct the model. Due to the duplication of the lattice structure, only one rib was modeled. And due to the symmetry in the three-point bending, only half of the rib was modeled. The model has a average element size of 0.16mm, contains 25,954 nodes and 127,831 elements. One end was fixed and one half of load applied to the rib was applied at the other end of the model.
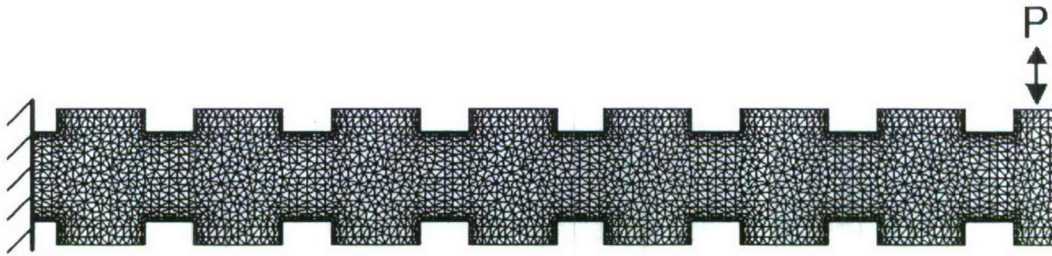

Fig. 5-34 Finite element mesh model for the box lattice

Finite element stress analysis was conducted using the package ABAQUS [ABAQUS, 2006]. For the elastic-plastic stress analysis, the plasticity theory of Jiang and Sehitoglu [Jiang and Sehitoglu, 1996] was implemented into ABAQUS as a user-defined subroutine (UMAT). The constitutive equations for modeling cyclic plasticity deformation are summarized in Table 5-9. The material constants used in the plasticity model are listed in Table 5-10. They were obtained from the stress-strain curve of the fully reserved uniaxial tension-compression experiments shown in Fig. 5-6.

Table 5-9 Cyclic plasticity model used in the finite element simulations

Yield Function	$f = (\widetilde{S} - \widetilde{\alpha}):(\widetilde{S} - \widetilde{\alpha}) - 2k^2 = 0$	$\widetilde{S}$ = deviatoric stress $\widetilde{\alpha}$ = backstress k = yield stress in shear
Flow Law	$d\widetilde{\varepsilon}^{\,p} = \dfrac{1}{h}\left\langle d\widetilde{S} : \widetilde{n} \right\rangle \widetilde{n}$	$\widetilde{n}$ = normal of yield surface h = plastic modulus $\widetilde{\varepsilon}^{\,p}$ = plastic strain
Hardening Rule	$\widetilde{\alpha} = \displaystyle\sum_{i=1}^{M} \widetilde{\alpha}^{(i)}$ $d\widetilde{\alpha}^{(i)} = c^{(i)} r^{(i)} \left(\widetilde{n} - \left(\dfrac{\left\| \widetilde{\alpha}^{(i)} \right\|}{r^{(i)}} \right)^{\chi^{(i)}+1} \dfrac{\widetilde{\alpha}^{(i)}}{\left\| \widetilde{\alpha}^{(i)} \right\|} \right) dp \;\;, (i = 1,2,\cdots,M)$	$\widetilde{\alpha}^{(i)}$ = ith backstress part M = number of backstress parts dp = equivalent plastic strain increment $c^{(i)}$, $r^{(i)}$, $\chi^{(i)}$ = material constants

Table 5-10 Material constants used in the cyclic plasticity model

E=71.7GPa, μ=0.306, k=227 MPa,

$c^{(1)}$=153, $c^{(2)}$=34.8, $c^{(3)}$=12.8, $c^{(4)}$=6.0, $c^{(5)}$=3.27,

$r^{(1)}$=25 MPa, $r^{(2)}$=34 MPa, $r^{(3)}$=42 MPa, $r^{(4)}$=52 MPa, $r^{(5)}$=280 MPa,
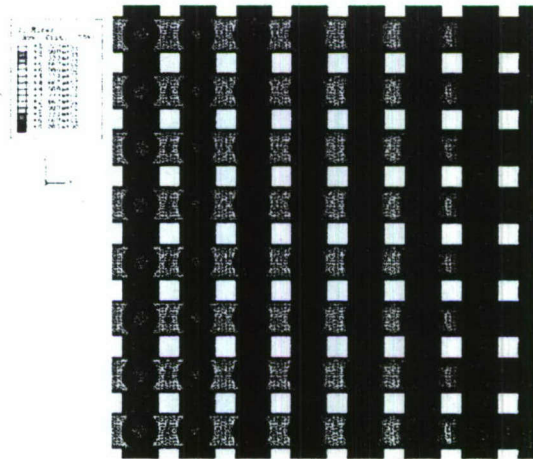

Fig. 5-35 Contour of equivalent von Mises stress when the Load was 400 N.

The finite element stress analysis mimicked the actual loading conditions employed in the experiments. Figure 35 shows the contour of the equivalent von Mises stress when the applied load was 400 N. The notch root area near closest to the point of load application experienced maximum stress.

Once all the detained stress-strain response was obtained for any material point in the structure, the fatigue model developed in the current research (Eq.(5-5)) can be used to access the fatigue damage. The critical plane and the maximum *FP* can be identified by rotating the coordinates system in the implementation of the fatigue model for each material point. Plots in Fig. 5-36 show the contour of the fatigue parameter (FP) with different views for the loading condition with a maximum external load of 400 N and minimum load of 40 N. By comparing the fatigue damage of all the material points in the structure, the critical position where fatigue will occur can be identified. In this way, the fatigue life of the structure can be predicted.
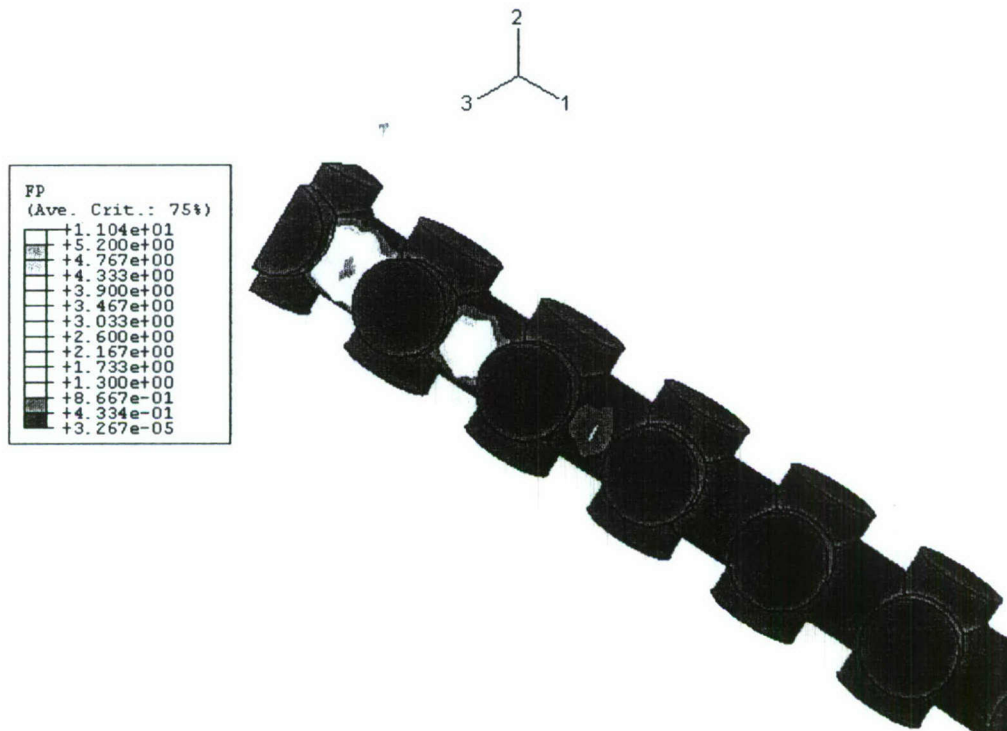

Fig. 5-36 Contour of fatigue parameter (3D view) (Specimen: AROS01: P_{max}=0.4KN, P_{min}=0.04KN)

The post-processing was carried out with a custom-designed post-processor. This post-processor implemented the fatigue model developed in the current research. It can provide the contour of the fatigue parameter (such as that shown in Fig. 5-36), identify the critical location where fatigue failure is predicted to occur, and the fatigue life of the component.
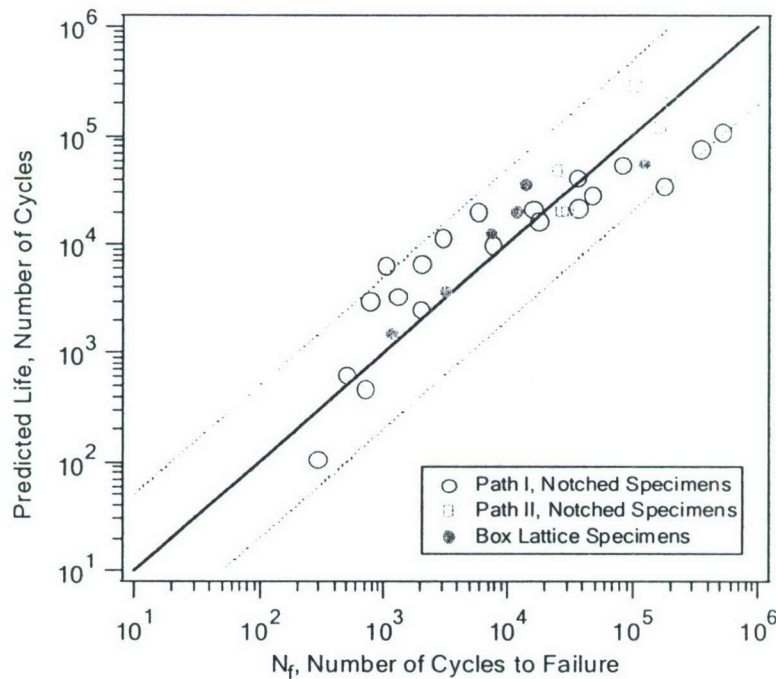

Fig. 5-37 Comparison of the observed fatigue life with the predictions for the notched and box lattice specimens

The results shown in Fig. 5-37 suggest that the models developed in the current research can correlate very well the experiments of the structures subjected to fatigue loading.

5.10   Conclusions

The two major structural concerns are the strength and deformation when a structure is subjected to external loading. The deformation of a structure can be reliably simulated using the finite element method by implementing a suitable constitutive material deformation law. The strength of a structure needs to consider static loading and dynamic loading. For the static strength, the well-established von Mises criterion can be used after a stress analysis of the structure. The major concern of a structure is the fatigue strength. The current research has established an

approach that can be used for the fatigue design and evaluation of an aluminum structure subjected to dynamic or fatigue loading.

The approach for the fatigue strength consideration consists two steps. The first step is to determine the detailed stress-strain response of the material in the structure using the finite element method. A key element in the finite element stress analysis is the use of a suitable constitutive material law. The cyclic plasticity theory developed by Jiang and Sehitoglu [1996] has been widely accepted for the modeling of the stress-strain relationship of metallic materials. The current research confirms that the cyclic plasticity theory is well suited for the aluminum alloy that can be used as a heat exchanger. The cyclic plasticity model has been implemented into the finite element code.

Once the stress-strain response of the materials in a structure is obtained, a fatigue model is used to assess the fatigue strength of the material. The current research has generated extensive deformation and fatigue results for 7075T6 aluminum alloy. The experimental results provide all the baseline mechanical properties of the material that are needed for the consideration of the mechanical properties of the aluminum structures. A robust fatigue model was developed and the model was validated with extensive experiments. A post-processor that implemented the fatigue model has been developed. The post-processor together with the finite element stress analysis can be directly applied to the fatigue design and evaluation of the multifunctional structures.

6   References

ABAQUS User's Manual, V 6.5, Hibbitt, Karlsson & Sorensen, Inc., 1080 Main Street, Pawtucket, Rhode Island 02860-4847, Tel: 1 401 727 4200, Facsimile: 1 401 727 4208

Bird, R. B., Stewart, W. E., and Lightfoot, E. N., "Transport Phenomena", John Wiley & Sons, Inc., 1966.

Balantrapu, K. (2006) "Thermal/Fluid Characteristics of Cylindrical-Filament Open-Cell Box-Lattice Structures as Heat Exchanger Surfaces", MS Thesis, Mechanical Engineering Dept., Univ. Nevada, Reno, 89557

Balantrapu, K., D. Sarde, C. M. Herald and R.A. Wirtz (2005) "Porosity, Specific Surface Area and Effective Thermal Conductivity of Anisotropic Open Cell Lattice Structures", IPACK2005-73191, Proc. InterPack 2005, July 17 – 22.

Brautsch, A., and Kew, P., 2002, "The Effect of Surface Conditions on Boiling Heat Transfer From Mesh Wicks," Proceeding of the 12th International Heat Transfer Conference.

Cavaliere, P. and Squillace, A. (2005) "High temperature deformation of friction stir processed 7075 aluminium alloy", Materials Characterization, Volume 55, Issue 2, Pages 136-142

Chang, W.S., (1990) "Porosity and Effective Thermal Conductivity of Wire Screens", JHT, Vol. 112, pp. 5 – 9.

Chang, J. Y., and You S. M., 1997, "Boiling Heat Transfer Phenomena from Microporous and Porous Surfaces in Saturated FC-72," International Journal of Heat and Mass Transfer, **40**, pp. 4437-4447.

Dhir, V.K. (1994) "Boiling and Two-Phase Flow in Porous Media", Annual Review of Heat Transfer, CRC Press, Boca Raton, pp. 303 - 350

Dybbs, A. and Edwards, R. V., "Fundamentals of Transport Phenomena in Porous Media", Martinus Nijoff Publishers, 1984, pp. 201-256.

Gerlach, D. W., and Joshi, Y. K., 2005, "Boiling Performance of Fluorinert 5060 on Confined and Unconfined Wire Meshes Soldered to the Substrate," Proceedings of the ASME International Mechanical Engineering Congress and Exposition, November 5-11, Orlando, FL, USA.

Germano, M., Piomelli, U., Moin, P., and Cabot, W., "A Dynamic Subgrid-Scale Eddy Viscosity Model", *Physics of Fluids*, Vol. 3, No. 7, 1991, pp. 1760-1765.

Gullbrand, J., K. Balantrapu and R.A. Wirtz (2005) "Thermal Characterization of Open Lattice Structures used as Heat Exchanger Surfaces", AIAA Paper 2005-0185, 43-rd AIAA Aerospace Sciences Meeting, Reno , NV January 10, 2005

Holland, B. (2006) "Flow Boiling of FC-72 from a Screen Laminate Extended Surface Matrix" MS Thesis, Mechanical Engineering Dept., University of Nevada, Reno, 89557

Incropera, F. P, and DeWitt, D. P., 2002, "Introduction to Heat Transfer," 4th ed., John Wiley and Sons.

Jiang, Y., (2000) "A Fatigue Criterion for General Multiaxial Loading," *Fatigue and Fracture of Engineering Materials and Structures*, Vol.23, pp.19-32.

Jiang, Y. and Kurath, P., 1997, "NonProportional Cyclic Deformation: Critical Experiments and Analytical Modeling," *International Journal of Plasticity*, Vol.13, pp.743-763

Jiang, Y. and Sehitoglu, H., (1992) Report no. 161, UILU-ENG 92-3602, College of Engineering, University of Illinois at Urbana-Champaign

Jiang, Y. and H. Sehitoglu (1996) "Modeling of Cyclic Ratchetting Plasticity" ASME *Journal of Applied Mechanics*, Vol.63, pp.720-733

Lee, S., Song, S., Au, V., and Moran, K., 1995, "Constriction/Spreading Resistance Model for Electronics Packaging," ASME/JSME Thermal Engineering Conference, Vol.4, pp. 199-206

Li, C. and Peterson, G. (2005) "Experimental study of thickness effects on evaporation/boiling on thin sintered copper mesh surfaces", Proc. ASME Summer Heat Transfer Conf. paper HT2005-72431.

McGillis, W., Carey, V., Fitch, J. and Hamburgen, W. (1991) "Pool boiling enhancement techniques for water a low pressure", Proc. Seventh SEMI-Therm Symposium, pp. 64 – 72.

Mickley, H. S., Smith, K. A., and Korchak, E. I., "Fluid Flow in Packed Beds", Chemical Engineering Science", Vol. 20, 1965, pp. 237-246.

Mukherjee, S., and Mudawar, I., 2003, "Smart Pumpless Loop for Micro-Channel Electronic Cooling Using Flat and Enhanced Surfaces," IEEE Transactions on Components and Packaging Technologies, **26**, pp. 99-109

Lilly, D., "A Proposed Modification to the Germano Subgrid-Scale Closure Method", *Physics of Fluids*, Vol. 4, No. 3, 1992, pp. 633-635.

Nadai, A., 1950. "Theory of low and fracture of solids", vol. 1, 2nd Ed. McGraw-Hill Book Company, Inc., New York, Toronto, and London.

Nakayama, W, Nakajima, T and Hirasawa, S. (1989) "Heat sink studs having enhanced boiling surfaces for cooling of microelectronic components", ASME paper 84-WA/HT-89

Park, J.-W., Ruch, D., and Wirtz, R. A., (2002) "Thermal/Fluid Characteristics of Isotropic Plain-Weave Screen Laminates as Heat Exchange Surfaces", *AIAA* paper 2002-0208.

Rainey, K. N., and You, S. M., 2000, "Pool Boiling Heat Transfer From Plain and Microporous, Square Pin-Finned Surfaces in Saturated FC-72," Journal of Heat Transfer, **122**, pp. 509-516.

Sarde, D. (2006) "Thermal/Fluid Characteristics of Elliptic Cross-Section Filament Box-Lattices as Heat Exchanger Surfaces", MS Thesis, Mechanical Engineering Dept., University of Nevada, Reno, 89557

Sarde, Deepti, C. Herald and R.A. Wirtz (2006) "Thermal/Fluid Characteristics of Elliptic Cross Section Filament Box Lattice Matrices as Heat Exchanger Surfaces" AIAA Thermophysics and Heat Transfer Conference, San Francisco, CA, June 6 – 8, 2006

Smagorinsky, J., "General Circulation Experiments with the Primitive Equations", Monthly Weather Review, Vol. 91, 1963, pp. 99-152.

Smith, R.N. Watson, P. and Topper, T.H. "A stress-strain parameter for the fatigue of metals" Journal of Materials, 1970, Vol.5, No.4, pp.767-778

Socie, D.F. (1987) "Multiaxial fatigue damage models", ASME *Journal of Engineering Materials and Technology*, Vol. 109, pp.293-298

Suekane, T., Yokouchi, Y., and Hirai, S., "Inertial Flow Structures in a Simple-Packed Bed of Spheres", *Fluid Mechanics and Transport Phenomena*, Vol. 49, No. 1, 2004, pp., 10-17.

Tong, L.S. and London, A.L. (1957) "Heat Transfer and Flow-Friction Characteristics of Woven-Screen and Crossed-Rod Matrices" Trans. ASME, pp. 1558 – 1570

Vasil'Yev, A. (1992) "Heat Transfer and Critical Heat Flux Density in Boiling of Water Under a Vacuum on Walls Covered with a Single Layer of Mesh", Heat Transfer Research, Vol. 24, pp. 913 – 921.

Wakao, N., and Kaguei, S., "Heat and Mass Transfer in Packed Beds", Gordon and Breach, 1982.

Wirtz, R., Fuchs, A., and Jiang, Y. (2003) "Multi-Functional Materials for Thermal Control of Sensors and Electronics," Final Report Submitted to The Missile Defense Agency through the Air Force Office of Scientific Research (F49620-00-1-305)

Wirtz, R. A., Xu, S., Park, J.-W., and Ruch. D. (2003) "Thermal/Fluid Characteristics of 3-D Woven Mesh Structures as Heat Exchanger Surfaces", *IEEE Trans Components and Packaging Technology*, Vol. 26, , pp. 40-47.

Xu, J. and Wirtz, R.A. (2003a) "In-plane Effective Thermal Conductivity of Plane-Weave Screen Laminates", IEEE Trans. on Components and Packaging Tech, Vol. 25, #4, pp. 615 - 620,.

Xu, J., and Wirtz, R. A. (2003b) "In-Plane Effective Thermal Conductivity of Plain Weave Screen Laminates with Arbitrary Weave Parameters", Paper TED-AJ03-417, 6-th ASME-JSME Thermal Engineering Joint Conference, Hawaii, March 16 - 20.

Yevseyev, A. R., Nakorayakov, V. E., and Romanov N. N., "Experimental Investigation of a Turbulent Filtrational Flow", *International Journal of Multiphase Flow*, Vol. 17, No. 1, 1991, pp. 103-118.

7. Ancillary Information

Research Personnel

The research team includes: R.A. Wirtz (PD; Heat Transfer in Electronics); Yanyao Jiang (Co-PI; structural analysis); Two Post-Doctoral Associates: Jessica Gullbrand (CFD and Heat Transfer) and Miaolin Feng (Structural Analysis). Four graduate trainees (Kiran Balantrapu, Ben Holland, MS; Deepti Sarde, MS and Tianwen Zhao, PhD) have participated.

Publications/ Theses

Publications

Balantrapu, K., D. Sarde, C. M. Herald and R.A. Wirtz (2005) "Porosity, Specific Surface Area and Effective Thermal Conductivity of Anisotropic Open Cell Lattice Structures", IPACK2005-73191, Proc. InterPack 2005, July 17 – 22.

Gullbrand, J., K. Balantrapu and R.A. Wirtz (2005) "Thermal Characterization of Open Lattice Structures used as Heat Exchanger Surfaces", AIAA Paper 2005-0185, 43-rd AIAA Aerospace Sciences Meeting, Reno, NV January 10, 2005

Gullbrand, J., R.A. Wirtz (2005) "Comparison of LES and RANS Simulations of Turbulent Convection in a Structured Porous Media", Paper HT2005-721148, ASME Summer Heat Transfer Conference, San Francisico, CA.

Jiang, Y. and Zhao, T. (2006) "Multiaxial Fatigue of 7075 Aluminum Alloy," International Conference on Fatigue Damage of Structural Materials, Hyannis, Sept., 2006

Jiang, Y. and Zhao, T. (2005) "A Pseudo-Plasticity Concept for Fatigue Damage Assessment," Dislocations, Plasticity, Damage and Metal Forming: Material Response and Multiscale Modeling---Proceedings of PLASTICITY'05, A.S. Khan and A.R. Khoei, Eds., Neat Press, pp.202-204.

Sarde, Deepti, C. Herald and R.A. Wirtz (2006) "Thermal/Fluid Characteristics of Elliptic Cross Section Filament Box Lattice Matrices as Heat Exchanger Surfaces" AIAA Thermophysics and Heat Transfer Conference, San Francisco, CA, June 6 – 8, 2006

Zhao, T. and Jiang, Y. (2006) "Fatigue of 7075T6 Aluminum Alloy," Fatigue'2006, *FT266*, Atlanta, May, 2006

Thesis

Balantrapu, K. (2006) "Thermal/Fluid Characteristics of Cylindrical-Filament Open-Cell Box-Lattice Structures as Heat Exchanger Surfaces", MS Thesis, Mechanical Engineering Dept., Univ. Nevada, Reno, 89557

Holland, B. (2006) "Flow Boiling of FC-72 from a Screen Laminate Extended Surface Matrix" MS Thesis, Mechanical Engineering Dept., University of Nevada, Reno, 89557

Sarde, D. (2006) "Thermal/Fluid Characteristics of Elliptic Cross-Section Filament Box-Lattices as Heat Exchanger Surfaces", MS Thesis, Mechanical Engineering Dept., University of Nevada, Reno, 89557

Papers Pending

Holland, B. and Wirtz, R.A. (2007) "Flow Boiling of FC-72 from a Screen Laminate Extended Surface Matrix", THERMES 2007, Santa Fee, NM.

Zhao, T. and Jiang, Y. (2006) "A Study of Crack Initiation of 7075T6 Aluminum Alloy," Submitted to International Journal of Fatigue

Zhao, T. and Jiang, Y. (2006) "Modeling of Crack Growth on 7075T6 Aluminum Alloy," To Be Submitted to Engineering Fracture Mechanics

Zhao, T. and Jiang, Y. (2006) "A Study of Crack Growth from a Notch," To Be Submitted to International Journal of Fatigue

8   Acknowledgement/Dissclaimer